Atomic Layer Deposition of Cobalt Oxide and Copper Oxide Thin Films

Tomi Iivonen

Department of Chemistry
Faculty of Science
University of Helsinki
Helsinki, Finland

DOCTORAL DISSERTATION

To be presented for public discussion with the permission of the Faculty of Science of the University of Helsinki, in Auditorium A110, Department of Chemistry, A.I. Virtasen aukio 1, on the 25th of September, 2020 at 12 o'clock.

Helsinki 2020

Supervisors

Professor emeritus Markku Leskelä
Professor Mikko Ritala
Department of Chemistry
University of Helsinki
Helsinki, Finland

Reviewers

Professor J. Ruud van Ommen
Department of Chemical Engineering
Delft University of Technology
Delft, The Netherlands

Professor Harri Lipsanen
Department of Electronics and Nanoengineering
Aalto University
Espoo, Finland

Opponent

Professor Julien Bachmann
Department of Chemistry and Pharmacy
Friedrich-Alexander University Erlangen-Nürnburg
Erlangen, Germany

ISBN 978-951-51-6379-0 (paperback)
ISBN 978-951-51-6380-6 (PDF)
http://ethesis.helsinki.fi

Unigrafia

Helsinki 2020

“Keep pushing.”

Professor Matt Might,
University of Alabama at Birmingham

Abstract

The focus of this thesis is the development and optimization of atomic layer deposition (ALD) processes of cobalt oxide and copper oxide thin films. Emphasis is placed also on the characterization of the chemical and physical properties of the obtained thin films. As materials, cobalt oxides and copper oxides are semiconducting, and they also absorb visible light. Therefore, these materials are potentially useful to be utilized in various electronic, optical and catalytic applications.

ALD is a chemical gas-phase thin film synthesis technique that has several advantageous features, such as the ability to produce films with exceptional conformality on three-dimensional high aspect ratio structures, excellent uniformity of film thickness over large area substrates and accurate control of film thickness in a sub-nanometer range. The origin of these features is the unique film growth mechanism based on sequential and self-limiting gas-to-solid chemical reactions. In order to enable all the useful features of ALD in thin films deposition, the precursor chemistry must be studied, developed and above all, understood.

Studies related to cobalt and copper ALD precursors have largely focused on the deposition of metallic thin films due to their applicability in the microelectronics industry. ALD of cobalt oxide and copper oxide, on the other hand, has received significantly less attention. The contribution of this PhD thesis toward cobalt oxide and copper oxide thin film deposition is four ALD process development studies on these materials.

The $Co(BTSA)_2(THF) + H_2O$ process could be used to deposit CoO films at temperatures of 75 – 250 ºC. However, the films deposited using this precursor combination contained an increased amount of H, C and Si impurities that originated from the BTSA ligands. The amount of impurities increased with increasing deposition temperature which suggests that $Co(BTSA)_2(THF)$ is not an ideal precursor for cobalt oxide film deposition with ALD. In-situ reaction mechanism studies gave evidence toward that the film growth occurs via a ligand exchange mechanism.

The $Co^{t-Bu}(DAD)_2$ cobalt precursor was used together with O_3 to deposit cobalt oxide films. The optimal deposition temperature for this process was 120 ºC, at which polycrystalline and phase-pure Co_3O_4 thin films were obtained. The formation of mixed valence Co_3O_4 films from a Co(II) precursor occurred due to the high oxidative power of O_3. The Co_3O_4 films deposited at 120 ºC contained only a low amount of impurities, of which H was the most prominent at approximately a low 5 at-%. In photoelectrochemical studies, cobalt oxide nanoparticles were discovered to be efficient catalysts for the photoelectrochemical oxygen evolution reaction.

The $Cu(OAc)_2 + H_2O$ process produced crystalline Cu_2O thin films at temperatures close to 200 ºC. During the process development study, it was found that $Cu(OAc)_2$ is reduced to the volatile copper(I) acetate (CuOAc) when heated to its source temperature in ALD conditions. According to in-situ reaction mechanism studies and post-deposition film characterization, film growth proceeds via a ligand exchange route and results in the release of acetic acid as the reaction by-product. Elemental analysis of the films revealed that the Cu:O ratio of the films is close to the stoichiometric value of 2.0 and that the films contain exceptionally low amounts of impurities, 0.4 at-% H and ≤ 0.2 at-% C.

The $Cu(dmap)_2$ copper precursor was used at deposition temperatures of 80 – 140 ºC together with O_3. This ALD chemistry produced polycrystalline and phase-pure CuO thin films with relatively low amount of impurities, ≤ 3.0 at-% H, C and N at the optimal deposition temperature for this process, 120 ºC.

Preface

The work leading to these results was carried out in the Department of Chemistry at University of Helsinki between the years 2013 and 2020. This work has received funding from the "4G-PHOTOCAT" project supported by the European Commission's Seventh Framework Programme (FP7) for Research and Technological Development, the Centre of Excellence in Atomic Layer Deposition funded by the Academy of Finland and also from the Faculty of Science of University of Helsinki. The Doctoral Programme in Materials Research and Nanoscience (MATRENA) of University of Helsinki is acknowledged for support in the form of travel grants.

I wish to thank Professor Markku Leskelä for the opportunity to pursue a doctoral degree in materials chemistry. I'm grateful to Professor Leskelä for the great flexibility during this project and also for the support that was always there when needed. I also wish to thank Professor Mikko Ritala for his expertise, guidance and for meticulously proof-reading my manuscripts.

I wish to thank the official reviewers of this thesis, Professor J. Ruud van Ommen and Professor Harri Lipsanen for their valuable contribution toward finalizing the work. I also wish to thank Professor Julien Bachmann for accepting to act as the opponent in the public examination of my thesis.

During my PhD project, I had the privilege of working with many brilliant scientists. I was introduced to the world of ALD by Dr. Jani Hämäläinen and I don't think I could have had a better mentor. Thank you, Jani, for all your help. I also wish to thank Dr. Jiyeon Kim for our fruitful collaboration that led to the publication of three scientific articles. Mr. Mikko Heikkilä is thanked for the collaboration related to ALD of Cu_2O thin films as well as for all the help related to X-ray measurements. Moreover, I wish to thank Dr. Miika Mattinen for his contribution in AFM analyses. For SEM and EDX analyses and advice related to electron microscopy in general, I am thankful to Dr. Marianna Kemell and Mr. Georgi Popov. Mr. Popov also deserves thanks for designing and carrying out out the photo-conductivity measurements and his efforts for getting the Cu_2O manuscript published in ACS Omega. Mr. Mikko Kaipio and Ms. Heta-Elisa Nieminen are both thanked for their contribution in the reaction mechanism studies with QMS and QCM. Dr. Timo Hatanpää is thanked for his precursor synthesis efforts and help related to TGA. Dr. Benoît Marchand, Dr. Kenichiro Mizohata, Dr. Kristoffer Meinander and Professor Jyrki Räisänen from the Department of Physics at University of Helsinki are thanked for collaboration and their expertise in XPS and ToF-ERDA. I also want to thank all members of the 4G-PHOTOCAT consortium for the inspiring collaboration. Special thanks are deserved by Professor Radim Beranek, Professor Anjana Devi and Dr. Dariusz Mitoraj.

Working in the ALD research group has been a privilege and great fun. I wish to thank the former and current members of the group for creating such a wonderful work environment. Special thanks go to Elisa, Katja, Georgi and Miika at B316 for the supportive, unique and fun office spirit!

Finally, I want to thank my family for all the support during the years I have studied at University of Helsinki. I am grateful for all the encouragement from my parents Marja-Liisa and Jaakko. I also wish to extend my gratitude to Risto, Arja and Mauri and Elina for your friendship and support. Last, but certainly not least, I wish to thank Aino for all the love and understanding, and our daughter Taimi being the sunshine of my life.

Helsinki, July 2020

Tomi Iivonen

List of publications

This doctoral thesis consists of four original publications which are listed below. In the text, the publications are referred to by the Roman numerals **I – IV**. The contribution of the author is listed below each publication.

I T. Iivonen, J. Hämäläinen, B. Marchand, K. Mizohata, M. Mattinen, G. Popov, J. Kim, R.A. Fischer, M. Leskelä. Low-temperature atomic layer deposition of copper(II) oxide thin films, *Journal of Vacuum Science and Technology A* **34** (2016) 01A109. DOI: 10.1116/1.4933089

The author did all the film deposition experiments, performed the GI-XRD, XRR, UV-Vis and four-point probe measurements and analyzed the data. The author wrote the first draft of the manuscript and finalized it with contributions from all co-authors and according to suggestions from peer-review referees.

II J. Kim, T. Iivonen, J. Hämäläinen, M. Kemell, K. Meinander, K. Mizohata, L. Wang, J. Räisänen, R. Beranek, M. Leskelä, A. Devi. Low-temperature atomic layer deposition of cobalt oxide as an effective catalyst for photoelectrochemical water splitting devices, *Chemistry of Materials* **29** (2017) 5796 – 5805. DOI: 10.1021/acs.chemmater.6b05346

The author did the deposition experiments together with J. Kim. The author performed the GI-XRD, HT-XRD, FESEM, EDX, AFM and UV-VIS measurements/experiments and analyzed the data. J. Kim wrote the first draft of the manuscript. The manuscript was finalized by J. Kim and the author with contributions from all co-authors and according to suggestions from peer-review referees.

III T. Iivonen, M. Kaipio, T. Hatanpää, K. Mizohata, K. Meinander, J. Räisänen, J. Kim, M. Ritala, M. Leskelä. Atomic layer deposition of cobalt(II) oxide thin films from $Co(BTSA)_2(THF)$ and H_2O, *Journal of Vacuum Science and Technology A* **37** (2019) 010908. DOI: 10.1116/1.5066638

The author performed the majority of the film deposition experiments, and performed the TGA, GI-XRD and AFM measurements as well as analyzed the data. The author also contributed to the film thickness measurements using XRR, ellipsometry and UV-Vis spectrometry. The author assisted M. Kaipio in the in situ reaction mechanism studies and in the interpretation of the experimental results. The author wrote the first draft of the manuscript (excluding the section discussing the reaction mechanism studies). The manuscript was finalized by the author with contributions from all co-authors and according to suggestions from peer-review referees.

IV T. Iivonen, M. J. Heikkilä, G. Popov, H. Nieminen, M. Kaipio, M. Kemell, M. Mattinen, K. Meinander, K. Mizohata, J. Räisänen, M. Ritala, M. Leskelä. Atomic layer deposition of photoconductive Cu_2O thin films, *ACS Omega* **4** (2019) 11205 – 11214. DOI: 10.1021/acsomega.9b01351

The majority of the film deposition experiments was done by M. J. Heikkilä. The author contributed to the film deposition experiments, and did the AFM and UV-Vis measurements. The author designed the in situ reaction mechanism studies together with H. Nieminen and M. Kaipio. The first draft of the manuscript was written by the author (excluding the section discussing the photoconductivity studies). The manuscript was finalized by the author with contributions from all co-authors and according to suggestions from peer-review referees.

Other publications by the author

1. M. Buchalska, M. Surowka, J. Hämäläinen, T. Iivonen, M. Leskelä, W. Macyk. Photocatalytic activity of TiO_2 thin films on Si support prepared by atomic layer deposition, *Catalysis Today* **252** (2015) 14 – 19. DOI: 10.1016/j.cattod.2014.09.032

2. A. Hiltunen, T.-P. Ruoko, T. Iivonen, K. Lahtonen, H. Ali-Löytty, E. Sarlin, M. Valden, M. Leskelä, N.V. Tkachenko. Design aspects of all atomic layer deposited TiO_2 – Fe_2O_3 scaffold-absorber photoanodes for water splitting, *Sustainable Energy & Fuels* **2** (2018) 2124 – 2130. DOI: 10.1039/C8SE00252E

3. T.-P. Ruoko, A. Hiltunen, T. Iivonen, R. Ulkuniemi, K. Lahtonen, H. Ali-Löytty, K. Mizohata, M. Valden, M. Leskelä, N.V. Tkachenko. Charge carrier dynamics in tantalum oxide overlayered and tantalum doped hematite photoanodes, *Journal of Materials Chemistry A* **7** (2019) 3206 – 3215. DOI: 10.1039/C8TA09501A

4. M. Trochowski, M. Kobielusz, K. Mróz, M. Surówka, J. Hämäläinen, T. Iivonen, M. Leskelä, W. Macyk. How insignificant modifications of photocatalysts can significantly change their photocatalytic activity, *Journal of Materials Chemistry A* *7* (2019), 25142 – 25154. DOI: 10.1039/C9TA09400H

List of abbreviations and acronyms

acac	acetylacetonate
AFM	atomic force microscopy
ALD	atomic layer deposition
amd	amidinate
AZO	aluminum doped zinc oxide, ZnO:Al
BTSA	bis(trimethylsilyl)amido
Cp	cyclopentadienyl
CCTBA	hexacarbonyl(tert-butylacetylene)dicobalt
CVD	chemical vapor deposition
DAD	1,3-diazadienyl
dmamb	dimethylamino-2-methyl-butoxy
dmap	dimethylamino-2-propoxide
DMB	3,3-dimethyl-1-butene
EDX	energy dispersive X-ray spectroscopy
EL	electroluminescent
FESEM	field effect scanning electron microscopy
FTO	fluorine doped tin(IV) oxide, SnO_2:F
GI	grazing incidence
GPC	growth per cycle
hfac	hexafluoroacetylacetonate
HT-XRD	high temperature X-ray diffraction
ICPE	incident photon-to-current efficiency
i-Pr	isopropyl
IR	infrared
Me	methyl
MRI	magnetic resonance imaging
$^{n}Bu_3P$	tri-n-butylphosphane
NIR	near-infrared
NMR	nuclear magnetic resonance
OAc	acetate
OER	oxygen evolution reaction
PE-ALD	plasma-enhanced atomic layer deposition
QCM	quartz crystal microbalance
QMS	quadrupole mass spectroscopy
RBS	Rutherford backscattering spectroscopy
RHEED	reflection high energy electron diffraction
RMS, R_q	root-mean-square
RT	room temperature
RTA	rapid thermal annealing
s-Bu	sec-butyl
SLG	soda lime glass

t-Bu	tert-butyl
TCO	transparent conductive oxide
TFT	thin film transistor
TGA	thermogravimetric analysis
thd	2,2,6,6-tetramethyl-3,5-heptanedionate
THF	tetrahydrofuran
TMEDA	N,N,N',N'-tetramethylethylenediamine
TMVS	tetramethylvinylsilane
ToF-ERDA	time-of-flight elastic recoil detection analysis
UV	ultraviolet
Vis	visible
XRD	X-ray diffraction
XRF	X-ray fluorescence
XPS	X-ray photoelectron spectroscopy
XRR	X-ray reflectivity
Å	ångström, 10^{-10} m

Table of Contents

Abstract i

Preface iii

List of publications v

Other publications by the author vii

List of abbreviations and acronyms viii

Table of Contents x

1 Introduction 1

2 Background 2

2.1 Cobalt oxides 2

2.2 Copper oxides 4

3 Atomic layer deposition 7

3.1 Fundamentals of ALD 7

3.2. Temperature effects in film deposition 8

3.3 Effect of the oxygen source and reaction mechanisms 10

3.3.1 Water 10

3.3.2 Ozone 11

3.3.3 Molecular oxygen 12

4. ALD of cobalt oxide and copper oxide thin films 13

4.1 Cobalt oxides 13

4.1.1 Water processes 14

4.1.2 Ozone processes 15

4.1.3 Oxygen processes 18

4.1.4 Electrical and optical properties of ALD cobalt oxide films 19

4.1.5 Applications of ALD cobalt oxide films 19

4.2 Copper oxides 20
4.2.1 Water processes 21
4.2.2 Ozone processes 23
4.2.3 Electrical and optical properties of ALD copper oxide films 24
4.2.4 Applications of ALD copper oxide films 26
4.3 Ternary, quaternary and other complex cobalt oxides and copper oxides 27
5 Experimental 30
5.1 Film deposition 30
5.2 In situ reaction mechanism studies 30
5.3 Film characterization 31
6 Results and discussion 33
6.1 ALD of cobalt oxide thin films 33
6.1.1. $Co(BTSA)_2(THF) + H_2O$ [III] 33
6.1.2. $Co(^{t\text{-}Bu}DAD)_2 + O_3$ [II] 39
6.2. ALD of copper oxide thin films 41
6.2.1. $Cu(OAc)_2 + H_2O$ [IV] 41
6.2.2. $Cu(dmap)_2 + O_3$ [I] 45
6.3 Functional properties of CoO, Co_3O_4, Cu_2O and CuO films 50
6.3.1 Optical properties and band gap analysis 50
6.3.2 Photoelectrochemical water splitting 52
6.3.3 Photoconductivity 53
7 Conclusions 55
8 References 57

1 Introduction

Materials science is the study of properties of solid matter and the characterization of its chemical and physical properties. In the recent years, nanomaterials have emerged as an increasingly popular and important sub-field of materials science. The interest toward nanomaterials stems from their unique size-dependent properties which can be drastically different when compared to the same material in macroscopic form. Nanomaterials also hold great potential to be utilized in various technologies, such as electronics, optics, catalysis and medicine, among others.

Thin films, i.e. material layers which are limited to the nanometer scale in thickness, are a prime example of nanomaterials that have made the leap from research laboratories to consumer products. Currently, thin film technologies enable several important applications and devices, such as microelectronics, rechargeable batteries and solar cells.

When it comes to techniques for thin film synthesis, chemical gas-phase deposition methods have emerged as the most important ones due to their advantageous capability to coat complex three-dimensional geometries in a conformal manner. This feature is of critical importance for driving the miniaturization of electronics, batteries and other technologies forward. Of the gas-phase deposition techniques, the atomic layer deposition (ALD) method has proven to be unmatched for depositing high quality thin films which are not only conformal but also pinhole-free and uniform on large area substrates. Furthermore, thicknesses of thin films deposited with ALD can be controlled very precisely, often in the sub-nanometer range. Together, these features make ALD an invaluable tool for modern nanotechnology.

The goal of this dissertation work was to develop and study new ALD chemistries that can be used to deposit cobalt oxide and copper oxide thin films. These materials exhibit semiconductivity and also absorb visible light, which makes them potential candidates to be utilized in diverse electronic, optical and catalytic applications. The focus of the work lies in ALD process development, which consists of studying how the choice of precursor molecules and different process parameters affect the chemical and physical properties of the obtained thin films. The contribution of this work toward advancing the fields of nanomaterials and thin film technology consists of four ALD process development studies; two for cobalt oxide thin films and two for copper oxide thin films.

The contents of this thesis are organized in the following manner. Chapter 2 gives an introduction to some fundamental properties of cobalt oxide and copper oxide thin films as well as to some of their applications. Chapter 3 contains an introduction to ALD and Chapter 4 reviews the current state of ALD of cobalt oxide and copper oxide thin films as well as their properties and applications. Chapter 5 describes the experimental techniques employed throughout the work and Chapter 6 summarizes the main results of the four ALD process development studies conducted in the course of this work. Finally, concluding remarks and an outlook are given in Chapter 7.

2 Background

This chapter contains an introduction to the chemical and physical properties of cobalt oxides and copper oxides. Included is also a brief discussion on some possible applications of cobalt oxide and copper oxide thin films.

2.1 Cobalt oxides

Cobalt is a first-row transition metal with an electron configuration [Ar] $3d^7\ 4s^2$. Cobalt cations have two primary oxidation states, Co^{2+} and Co^{3+} from which Co^{2+} is more common. The corresponding, chemically stable cobalt oxides are the monoxide, CoO and the mixed valence oxide Co_3O_4. The mixed valence oxide contains both Co^{2+} and Co^{3+} ions in a stoichiometry of $Co^{2+}Co_2^{3+}O_4$. Pure cobalt(III) oxide, Co_2O_3, is not a stable compound.

Cobalt monoxide crystallizes in the cubic rock-salt structure.[1] Nanocrystalline CoO can also exist in a hexagonal form similar to the wurtzite-type structure, especially in the case of nanoparticles and nanocrystalline thin films.[2–5] Co_3O_4, on the other hand, crystallizes in the normal spinel structure.[6] In this structure, oxygen ions form a face centered cubic lattice and Co^{2+} and Co^{3+} ions reside at the interstitial tetrahedral and octahedral sites, respectively. Representative unit cell structures of the three cobalt oxides are shown in Figure 1.

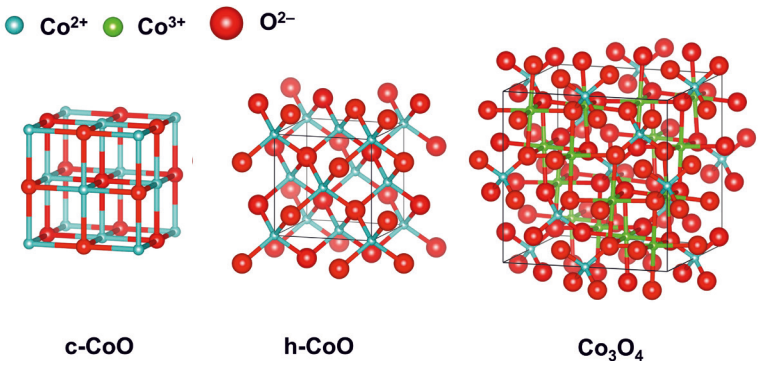

Figure 1. Unit cells of cubic CoO, hexagonal CoO and cubic spinel Co_3O_4.

Reports on the electrical properties of CoO are contradictory as this material has been classified to be both semiconducting and insulating.[7–10] The resistivity of single crystal CoO has been noted to be as high as $10^{10}\ \Omega$ cm, which indicates that this material is an electrical insulator.[8] However, the conductivity of CoO increases with increasing temperature, which is characteristic to semiconductors. Based on both theoretical and experimental studies, CoO has been classified as a charge-transfer insulator with a wide band gap of 5 – 7 eV.[9–11]

CoO also absorbs light at wavelengths of 440 – 500 nm which correspond to photon energies of 2.5 – 2.8 eV.

Co_3O_4, on the other hand, is a p-type semiconductor.[12–14] The p-type conductivity in Co_3O_4 originates from cobalt vacancies in the crystal lattice, which create electron acceptor states within the band gap.[13] The electrical resistivity of polycrystalline Co_3O_4 thin films is in the order of $10^{-1} – 10^2$ Ω cm,[12,14] which is significantly lower than the values reported for CoO. The optical properties of Co_3O_4 in the UV–Vis–NIR wavelength range are linked to absorption events that correspond to charge transfer between the Co^{2+} and the Co^{3+} ions as well as excitation of electrons from the valence band to the conduction band.[15] Charge transfer between the cobalt cations occurs at photon energies of 0.7 – 1.8 eV,[15] while the excitation of electrons from the valence band to the conduction band occurs at photon energies of 2.0 – 2.6 eV.[12,15]

CoO can be oxidized to Co_3O_4 by annealing in an oxygen containing atmosphere.[16] Depending on the partial pressure of oxygen, CoO will oxidize to Co_3O_4 at temperatures of 300 – 500 °C. Raising the annealing temperature to 600 °C under N_2 has been reported to result in a reduction of Co_3O_4 back to CoO. If Co_3O_4 is annealed under high vacuum, the onset temperature for reduction to CoO is 300 °C.[12] In addition to the pure oxides, CoO and Co_3O_4, cobalt also forms various hydroxides and oxyhydroxides, such as $Co(OH)_2$ and CoOOH.[17] These hydroxides and oxyhydroxide species can form spontaneously on cobalt oxide surfaces upon exposure to moisture.[18,19] Upon annealing in inert conditions, cobalt hydroxides and oxyhydroxides decompose to either CoO or Co_3O_4.[17]

Cobalt oxide thin films can be utilized in several applications associated with energy storage and conversion, as well as in catalysis, resistive switching,[20,21] magnetic materials[21] and gas sensing,[22] among others. Perhaps the most prominent application for cobalt oxide is found in lithium ion batteries. By means of lithiation, both CoO and Co_3O_4 can be converted to $LiCoO_2$ which is used as a cathode material in high energy density lithium ion batteries.[23,24] Moreover, (meso)porous cobalt oxide thin films find use as electrodes in electrochemical supercapacitors.[25,26] In contrast to high energy density batteries, supercapacitors have high power densities and therefore supercapacitors can function as a complementary technology in energy storage and release.

Cobalt oxides, hydroxides and oxyhydroxides have proven to be efficient catalysts for the oxygen evolution reaction (OER).[27–29] The ability of these materials to transform H_2O to O_2 originates from the rich redox chemistry of cobalt, which can facilitate the formation of cobalt superoxide surface species that can be oxidized to transformed to molecular oxygen by photogenerated holes.[29] Moreover, cobalt oxide nanoparticles and overlayers have shown to be efficient co-catalysts in electrochemical water splitting based on n-type semiconductor photoanodes, such as TiO_2 and Fe_2O_3.[30,31]

In addition to the simple binary cobalt oxides, CoO and Co_3O_4, ternary, quaternary, doped and other cobalt containing oxide materials are of interest due to their electrical, optical and magnetic properties. For example, the in-plane resistivity of single crystalline, delafossite

class $PdCoO_2$ and $PtCoO_2$ can be as low as 2×10^{-6} Ω cm, i.e. lower than those of the parent noble metals and practically as low as the resistivity of copper, 1.7×10^{-6} Ω cm.[32] The spinel structured nickel cobalt oxide, $Ni_xCo_{3-x}O_4$ is another example of a conductive oxide.[33–35] The resistivity of this material depends on the degree of Ni substitution in the Co_3O_4 lattice and is in the order of 10^{-3} Ω cm. Moreover, nickel cobalt oxides retain p-type semiconductivity and are also ferromagnetic.[35] Other cobalt containing oxides exhibiting ferri- or ferromagnetism include cobalt iron oxides,[36] cobalt manganese oxides[37] and lanthanum cobalt oxides,[38] among others. What is more, ternary and more complex layered cobalt oxides, such as $Ca_3Co_4O_9$, are thermoelectric materials with high figures of merit for converting heat to electricity.[39,40]

2.2 Copper oxides

Like cobalt, copper is also a first-row transition metal. The electron configuration of copper is [Ar] $3d^{10}$ $4s^1$ and common compounds of Cu exist at oxidation states of +1 and +2. The oxides corresponding to Cu^+ and Cu^{2+} are Cu_2O and CuO, respectively. In ternary and quaternary cuprates, copper can exist also as Cu^{3+}.[41] Of the binary copper oxides, Cu_2O crystallizes in a simple cubic structure, while CuO assumes the monoclinic tenorite structure (Figure 2).

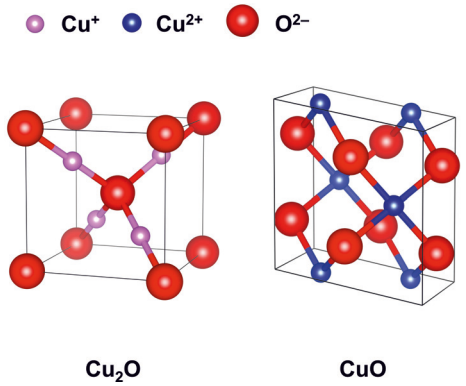

Figure 2. Unit cells of cubic Cu_2O and monoclinic CuO.

In addition to Cu_2O and CuO, a mixed valence copper oxide, Cu_4O_3, is also known.[42] Cu_4O_3 is considered to be a metastable material, as CuO and Cu_2O impurity phases are easily formed during its synthesis and post-synthesis annealing.[43,44]

Cu_2O and CuO are both p-type semiconductors.[45,46] Similarly to the cobalt oxides, the p-type semiconductivity in copper oxides originates from intrinsic Cu vacancies in the crystal lattices of these compounds.[47] Of the two copper oxide variants, Cu_2O has been studied significantly more due to its advantageous electrical and optical properties.

The electrical properties reported for Cu_2O thin films show large variance depending on sample morphology and grain size. Resistivities of polycrystalline Cu_2O thin films are generally in the range of $10^2 – 10^5$ Ω cm.[48,49] A high degree of crystallinity and large grain size haven been reported to result in low resistivity. The Hall mobility of holes in polycrystalline Cu_2O thin films varies between 5 – 60 $cm^2\ V^{-1}\ s^{-1}$ and high mobility is observed for films with a high degree of crystallinity.[48,49] In the case of epitaxial Cu_2O deposited on MgO substrates by sputtering, Hall mobility of holes up to 90 $cm^2\ V^{-1}\ s^{-1}$ have been obtained.[50] The band gap of Cu_2O is approximately 2.1 – 2.2 eV.[51,52] This photon energy range corresponds to the visible wavelengths which makes Cu_2O an interesting material for solar energy applications.

While the monoxide of copper, CuO, has received less attention than Cu_2O, reports on the electrical and optical properties of CuO are still found in the literature. The resistivity of polycrystalline CuO thin films is in the range of $10^0 – 10^3$ Ω cm and the Hall mobility of holes in polycrystalline CuO thin films is < 7 $cm^2\ V^{-1}\ s^{-1}$.[53–56] The band gap of bulk CuO is approximately 1.4 eV.[57]

The oxidation state of copper in its oxides can be controlled by annealing.[44] In an oxygen containing atmosphere, the oxidation of Cu_2O occurs at temperatures of approximately 300 °C, whereas CuO can be reduced to Cu_2O by vacuum annealing at 600 – 700 °C. Concerning the hydroxides of copper, Cu(I) hydroxide, CuOH, is not stable and decomposes to Cu_2O and water.[58] $Cu(OH)_2$ is a stable compound that starts to decompose to CuO and H_2O at temperatures of 150 °C and higher.[59]

The applications of copper oxide thin films are often related to energy production. As copper oxides are Earth-abundant materials and of low cost, they have been considered to be used in low-cost solar cell technologies.[60,61] Another widely studied application is the use of Cu_2O as a photocathode in electrochemical water splitting.[62] While Cu_2O appears to be an ideal material for the hydrogen evolution reaction from the point of view of its band gap, it suffers from photocorrosion that results in a gradual decrease in performance due to the formation of Cu and CuO impurity phases.[63] However, recent studies have shown that the photocorrosion of Cu_2O under electrochemical conditions can be mitigated by protecting the photocathode surface with ultrathin capping layers, such as Al-doped ZnO (AZO) and TiO_2.[64,65]

Cu_2O has been also considered as a p-type channel material in thin film transistor (TFT) structures.[66–68] In this context, low-temperature deposition of amorphous Cu_2O thin films is of particular interest, as this approach is a possible pathway to enable flexible electronics.[69]

In addition to the binary oxides, copper forms numerous ternary and quaternary oxides, such as the delafossite class $CuMO_2$ compounds and the layered cuprates, $MCuO_3$ and M_2CuO_4. Similarly to Cu_2O, most of the $CuMO_2$ delafossites exhibit p-type semiconductivity.[46] Importantly, the choice of the metal M in these compounds can be used to modify both the electrical and optical properties of the material. In comparison to binary Cu_2O, some copper delafossites, for example $CuAlO_2$,[70] $SrCu_2O_2$[71] and (magnesium doped) $CuCrO_2$[72,73] exhibit

good electrical conductivity and are also optically transparent due to their wide band gaps of approximately 3.1 – 3.5 eV. Due to this combination of electronic and optical properties, $CuAlO_2$, $SrCu_2O_2$ and $(Mg)CuCrO_2$ are classified as transparent conductive oxides (TCO). Recently, studies on copper containing p-type TCOs has attracted increasing attention due to their potential in next generation photovoltaics.[74] Another prospective use for p-type TCOs is to combine them with the common n-type TCOs for creating pn-junctions and eventually, low-cost transparent electronics.[75,76]

Layered cuprates, such as $(Sr)La_2CuO_4$,[77] $YBa_2Cu_3O_{7-x}$[78] and $Hg_2Ba_2Ca_2Cu_3O_{8+x}$,[79] are known to exhibit superconductivity at temperatures achievable with liquid nitrogen cooling. Thin films of these materials are interesting with respect to many applications based on superconductive electromagnets, such as magnetic resonance imaging (MRI), nuclear magnetic resonance (NMR) and magnetic levitation.[80]

3 Atomic layer deposition

3.1 Fundamentals of ALD

ALD is a chemical gas-phase deposition method that can be used for creating high quality thin films of various materials, including oxides, chalcogenides, nitrides, halides and metals.[81,82] In the recent years, both the chemistry and technology aspects of ALD have emerged as a topic of ever increasing interest among researchers, chemical companies and notably, the semiconductor industry.[83–85]

From the point of view of industrial applicability, the most prominent research topics in modern ALD technology involve metallization,[86] high-k oxides,[84,87] lithography,[88] photovoltaics,[89] microelectromechanical systems (MEMS)[90] and optical coatings.[84] Other, emerging topics in ALD are 2D materials,[91,92] lithium-ion batteries,[93,94] catalysis[95] and medical technologies.[96] The reason why ALD can enable advances in many of these technologies is its unmatched ability to produce continuous, pinhole-free thin films that are uniform over a large surface area and also conformal on complex three-dimensional substrates.[81]

As a thin film deposition method, ALD is based on self-limiting gas-to-solid reactions that take place on the surface of a substrate. The self-limiting film deposition mode characteristic to ALD can be achieved by 1) finding a suitable combination of film-forming precursor molecules, 2) pulsing the gaseous film-forming precursors to the substrate in a sequential manner, 3) ensuring that the precursors do not react in the gas phase by separating the precursor pulses with purging periods, 4) choosing appropriate process parameters, such as precursor pulse times and deposition temperature.

Film growth in ALD occurs in cycles. For a simple binary film deposition process, these cycles consist of precursor pulses for precursor A and precursor B as well as purging periods for each precursor. Ideally, when the precursor A is pulsed to a substrate, it will either react with surface groups or adsorb on the surface. Once all available surface groups have reacted or all adsorption sites have been filled, no further material will be deposited. In other words, the film growth is self-limiting. The first precursor pulse is followed by a purge with an inert gas, during which unreacted precursor molecules and any possible surface reaction by-products are removed from the vicinity of the subtrate. After the purging period, precursor B is pulsed to the substrate where it reacts with the new surface species formed from precursor A. During the pulse of precursor B, a new monolayer or a fraction of a monolayer of material in the form of a thin film is formed. Finally, a second purge period is used to remove unreacted molecules of precursor B as well as the reaction by-products. This completes the ALD cycle.

The amount of material deposited during one ALD cycle is referred to as the growth rate or the growth per cycle (GPC) value. Typically, the GPC of an ALD process is measured in the order of ångströms (Å, 10^{-10} m), which signifies that the thickness of ALD thin films can be controlled in the sub-nanometer range.

As ALD is based on surface chemistry, the choice of precursors plays an important role in the film deposition. The main requirements for ALD precursors are volatility, thermal stability and sufficient reactivity.[97] For depositing metal oxide films, one of the precursors must contain a metal atom, while the other precursor acts as the oxygen source.[98] The same analogue applies also for the deposition of chalcogenides, nitrides and halides.[82] For depositing metallic films, different reducing agents, such as molecular hydrogen or compounds that can form hydrogen radicals, can be utilized.[99,100] Thin films of noble metals can also be deposited by using molecular oxygen or ozone as the co-reactant. This type of ALD chemistry results in the formation of noble metal oxides that are not stable under the deposition conditions and decompose to pure metals.[98]

In addition to film deposition driven solely by thermal energy, various energy enhanced variants of ALD have been developed.[101] In plasma-enhanced ALD (PE-ALD), one of the precursors is either a reductive or an oxidative plasma.[102] This approach enables the deposition of metals, oxides and other materials not necessarily achievable by thermal ALD. PE-ALD can enable film deposition at lower temperatures than thermal ALD which is useful for depositing thin films on substrates that have a limited thermal stability, such as polymers. More recently emerged variants of ALD include photo-assisted ALD and electron-enhanced ALD, in which one of the "precursors" is either UV-Vis photons [103] or electrons.[104]

3.2. Temperature effects in film deposition

In thermal ALD, film deposition is done at temperatures that are well above RT in order to ensure sufficient reactivity during the film-forming surface reactions.[81] The effects of deposition temperature are commonly represented by a plot of GPC as a function of the reaction temperature. A graph displaying some of the trends in GPC with changing deposition temperature is presented in Figure 3. These effects can be divided into two categories; those originating from the chemical and physical properties of the precursor molecules and those associated with the substrate or the deposited material.

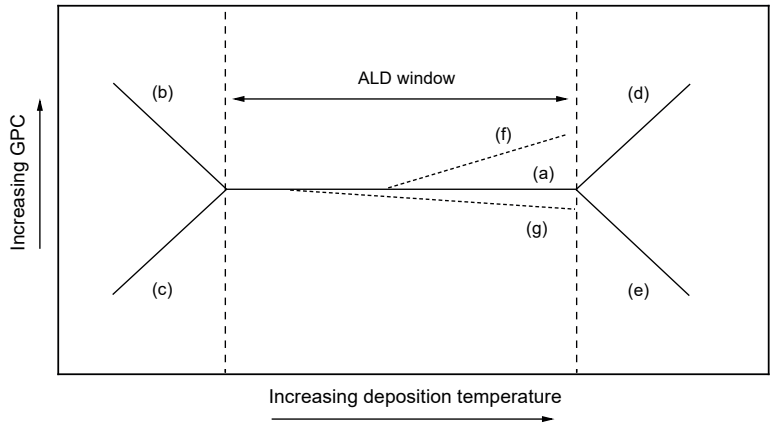

Figure 3. Effect of deposition temperature to GPC in ALD.

The temperature range where film growth proceeds in a self-limiting manner and without detrimental decomposition of precursors is referred to as an ALD window (a).[83] At deposition temperatures below the ALD window, low vapor pressure precursors can condense on the film surface, which leads to the deposition of more than one monolayer per cycle (b). Precursor condensation can also lead to the incorporation of precursor ligands in the films, which signifies the formation of impure and non-stoichiometric films. On the other hand, a too low deposition temperature can also diminish the reactivity of the precursors. This effect is observed as decreased GPC values (c). Increasing the deposition temperature can be used to resolve both (b) and (c). However, increasing the deposition temperature too much can lead to either thermal decomposition (d) or desorption of precursor molecules (e). The thermal decomposition of a precursor causes material to be deposited continuously, similarly to CVD. In such a case, the advantages originating from the self-limiting growth mode are lost. Furthermore, thermal decomposition of a metal precursor can be reductive, which can result in the formation of films which contain both oxide and metallic phases.[82] In certain ALD processes, GPC can either increase (f) or decrease (g) within the ALD window. These phenomena are explained by the fact that the number of adsorption sites on the growth surface depends on temperature. (f) is commonly observed in noble metal ALD where O_2 is used as the co-reactant and is related to the uptake of atomic oxygen in the films. Possible effects in (g) are the densification of the deposited film,[101] the thermal decomposition of surface hydroxyls[105] and for ALD processes based on O_3, the decomposition of O_3 to the less reactive O_2.[106]

3.3 Effect of the oxygen source and reaction mechanisms

The most commonly used oxygen sources in thermal ALD of metal oxide thin films are H_2O and O_3.[82] In some examples, molecular oxygen, O_2 , "wet oxygen", i.e. a mixture of H_2O vapor and O_2,[107,108] as well as primary alcohols and H_2O_2 have also been utilized.[82,109] Not all metal precursors are reactive towards H_2O, O_2 or alcohols, while O_3 is a more universal oxygen source due to its high reactivity. Depending on the chemistry of the metal precursor ligands and the choice of the oxygen source, film growth can proceed through ligand exchange, ligand combustion or a combination of the two.[98]

The surface reactions of ALD processes can be studied *in-situ* using different techniques, such as quadrupole mass spectroscopy (QMS), quartz crystal microbalance (QCM) and infrared (IR) spectroscopy.[105,110] For understanding the surface chemistry of ALD processes, QMS and IR spectroscopy are particularly useful techniques, as they can be applied to identify the by-products of the film deposition reactions. QCM, on the other hand, can be used to easily determine if a precursor is decomposing upon adsorption. When it comes to solving reaction mechanisms of ALD processes, the utilization of two or more complementary *in-situ* techniques usually gives the best result.[98]

3.3.1 Water

In ALD chemistry where H_2O is used as the oxygen source, the primary reaction mechanism is an exchange reaction between the ligands of the metal precursor and the surface hydroxyl groups.[98] These reactions result in a formation of new chemical bonds between metal atoms and oxygen atoms as well as the release of protonated ligands as by-products.The ligand exchange reactions can occur during both the metal precursor pulse and the H_2O pulse. A schematic of the ligand exchange process is shown in Figure 4.

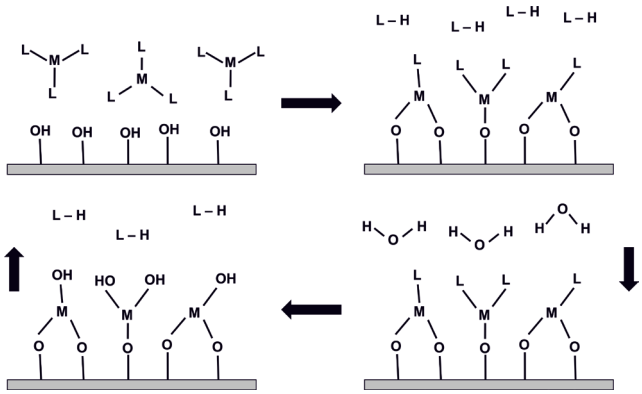

Figure 4. A schematic showing the different steps in metal oxide film deposition in ALD when H_2O is used as the oxygen source. M = metal cation, L = a ligand that can be protonated.

If there are no hydroxyl groups on the surface, metal precursors can still undergo molecular adsorption.[111] This mechanism is valid at deposition temperatures where the surface hydroxyls undergo thermal decomposition to a bare metal oxide terminated surface.[105,112] In the case of molecular adsorption of the metal precursor, the ligand exchange reactions will occur only during the H_2O pulse.[98] The adsorption of a metal precursor can also be dissociative, during which metal-ligand bonds break without the exchange reaction. If the dissociated ligands form a strong chemical bond with the surface, they can remain in the film as impurities.

The main advantage of using H_2O as the oxygen source is the feature of removing the metal precursor ligands intact. This approach can be used to avoid the incorporation of ligand fragments as impurities. Other advantages of H_2O include its ready availability, ease of use and non-toxicity. The disadvantages associated with H_2O based ALD chemistry are related to extremely low and high deposition temperatures. At low temperatures ($\leq$ 100 °C), water molecules can remain on the film surface as well as on the ALD reactor walls due to high activation energy of desorption.[81] This signifies that long purging times are required to ensure that film growth proceeds in the ALD mode. Consequently, ALD metal oxide films deposited using H_2O at low temperatures often contain an increased amount of hydrogen impurities.[113] The disadvantages of high temperature deposition are related to surface dehydroxylation, which has been noted to cause a decrease in GPC due to diminished amount of surface groups available for ligand exchange reactions.[98]

3.3.2 Ozone

In ALD metal oxide processes based on using O_3 as the oxygen source, the primary reaction mechanism is ligand combustion.[98] In this mechanism, atomic oxygen and oxygen radicals, which are formed from O_3 molecules, oxidize the ligands of surface-bound metal precursors. These reactions result in the formation of oxygen to metal chemical bonds as well as combustion by-products. For metal-organic and organometallic precursors, the combustion by-products are low-molecular mass molecules derivable from their ligands, such as CO_2, H_2O and oxides of nitrogen. O_3 is also reactive toward metal halide precursors, such as chlorides and iodides.[114,115] This deposition approach is useful for obtaining films that are free of hydrogen and carbon impurities. A schematic of ligand combustion chemistry during the O_3 pulse is shown in Figure 5.

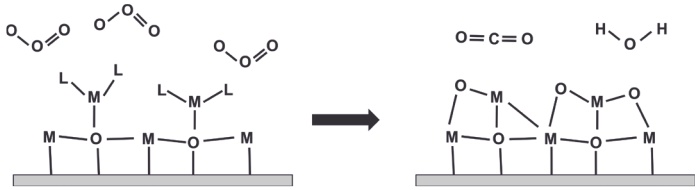

Figure 5. A schematic showing the combustion of the ligands of surface bound metal precursor molecule. L is a metal-organic or an organometallic ligand.

Due to its high reactivity, O_3 can enable film deposition with metal precursors that are not reactive toward H_2O.[82] Importantly, the redox chemistry of O_3 in ALD does not only combust the ligands of the metal precursor molecules, but also oxidizes the metal atoms in the deposited films to high oxidation states. This effect is particularly important in ALD of transition metals that have several stable oxidation states, such as cobalt and copper. While the O_3 based ALD chemistry can be used to deposit films of several transition metal oxides, phase control of the deposited material is often lost.

The high oxidation power of O_3 can also affect substrates. For example, H terminated Si surfaces are readily oxidized to SiO_2 by O_3 already at room temperature.[116] Similarly for other common substrates in ALD, such as metals or TiN, they can be oxidized by O_3 which can be detrimental with respect to device performance.

Another important effect in ALD of metal oxides is the surface-mediated decomposition of O_3.[106,117] This effect is particularly noticeable on p-type metal oxide surfaces as these materials are efficient catalysts for O_3 decomposition.[117] By using MnO_2 as a model catalyst, it was shown that the reaction between O_3 and atomic oxygen that results in the formation of O_2 is catalyzed by the p-type metal oxide surface.[118,119] As O_2 is far less reactive than O_3, this effect can lead to the deposition of films that are non-uniform and not conformal.[14,106] As the combustion of the ligands of metal precursor molecules and the decomposition of O_3 are competing processes, excessively long oxygen source pulse times can be required in ALD processes where O_3 is used. The decomposition of O_3 in ALD conditions is accelerated at high temperatures.[106] Conversely, lowering the deposition temperature can be used to mitigate this effect.

3.3.3 Molecular oxygen

Molecular oxygen is less reactive than O_3 and therefore the use of O_2 as the oxygen source in thermal ALD is limited to only few precursor combinations and materials. Possible routes for O_2 based thermal ALD of metal oxides include the use of high deposition temperatures or highly reactive metal precursors. Both approaches have notable disadvantages, which include the possible thermal decomposition of the metal precursor and difficulties in obtaining self-limiting growth.

Moreover, O_2 can be also used to deposit noble metal thin films, such as platinum or ruthenium, that can catalyse the dissociation of O_2 to form atomic oxygen.[99] In this approach, the ligands of the noble metal precursor are combusted by atomic oxygen created *in-situ* on the surface of the deposited noble metal film.

4. ALD of cobalt oxide and copper oxide thin films

This chapter reviews the ALD processes for cobalt oxide and copper oxide thin films. The thin film deposition chemistries summarized here are categorized based on whether H_2O, O_3 or O_2 was used as the oxygen source. This chapter also includes an overview of the functional properties and applications of ALD cobalt oxide and copper oxide thin films.

4.1 Cobalt oxides

A total of 14 cobalt precursors have been used to deposit cobalt oxide thin films with ALD. The molecular structures of these precursors are shown in Figure 6.

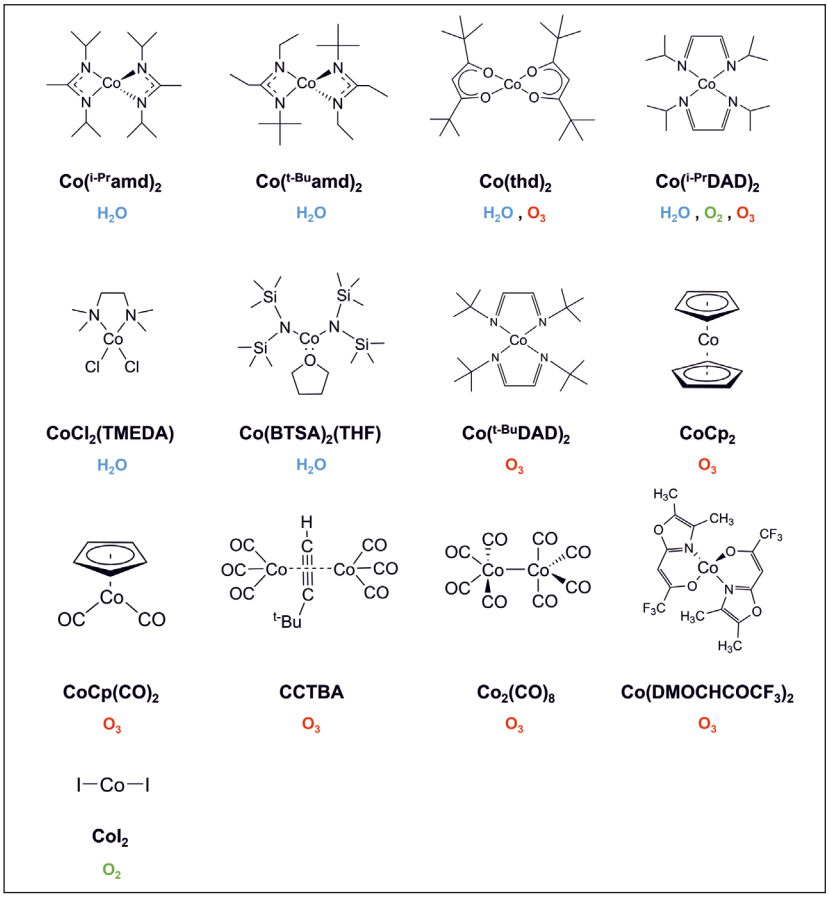

Figure 6. Chemical structures of precursors utilized in ALD of cobalt oxide thin films. The oxygen source(s) used with each precursor have been listed below the name of the molecule.

4.1.1 Water processes

Six of the cobalt precursor molecules in Figure 6 are reactive toward H_2O. The main ALD process parameters, including the deposition temperature range, GPC, saturation characteristics and the phase of the obtained films are compiled in Table 1. The oxidation state of cobalt in all these compounds is +2. As H_2O is not a strong oxidant, the deposition of CoO films can be expected. However, some of these cobalt precursors have been reported to produce Co_3O_4 containing films or even single phase Co_3O_4 at elevated deposition temperatures.

Table 1. Characteristics of ALD cobalt oxide processes based on using H_2O as the oxygen source. N.R. = not reported.

Precursor	Deposition temperature (°C)	GPC (Å)	Saturation	Phase of the deposited films	Ref.
$Co(^{i-Pr}amd)_2$	170 – 180, 250	0.4	N.R.	CoO	120,121
$Co(^{t-Bu}amd)_2$	180 – 270	N.R.	N.R.	CoO	122,123
$Co(thd)_2$	162 – 283	N.R.	N.R.	CoO, Co_3O_4	124
$Co(^{i-Pr}DAD)_2$	200 – 300	N.R.	N.R.	CoO + Co_3O_4, Co_3O_4	125
$CoCl_2$(TMEDA)	225 - 275	0.06 – 0.38	yes	CoO, CoO + Co	5
Co(BTSA)$_2$(THF)	75 – 250	0.2 – 1.2	yes	CoO, $Co(OH)_2$	**III**

The $Co(^{i-Pr}amd)_2$ precursor has been used together with H_2O for depositing cobalt oxide films at 170 – 180 °C and 250 °C.[120,121] Even though this ALD chemistry has been utilized by several authors, no saturation studies exist for this process. In addition, no report on the thermal stability of $Co(^{i-Pr_2}amd)_2$ has been given. Nevertheless, this precursor combination can be used to deposit stoichiometric and crystalline cubic CoO films as determined with, X-ray diffraction (XRD), Rutherford backscattering spectrometry (RBS) and reflection high-energy electron diffraction (RHEED) measurements. Furthermore, the CoO films were noted to grow epitaxially on strontium titanate surfaces.[121]

$Co(^{t-Bu}amd)_2$, another cobalt amidinate precursor, is also reactive toward H_2O.[122,123] This precursor combination has been used for cobalt oxide film deposition at temperatures of 180 – 270 °C. Photoelectron spectra of films deposited at 180 – 270 °C show that these films are of the CoO phase. Interestingly, the O 1s binding energy region spectra for films deposited at 180 °C showed only a single peak assignable to the lattice oxygen of CoO, which suggests that the films are free from hydrogen impurities. Increasing the deposition temperature to 305 °C and higher was reported to result in reductive decomposition of $Co(^{t-Bu}amd)_2$ and the formation of metallic Co in the films. Based on RHEED measurements, CoO films deposited from $Co(^{t-Bu}amd)_2$ + H_2O are polycrystalline cubic CoO on thermal SiO_2 and epitaxial on single crystalline MgO.

The $Co(thd)_2$ precursor has been used to deposit cobalt oxide thin films with H_2O as the oxygen source,[124] even though metal β-diketonates are usually not reactive towards water vapour in ALD conditions.[82] The GPC value for the $Co(thd)_2$ + H_2O ALD process, however, is significantly low, only 0.03 – 0.06 Å at 162 – 259 °C. A GPC value this low effectively

renders this process impractical for depositing continuous films. The phase of the cobalt oxide films deposited with this process was noted to be dependent on the deposition temperature.[124] At 186 °C, polycrystalline cubic CoO films were obtained whereas increasing the deposition temperature to 210 – 235 °C resulted in the formation of polycrystalline Co_3O_4. The cobalt oxide films deposited 259 °C were reported to be contain both CoO and Co_3O_4.

The diazadienyl cobalt(II) compound, $Co(^{i\text{-}Pr_2}DAD)_2$ has been used together with H_2O at deposition temperatures of 200 – 300 °C.[125] Information on the ALD characteristics of the $Co(^{i\text{-}Pr_2}DAD)_2 + H_2O$ process is limited, as the main focus in the studies on this cobalt precursor has been its reactivity towards O_2 and O_3.[125,126] According to XRD measurements, the films deposited from $Co(^{i\text{-}Pr_2}DAD)_2 + H_2O$ are amorphous at 200 °C, a mixture of CoO and Co_3O_4 phases at 225 °C, and Co_3O_4 at deposition temperatures of 250–300 °C.[125] The oxidation of cobalt from Co^{2+} to Co^{3+} in a water assisted ALD process is unusual and may be related to redox effects caused by the $^{i\text{-}Pr}$DAD ligands.

$CoCl_2$(TMEDA) is a diamine adduct of cobalt(II) chloride. On its own, $CoCl_2$ does not have a sufficient vapor pressure to be used as precursor in ALD, but adducting $CoCl_2$ with TMEDA enables film deposition at temperatures of 225 °C and above.[5] Saturative growth with respect to both the cobalt precursor and H_2O was confirmed at a deposition temperature of 275 °C. Films deposited using $CoCl_2$(TMEDA) + H_2O at 225 – 275 °C were reported to be of the CoO phase whereas films deposited at 300 °C were a mixture of CoO and metallic Co due to partial decomposition of the cobalt precursor. At deposition temperatures below 300 °C the films were polycrystalline CoO and contained both the cubic and hexagonal phases. These films were noted to contain large out-of-plane, pyramid-like grains that caused an increase in surface roughness. For 50 nm thick films deposited at 250, 275 and 300 °C, the average RMS roughness were 9 – 12 nm. According to Time-of-Flight Elastic Recoil Detection Analysis (ToF-ERDA) and X-ray photoelectron spectroscopy (XPS) studies, the Co:O stoichiometry of films deposited at 250 and 275 °C was close to 1.0, the films contained ≤ 1.2 at-% of H, C, N and Cl impurities, and the oxidation state of cobalt was +2.

4.1.2 Ozone processes

ALD of cobalt oxide with O_3 as the oxygen source has been demonstrated with eight cobalt precursors (Figure 6). Due to the high oxidation power of O_3, cobalt oxide films deposited using this oxygen source are primarily of the Co_3O_4 phase. The main parameters for cobalt oxide ALD processes based on O_3 are listed in Table 2.

Table 2. Characteristics of ALD cobalt oxide processes based on O_3. N.R. = not reported.

Precursor	Deposition temperature (°C)	GPC (Å)	Saturation	Phase of the deposited films	Ref.
$Co(thd)_2$	186 – 400	0.2	yes	Co_3O_4	127–129
$CoCp_2$	125 – 331	0.25 – 0.5	yes	Co_3O_4, Co + Co_3O_4	14,130–132
$CoCp(CO)_2$	50 – 200	0.8 – 1.1	yes	Co_3O_4	133
CCTBA	68 – 138	0.8 – 4.4	yes	CoO + Co_3O_4	134
$Co_2(CO)_8$	50	6.0	no	CoO + Co_3O_4	135
$Co^{i\text{-}Pr}(DAD)_2$	120 – 250	0.9 – 1.2	yes	Co_3O_4	126
$Co(DMOCHCOCF_3)_2$	150 – 200	0.1 – 0.2	no	Co_3O_4	136
$Co(^{t\text{-}Bu_2}DAD)_2$	100 – 150	0.45 – 1.2	yes	Co_3O_4	**II**

The $Co(thd)_2$ + O_3 ALD chemistry has been used to deposit cobalt oxide films at temperatures of 186 – 400 °C.[127–129] The onset of thermal decomposition of $Co(thd)_2$ is approximately 310 °C, above which the GPC of this process starts to increase sharply.[128] Based on saturation studies, film growth is self-limiting at 186 °C with respect to both precursors with a GPC of 0.20 Å. Films deposited on Si substrates at 186 – 283 °C were polycrystalline Co_3O_4,[127,128] whereas registry between the substrate and the deposited film was reported for single crystalline MgO, $SrTiO_3$ and α-Al_2O_3.[129] Notably, films deposited on 5×7 cm^2 glass substrates at 186 °C showed thickness non-uniformity. The thickness gradients were suggested to be caused by uneven delivery of O_3 to the substrate,[128] but the decomposition of O_3 on the cobalt oxide film surface is likely to contribute to the non-uniformity of the films as well.

For the $CoCp_2$ + O_3 ALD chemistry, four separate fundamental studies are found in the literature.[14,130–132] Cobalt oxide films deposited using $CoCp_2$ + O_3 are polycrystalline Co_3O_4 when deposited on Si and glass substrates, as verified with XRD, Raman spectroscopy and electron diffraction. Huang *et al*. used XPS to show that < 1 nm thick films contain cobalt as Co^{2+} and not Co^{3+}.[131] When the film thickness was increased to 6 nm and above, the deposition of Co^{3+} containing films, i.e. the Co_3O_4 phase was observed. Saturative film growth has been verified for both $CoCp_2$ and O_3 at temperatures of 167 °C and 250 °C.[130,132] In this temperature window, the GPC for this deposition chemistry is 0.4 – 0.5 Å.[130–132] According to Diskus *et al*., films deposited at 150 – 280 °C had uniform thickness, whereas at deposition temperatures of 137 °C and lower, an increase in thickness non-uniformity occurred along with decrease of GPC to approximately 0.2 Å.[130] Holden *et al*. also reported an increase in thickness non-uniformity when the deposition temperature was decreased from 175 to 150 °C, but conversely observed an increase in GPC from 0.5 to 0.8 Å.[14] The increase in GPC was assigned to the condensation of $CoCp_2$. This discrepancy between the two studies is most likely originating from differences in the vapor pressure of $CoCp_2$ as Diskus *et al*. evaporated $CoCp_2$ at room temperature, whereas Holden *et al*. used an evaporation temperature of 100 °C. In the study by Diskus *et al*., the thermal decomposition of $CoCp_2$ occurred at deposition temperatures over 331 °C.[130]

The $CoCp_2(CO)_2$ cobalt precursor has been used in combination with O_3 at deposition temperatures of 50 – 200 °C.[133] According to *in-situ* QCM measurements, film growth is self-limiting at 100 °C with a GPC of 1.1 Å. Above temperatures of 150 °C, $CoCp(CO)_2$ starts to decompose as evidenced by an increase in GPC to approximately 4.5 Å at 200 °C. Raman spectra of films deposited on glass at 50 – 150 °C were in agreement with spectra measured from a Co_3O_4 powder reference. However, according to Auger electron spectroscopy measurements, the oxygen to cobalt ratio in the films was 1.0, which implies the deposition of CoO films.

Another cobalt precursor with carbonyl ligands, hexacarbonyl(tert-butylacetylene)dicobalt, CCTBA, has also been used together with O_3 to deposit cobalt oxide films.[134] The limited thermal stability of CCTBA restricts the usability of this cobalt precursor to temperatures of 68 – 138 °C. According to *in-situ* QCM measurements, saturation with respect to CCTBA is obtained only at a single temperature of 68 °C. At temperatures of 80 – 138 °C, QCM did not show self-limiting mass increase during the cobalt precursor pulse, which indicates that CCTBA is decomposing. At 68 °C, i.e. under saturative film growth conditions, the GPC of this process was approximately 0.8 Å. Based on cross-sectional TEM images and electron diffraction patterns, films deposited at all temperatures were primarily of the Co_3O_4 phase but also contained small amounts of CoO. Auger electron spectroscopy (AES) experiments revealed that the oxygen to cobalt ratio in the films was close to 1.0, which also supports that the films contain both CoO and Co_3O_4. The step coverages of films deposited on aspect ratio 7.1 trenches at 80 and 138 °C were 100 % and 60 %, respectively.

The prototypical cobalt carbonyl compound $Co_2(CO)_8$ has been used in ALD together with O_3 at a single deposition temperature of 50 °C.[135] The authors declared that this process exhibits saturative growth behaviour, however, the reported GPC value was approximately 6.0 Å. A GPC this high denotes that over one monolayer is deposited during one deposition cycle. Based on characterization with XRD, the cobalt oxide films obtained using this chemistry were a mixture of CoO and Co_3O_4. According to XPS studies, the films contained cobalt as both Co^{2+} and Co^{3+}, which is in agreement with the deposition of Co_3O_4.

The $Co^{i\text{-}Pr}(DAD)_2 + O_3$ process has been used to deposit cobalt oxide films at temperatures of 120 – 300 °C.[126] Saturation studies done using *in-situ* QCM measurements at 150 °C confirmed that the film growth proceeds saturatively with respect to both precursors. The GPC value for this process was approximately 1.0 Å at 120 – 250 °C. When the deposition temperature was increased to 300 °C, a twofold increase in GPC was observed, which is indicative of decomposition of $Co^{i\text{-}Pr}(DAD)_2$. Electron diffraction patterns of films deposited at 150 – 250 °C corresponded to polycrystalline Co_3O_4 and also Raman spectra agreed with the presence of Co_3O_4. No indication of the CoO phase was given by either of the characterization methods. According to XPS measurements, the O:Co ratios of films deposited at 200 and 250 °C were 1.33, which corresponds to stoichiometric Co_3O_4.

The $Co(DMOCHCOCF_3)_2$ precursor has been used in combination with O_3 in a temperature range of 150 – 200 °C.[136] Saturation studies for this process were done at 200 °C. This deposition chemistry does not show normal saturation behaviour, as the GPC was noted to decrease from 0.2 Å to approximately 0.1 Å when the cobalt precursor pulse length was increased from 2.5 to 3.0 s. This behaviour was suggested to originate from etching of the deposited film by the cobalt precursor. The cobalt oxide films deposited at 200 °C were X-ray amorphous. According to XPS measurements, the as-deposited films contained both Co^{2+} and Co^{3+} and therefore, this precursor combination is suitable for depositing amorphous Co_3O_4 films. Annealing the as-deposited films in air at 800 °C for 3 h resulted in the formation of polycrystalline Co_3O_4 films.

4.1.3 Oxygen processes

Two examples of ALD chemistry for cobalt oxide film deposition with O_2 as the oxygen source are found in the literature. The scarcity of reports in this category is due to a lack of sufficiently reactive cobalt precursors. As O_2 is not as reactive as O_3, the cobalt precursors need to be either highly reactive or thermally stable at high temperatures. The $Co^{i\text{-}Pr}(DAD)_2 + O_2$ process is an example of the former option and the $CoI_2 + O_2$ process of the latter.

The $Co^{i\text{-}Pr}(DAD)_2 + O_2$ process has been used to deposit cobalt oxide films at temperatures of 125–300 °C.[125] The authors stated that no film growth occurred at 325 °C when O_2 was omitted from the pulsing sequence and concluded that $Co^{i\text{-}Pr}(DAD)_2$ is thermally stable up to this temperature. Saturation experiments were performed at 275 °C and the self-limiting growth mode was claimed to exist with respect to both precursors. However, the obtained GPC value of approximately 8.1 Å is unusually high and suggests that $Co^{i\text{-}Pr_2}(DAD)_2$ is decomposing. The crystalline phase of films deposited from $Co^{i\text{-}Pr_2}(DAD)_2 + O_2$ was reported to vary with respect to the deposition temperature. According to XRD and Raman spectroscopy studies, films deposited at 125–250 °C were a mixture of CoO and Co_3O_4, whereas films deposited at 265 °C and above were phase-pure, polycrystalline Co_3O_4. For films deposited at 275 °C, the O:Co stoichiometry was determined using RBS and stoichiometry of 1.3 corresponding to Co_3O_4 was obtained.

The $CoI_2 + O_2$ process is an example of high-temperature metal oxide ALD chemistry.[137] Due to the low vapor pressure of CoI_2, an unusually high source temperature of 465 °C is needed for this precursor. Saturative growth mode with respect to both CoI_2 and O_2 was confirmed at a deposition temperature of 525 °C. At 475 – 600 °C, GPC on Si substrates was approximately 1.5–2.0 Å and on MgO approximately 0.8 – 1.0 Å. Films deposited on Si were polycrystalline, phase-pure Co_3O_4 whereas on the MgO substrates, registry between the deposited Co_3O_4 films and the underlying substrate was observed. At 700 °C, GPC decreased close to 0 Å, which suggests that CoI_2 cannot adsorb on the growth surface at this temperature. Co_3O_4 films deposited at 575 °C were shown to have an O:Co stoichiometry of 1:33 and to be free of iodine impurities, as analyzed with X-ray fluorescence (XRF), RBS and ToF-ERDA.

4.1.4 Electrical and optical properties of ALD cobalt oxide films

Resistivities of ALD Co_3O_4 thin films have been reported for those deposited from $CoCp_2$ + O_3 [14] and $Co(thd)_2$ + O_3.[128,129] For polycrystalline Co_3O_4 films on Si and glass substrates, resistivities were in the range 0.1 – 80 Ω cm depending on film thickness. Generally, films deposited at high deposition temperatures were found to have higher resistivity than films obtained at lower deposition temperatures.[128,129] The increased resistivity in the films deposited at high temperatures may be due to impurities in the form of CoO or carbon originating to partial decomposition of $Co(thd)_2$.

Band gap analysis of Co_3O_4 films has been presented by Holden *et al*.,[14] who reported energy gap widths of approximately 2.2 eV for films deposited at temperatures of 150 – 350 °C. The band gap analysis was done using the Tauc plot method and assuming for direct allowed transitions.

4.1.5 Applications of ALD cobalt oxide films

An interesting and attractive property of cobalt oxides is their electrocatalytic activity in the water oxidation reaction.[138] Ngo *et al*. applied the $Co(^{i-Pr}amd)_2$ + H_2O ALD chemistry for creating CoO/TiO_2 and $CoO/SrTiO_3$ photoanodes suitable for visible light driven photo-electrochemical water splitting.[121] In these structures, the top CoO layer acts as an electrocatalyst for the oxygen evolution reaction on the photoanode surface. Using these photoanode structures, photoelectrochemical water oxidation was demonstrated with visible light (λ > 420 nm) illumination. This result is remarkable, as water splitting with pristine TiO_2 and $SrTiO_3$ photoanodes requires UV illumination.

The electrocatalytic properties of cobalt oxide films in water splitting were also studied by Oh *et al*., who used the $Co^{i-Pr}(DAD)_2$ + O_2 deposition chemistry for creating n-Si/CoO_x photoanode structures.[139] The best photoelectrochemical performance was achieved with photoanodes that were a mixture of the CoO and Co_3O_4 phases. With these photoanode structures, appreciably high photocurrents of approximately 30 mA cm^{-2} were obtained under illumination from a 1.5 AM Sun simulator.

Another topic of emerging interest related to cobalt oxide films is metallization via post-deposition reduction.[5,122] Väyrynen *et al*. showed that CoO films can be reduced to metallic Co by 45 minute annealing in 10 % forming gas at 250 °C.[5] The method for obtaining metallic Co from CoO reported by Zhang was based on reduction with atomic deuterium at 220 °C and capping the Co film with an oxygen scavenging Al layer.[122]

4.2 Copper oxides

A total of 11 copper precursors have been used in copper oxide film deposition. The molecular structures of these precursors are shown in Figure 7.

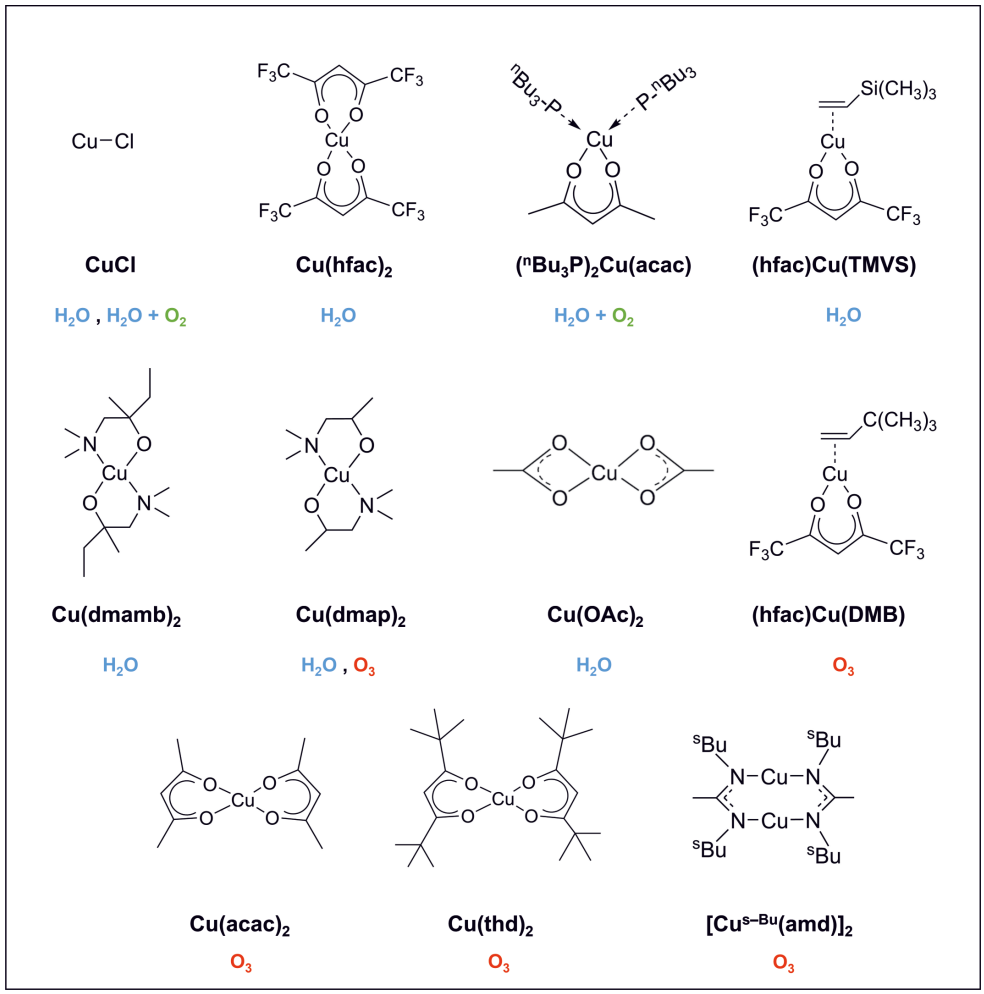

Figure 7. Chemical structures of precursors utilized in ALD of copper oxide thin films. The oxygen source(s) used with each precursor have been listed below the name of the molecule.

4.2.1 Water processes

Seven of the precursors shown in Figure 7 have been used with H_2O for depositing copper oxide films. The main process parameters of these ALD processes are listed in Table 3. The ALD processes utilizing "wet oxygen", i.e. the combination of H_2O and O_2 are also discussed here.

Table 3. Characteristics of ALD copper oxide processes based on using H_2O and wet oxygen as the oxygen source. a) For the CuCl + H_2O –process, b) for the CuCl + H_2O + O_2 –process, c) for the CuCl + H_2O –process with I_2 added to the H_2O vessel, d) on Ru substrates, e) GPC and saturation are not applicable for Spatial ALD.

Precursor	Deposition temperature (°C)	GPC (Å)	Saturation	Phase of the deposited films	Ref.
CuCl	350 – 700	0.1 – 1.5 [a)] 2.0 – 2.2 [b)]	yes [b)] / no [a)]	Cu + Cu_2O,[a)] Cu_2O,[c)] CuO [b)]	107,140
$(^nBu_3P)_2Cu(acac)$	100 – 135	0.05 – 0.1	no	Cu_2O, Cu_2O + CuO [d)]	108
$Cu(hfac)_2$	210 – 302	0.4	no	Cu_2O	140,141
$Cu(dmamb)_2$	120 – 240	0.13 – 1.5	yes	Cu_2O	142
$Cu(dmap)_2$	110 – 200	0.12	yes	Cu_2O	143
(hfac)Cu(TMVS)	150 – 350	1 nm / min [e)]	N/A [e)]	Cu_2O, Cu + Cu_2O	49
$Cu(OAc)_2$	180 – 240	0.11 – 0.13	yes	Cu_2O, Cu + Cu_2O	**IV**

The CuCl + H_2O ALD chemistry can be used to deposit Cu_2O films at 350 – 700 °C.[140] This precursor combination is applicable only at high temperatures due to the low vapor pressure of CuCl. According to the deposition experiments at 400 °C, film growth is not saturative due to the thermal instability of CuCl. The thermal instability of CuCl was also noted to result in metallic copper impurities in the films. Interestingly, the addition of I_2 to the H_2O pulse was noted to prevent the formation of metallic Cu in the films. A probable mechanism of the mechanism for the removal of metallic Cu is its oxidation to CuI by I_2. From here on, CuI can either evaporate from the surface or reach with H_2O to form Cu_2O and HI. The Cu_2O films deposited on Si were polycrystalline, whereas deposition on α-Al_2O_3 substrates resulted in the formation of Cu_2O films with a (110) preferred orientation. Cu_2O films deposited from CuCl + H_2O were reported to have thickness gradients along the direction of precursor flow. A likely explanation for the thickness non-uniformity is that the films are etched by HCl which is forming as a by-product in the film-forming surface reactions.

In another ALD study utilizing CuCl, this copper precursor was used in combination with "wet oxygen".[107] In this ALD chemistry, H_2O is used to the remove the Cl ligands and O_2 to oxidize Cu^+ to Cu^{2+}. The deposition experiments were done at a single temperature of 410 °C on MgO substrates. Saturative growth was verified to occur with respect to both precursors with a GPC of approximately 2.0 Å. According to XRD analysis, the deposited films were of the CuO phase with a preferred (111) orientation. This verifies that O_2 can oxidize Cu^+ to Cu^{2+} at the deposition temperature used for this study.

"Wet oxygen" has also been used together with the heteroleptic $[(^nBu_3)P]_2Cu(acac)$ copper precursor.[108] In this study, film deposition experiments were done on SiO_2, Ta, TaN and Ru substrates. Saturation experiments with respect to the copper precursor were performed at 135 °C on TaN, but no presence of self-limiting growth was observed. Temperature-independent growth with GPC of approximately 0.1 Å was reported up to 120 ºC on the metallic Ta, TaN and Ru substrates, while on SiO_2 the GPC values were below 0.05 Å at 100 – 130 ºC. Films deposited on all substrates were primarily of the Cu_2O phase, as characterized with XPS and electron diffraction. Films deposited on Ru substrates were noted to contain both Cu_2O and CuO. The partial oxidation of the films was suggested to be due to the catalytic dissociation of O_2 on the Ru substrate. Angle-resolved XPS studies showed that the surfaces of the Cu_2O films deposited on all substrates contained copper as Cu^{2+}, which was assigned to the formation of $Cu(OH)_2$ and CuO species by post-deposition oxidation in air.

The fluorinated β-diketonate copper precursor, $Cu(hfac)_2$ has been used together with H_2O to deposit Cu_2O films at temperatures of 210 – 302 °C.[141] The main topic of this study was to deposit metallic copper / copper nitride in an ABC type deposition scheme, where A is $Cu(hfac)_2$, B is H_2O and C is NH_3. However, the properties of the oxide deposition process were also discussed to a minor extent. According to the saturation experiments at 247 °C, the $Cu(hfac)_2 + H_2O$ process showed self-limiting growth with respect to H_2O but not to the copper precursor. It was noted that no thermal decomposition of $Cu(hfac)_2$ occurred at this temperature. Notably, protonated hfac ligands (Hhfac) can etch copper oxide,[144] which may explain the lack of saturation for this deposition chemistry. According to XRD, films deposited from $Cu(hfac)_2 + H_2O$ on SiO_2 at 247 °C were polycrystalline Cu_2O.[141] This finding is interesting, as the oxidation state of copper in $Cu(hfac)_2$ is +2 which implies that copper is reduced during the deposition process. However, no discussion on a possible redox mechanism was included. According to XPS measurements, copper exists in the films as Cu^+ and the carbon and fluorine contents in the films were ≤ 1.0 at-%.

$Cu(dmamb)_2$ is an aminoalkoxide copper(II) precursor that has been used together with H_2O to deposit Cu_2O films at temperatures of 120 – 240 °C.[142] The authors reported that no thermal decomposition of this copper precursor occurred at up to a temperature of 240 °C. Saturation experiments at 140 °C showed that the film growth is self-limiting with GPC of approximately 0.13 Å. Increasing the deposition temperature to 160 – 240 °C resulted in an increase of GPC to 0.45 – 1.5 Å, which indicates that $Cu(dmamb)_2$ is decomposing at these temperatures. Based on XRD and electron diffraction, the films deposited in the studied temperature range were phase-pure polycrystalline Cu_2O. Based on RBS measurements, the oxygen to copper ratio in the films was approximately 1.1:2 and the amounts of C and N impurities were < 0.2 at-%. Furthermore, Cu_2O films deposited from $Cu(dmamb)_2 + H_2O$ at 140 °C on 1.1 μm long, ordered Si nanowires with an aspect ratio of 7.6 were reported to be 100 % conformal.[145]

$Cu(dmap)_2$ is another aminoalkoxide copper precursor that has been used together with H_2O to deposit copper oxide thin films.[143] Film deposition experiments in this study were done at temperatures of 110 – 200 °C and process characterization was done using *in-situ* QCM

measurements. According to QCM data collected at 150 °C, no mass increase occurred when H_2O was omitted from the precursor pulsing sequence. This result was interpreted to signify that $Cu(dmap)_2$ is thermally stable at 150 °C. However, this deposition chemistry showed non-saturative growth characteristics, as increasing the copper precursor pulse time from 0.2 to 1.0 s resulted in a decrease in GPC from approximately 0.15 to 0.1 Å. The film characterization was done using ultra thin, 5 nm samples. According to XRD, the films deposited at 150 °C were amorphous. Based on XPS, the films contain copper as Cu^+. These results were used to conclude that this deposition process produces Cu_2O. The authors pointed out that it is possible for protonated dmap ligands to reduce Cu^{2+},[146,147] which can explain why Cu_2O films are obtained from a Cu(II) precursor instead of CuO.

Deposition of copper oxide thin films has also been demonstrated using spatial atmospheric pressure ALD.[49] The copper precursor in this study was (hfac)Cu(TMVS) (CupraSelect™) and film deposition experiments were carried out at temperatures of 150 – 350 °C. The growth rate of copper oxide films reported in this study was very high, approximately 1 nm min^{-1}. Notably, this deposition rate is two orders of magnitude higher than what is achieved in traditional thermal ALD. According to film characterization with XRD and electron diffraction, the (hfac)Cu(TMVS) + H_2O spatial ALD process produces phase-pure, polycrystalline Cu_2O films at 150 – 300 °C and films that are a mixture of Cu_2O and CuO at 350 °C. Notably, (hfac)Cu(TMVS) has also been used to deposit pure metallic Cu films with CVD at 75 – 420 °C.[148] This would imply that (hfac)Cu(TMVS) is decomposing during the spatial ALD copper oxide deposition process described in Ref. (49).

4.2.2 Ozone processes

Five precursors have been used together with O_3 in ALD of copper oxide thin films. The main process parameters for these ALD chemistries are summarized in Table 4.

Table 4. Characteristics of ALD copper oxide processes based on using O_3 as the oxygen source.

Precursor	Deposition temperature (°C)	GPC (Å)	Saturation	Phase of the deposited films	Ref.
(hfac)Cu(DMB)	100	0.31	yes	Cu_2O + CuO	68
$Cu(acac)_2$	150 – 240	0.38	no	CuO	53
$Cu(thd)_2$	200 – 260	0.15	no	CuO + Cu_2O	54
$[Cu^{s\text{–}Bu}(amd)]_2$	250	0.45 – 0.7	N.R.	CuO	149
$Cu(dmap)_2$	80 – 140	0.2 – 0.3	yes	CuO	**I**

(hfac)Cu(DMB) is a copper(I) precursor that has been used in combination with O_3 at a single deposition temperature of 100 °C.[68] Saturative growth was reported to occur with respect to both precursors with a GPC of 0.31 Å. The as-deposited films were X-ray amorphous. Based on XPS measurements and interpretation of Auger electron spectra, the

authors suggested that the as-deposited films contained copper as Cu^{2+}, Cu^{+} and Cu^{0}. This result is surprising, as O_3 can oxidize both Cu^{+} and Cu^{0} to Cu^{2+} due to its high oxidation potential.[109] However, β-diketonates are known to promote disproportionation chemistry of copper(I) and the multiple oxidation states of copper in the films may be a consequence of this redox chemistry.[150] According to XRD and optical measurements, the as-deposited films and films subjected to post-deposition rapid thermal annealing (RTA) in air at 200 °C were Cu_2O, whereas films treated with RTA in air at 400 °C crystallized in the monoclinic CuO structure.[68]

Properties of the $Cu(acac)_2 + O_3$ ALD chemistry have been studied at temperatures of 150 – 240 °C.[53] Deposition experiments done at 200 °C showed that the film growth is not saturative with respect to $Cu(acac)_2$. The authors also stated that films deposited at the highest deposition temperature studied, 240 °C, were non-uniform due to the decomposition of $Cu(acac)_2$. Films deposited at 160 – 240 °C were polycrystalline CuO, albeit with a low degree of crystallinity. According to XPS, the prevailing oxidation state of copper in films deposited at all temperatures was +2, which confirms the deposition of CuO.

The $Cu(thd)_2 + O_3$ precursor combination has been studied at deposition temperatures of 200 – 260 °C.[54] Saturation studies done at 240 °C. Self-limiting growth behaviour occurred for $Cu(thd)_2$ but curiously, not with respect to O_3. The authors ascribed this behaviour to precursor decomposition. Based on XRD measurements, the films deposited from $Cu(thd)_2 + O_3$ were weakly crystalline CuO similarly to the films deposited from $Cu(acac)_2 + O_3$.[53] It was also noted that occasional traces of Cu_2O impurity phases were present in the films.[54] Post-deposition RTA in a dynamic O_2 atmosphere at 400 °C resulted in the formation of CuO films with an increased degree of crystallinity.

$[Cu^{s\text{-}Bu}(amd)]_2$ is a dimeric copper amidinate compound that has been used together with O_3 at a single deposition temperature of 250 °C.[149] No saturation studies exist for this precursor combination, but the GPC of this process was reported to be 0.45 – 0.6 Å depending on the copper precursor pulse length. The obtained films where characterized with XRD, Raman spectroscopy and XPS. Based on XRD and Raman measurements, films deposited on Si and FTO substrates were polycrystalline CuO. XPS measurements showed that the oxidation state of Cu in the films was +2. Deconvolution of O 1s photoelectron spectra indicated that the films also contained copper carbonate and copper hydroxide, which may indicate that $[Cu^{s\text{-}Bu}(amd)]_2$ undergoes partial thermal decomposition at 250 °C.

4.2.3 Electrical and optical properties of ALD copper oxide films

Similarly to the ALD cobalt oxide films, the electrical and optical properties of ALD copper oxide films are of interest. CuO films have been primarily characterized with respect to electrical resistivity and band gap. Cu_2O films have also been characterized optically, but also with Hall measurements which yield information on electrical and semiconductor properties such as charge carrier type, mobility and concentration.

The electrical resistivities of CuO films deposited from $Cu(acac)_2$ and O_3 were reported to vary with deposition temperature.[53] The resistivity of 40 nm thick CuO films deposited at 150 °C was in the order of 10^0 Ω cm, while increasing the deposition temperature to 240 °C resulted in films with a specific resistivity of 10^3 Ω cm. A possible explanation for the increase in resistivity is the increased carbon impurity content in the films deposited at high temperatures. CuO films deposited from $Cu(thd)_2 + O_3$ were also noted to exhibit similar electrical properties.[54] The resistivity of the as-deposited, 20 – 80 nm thick films was approximately 20 – 50 Ω cm, whereas RTA for 5 minutes at 400 °C in a dynamic O_2 atmosphere resulted in films with resistivity values close to 1 Ω cm.

The authors of the $Cu(thd)_2 + O_3$ chemistry also studied the optical properties of their CuO films.[54] The experiments were done utilizing the Tauc plot method and the analysis was done assuming for indirect allowed transitions. The band gap values reported for CuO thin films varied depending on the sample thickness; 9 nm thick films had a narrow band gap of 1.06 eV whereas the band gap values of thicker films were increasing monotonously with increasing thickness. For an 81 nm CuO film, a band gap of 1.24 eV was reported.

Band gap studies of copper oxide films were also carried out by the authors of the single deposition temperature (50 °C) (hfac)Cu(DMB) + O_3 process.[68] However, they did not specify whether the analyses were done with respect to a direct or an indirect band gap. The band gaps of as-deposited films and films subjected to RTA in air at 200 °C were close to 2.1 eV, which indicates the formation of the Cu_2O phase. Increasing the RTA temperature to 300 – 500 °C resulted in films with band gap values of approximately 1.4 – 1.5 eV, which are characteristic for CuO.

Electrical properties of the Cu_2O films deposited using the (hfac)Cu(TMVS) +H_2O spatial ALD process were studied with Hall measurements.[49] The Hall mobilities of 50 – 120 nm thick films were approximately of 0.5 – 5 $cm^2\ V^{-1}\ s^{-1}$. The charge carrier concentration in films deposited at all temperatures were constant at approximately 10^{16} cm^{-3}, while the resistivies of the films decreased with increasing deposition temperature. The resistivities of films deposited at 225 °C was approximately 120 Ω cm. For films deposited with the $Cu(dmamb)_2 + H_2O$ chemistry at 140 °C, Hall mobility values of 8.1 $cm^2\ V^{-1}s^{-1}$ were reported.[142]

The authors of the (hfac)Cu(TMVS) + H_2O and $Cu(dmamb)_2 + H_2O$ ALD processes also studied the optical properties of their Cu_2O films.[49,142] These analyses were done utilizing the Tauc plot method and assuming for direct allowed transitions. Both studies reported that the direct allowed band gap of the Cu_2O films is 2.5 eV.

4.2.4 Applications of ALD copper oxide films

Cu_2O films deposited with the $Cu(dmamb)_2$ + H_2O process have been used for making photodiodes on n-Si substrates.[145] Two different device structures were used, planar Si and Si nanowires with an aspect ratio of approximately 7.6. The Cu_2O films deposited on the nanowire structure were reported to be 100 % conformal and thus, this approach was demonstrated to be suitable for creating an n-Si/p-Cu_2O core-shell photodiode array. Compared to reference planar devices, the core-shell nanowire devices exhibited improved photodetection performance under UV illumination and enhanced photocurrent in the forward bias region. The improved performance of the core-shell nanowire structure was assigned to increased light absorption and effective separation of photogenerated charges at the pn-interface.

The (hfac)Cu(DMB) + O_3 process was used to make bottom-gate thin film transistor (TFT) structures.[68] In these devices, p^+–Si was used as the gate metal and a 100 nm thick SiO_2 layer as the gate dielectric. The thickness of the copper oxide channel layer was not reported. The Cu_2O channel layer was subjected to RTA in air at temperatures of 200 – 500 °C. The TFT devices made from as-deposited, amorphous Cu_2O layers were measured to have a field effect mobility of 1.7 $cm^2\ V^{-1}\ s^{-1}$ and an on/off ratio in the order of 10^3. Improvement in device performance was obtained by oxidizing the copper oxide channel layer to CuO with RTA in air at 300 °C. The field effect mobility of the devices with the annealed CuO layer was 5.6 $cm^2\ V^{-1}\ s^{-1}$ and the on/off ratio was approximately 10^5.

4.3 Ternary, quaternary and other complex cobalt oxides and copper oxides

Similarly to their binary counterparts CoO, Co_3O_4, Cu_2O and CuO, thin films of ternary, quaternary and doped cobalt or copper containing oxides hold potential to be utilized in various electronic, optical and catalytic applications. In ALD, ternary, quaternary and other complex thin films can be synthesized by combining two or more deposition processes for the corresponding binaries.[82,151] The stoichiometry of the films can be adjusted by controlling the pulsing ratio of the different metal precursors. Most of the ternary, quaternary and other complex metal oxide films have been deposited from metal β-diketonates and O_3 due to the thermal compatibility of these ALD chemistries.[151] In most instances, the ternary and quaternary metal oxide thin films are amorphous as-deposited but can be crystallized by annealing at elevated temperatures. The ALD processes for cobalt-containing complex oxide thin films are listed in Table 5 and the ALD processes for copper-containing oxide films are listed in Table 6.

Table 5. ALD processes for cobalt-containing complex oxide thin films. [a)] DEZ = diethylzinc.

Material	Metal precursors	Oxygen source	Deposition temperature (°C)	Crystallization requirement	Ref.
$[CoCa_2O_3]_xCoO_2$	$Ca(thd)_2$ $Co(thd)_2$	O_3	200 – 300	RTA under O_2 and N_2 at 550 – 850 °C	40
$MnCo_2O_4$	$Mn(thd)_2$ $Co(thd)_3$	O_3	135 – 275	Crystalline as-dep.	152
$CoFe_2O_4$	$FeCp_2$ $CoCp_2$	O_2	450	Crystalline as-dep.	153
$CoFe_2O_4$	$FeCp_2$ $CoCp_2$	O_3	250	Crystalline as-dep.	154
Fe_2CoO_4 $(FeCo)_{1.5}O_4$	$Fe(thd)_3$ $Co(thd)_2$	O_3	185 – 235	Anneal under O_2 at 600 or 800 °C	155
$NiCo_2O_4$	$Ni(thd)_2$ $Co(thd)_2$	O_3	200	Crystalline as-dep.	35
$SrCoO_3$	$Co(thd)_3$ $Sr(thd)_2$	O_3	290 – 330	RTA under O_2 or N_2 at 600 – 800 °C	156
$LaCoO_3$	$Co(thd)_3$ $La(thd)_3$	O_3	200 – 400	Anneal in air at 600 °C	127
$(Sr,La)CoO_3$	$Co(thd)_3$ $Sr(thd)_2$ $La(thd)_3$	O_3	290 – 340	RTA under O_2 or N_2 at 500 – 1000 °C	157
ZnO:Co	DEZ[a)] $Co(acac)_3$	H_2O	160	Crystalline ZnO as-dep.	158
TiO_2:Co	$Ti(OMe)_3$ $Co(acac)_3$	H_2O, O_3	300	Crystalline TiO_2 as-dep.	159
Co_3O_4:ZrO_2 nanolaminate	$Co(acac)_3$ $ZrCl_4$	O_3	300	Crystalline-as dep.	21,160

Table 6. ALD processes for copper-containing complex oxide thin films.

Material	Metal precursors	Oxygen source	Deposition temperature (°C)	Crystallization requirement	Ref.
$CuCrO_2$	$Cr(acac)_3$ $Cu(thd)_2$	O_3	240 – 270	RTA in Ar at 700 – 950 °C	72
$CuCr_2O_4$	$Cr(acac)_3$ $Cu(thd)_2$	O_3	250	RTA under O_2 at 700 °C	161
$CuCrO_2$:Mg	$Mg(thd)_2$ $Cr(acac)_3$ $Cu(thd)_2$	O_3	250	RTA in Ar at 800 °C	73
$LaCuO_3$ La_2CuO_4	$Cu(acac)_2$ $La(thd)_3$	O_3	210 – 300	Anneal under O_2 at 650 – 900 °C	162
$(Sr,La)CuO_4$	$Cu(acac)_2$ $Sr(thd)_2$ $La(thd)_3$	O_3	250	Anneal in air at 650 °C	77
$CuWO_4$	$[Cu^{s-Bu}(amd)]_2$ $(^tBuN)_2W(Me_2N)_2$	O_3 H_2O	250	Anneal in air at 600 °C	149
ZnO:Cu	DEZ $Cu(hfac)_2$	H_2O	200	Crystalline ZnO as-dep.	163

Of the ternary, quaternary and other cobalt-containing compounds listed in Table 5, $MnCo_2O_4$, $CoFe_2O_4$, $(CoFe)_{1.5}O_4$, $NiCo_2O_4$ and cobalt-doped TiO_2 exhibit ferri- or ferro-magnetism. Consequently, thin films of these materials have been studied and characterized with respect to coercivity and magnetic saturation.[35,152,154,155,159] The motivation for depositing magnetic thin films with ALD is the utilization of these materials in magnetic storage devices based on 3D architectures. Another approach for creating magnetic thin films is the deposition of nanolaminates, such as ZrO_2:Co_3O_4.[21,160]

From the copper-containing oxides listed in Table 6, $CuCrO_2$ and the Mg-doped copper chromium delafossite, $CuCrO_2$:Mg are of p-type TCOs.[35,72,73,161] The electrical properties and the width of the band gap of copper chromium oxides can be adjusted by controlling the cation stoichiometry. As an example, the resistivity of $CuCrO_2$ thin films crystallized with rapid thermal annealing in Ar is in the the order of 10^0 Ω cm,[72] whereas the resistivity of $CuCr_2O_4$ is two orders of magnitude greater, in the range of 10^2 Ω cm.[161] By doping $CuCrO_2$ with Mg, electrical resistivity as low as 10^{-3} Ω cm can be achieved.[73] Due to a band gap of 3.1 eV of $CuCrO_2$:Mg an appreciably transmittance in the visible wavelength range, approximately 80 %, can be obtained.[73]

Recently, the deposition of $La_{2-x}Sr_xCuO_{4-y}$ thin films with ALD has been demonstrated by Sønsteby *et al*.[77] In this study, highly oriented thin films of the superconductive cuprate were deposited from metal β–diketonate precursors and O_3 on pseudocubic $LaAlO_3$ substrates. The as-deposited films were amorphous but crystallized in the superconductive Ruddlesden-Popper 1 phase upon annealing in air at 650 °C. The authors demonstrated that

the cation stoichiometry of the deposited films could be accurately controlled by adjusting the metal precursor pulsing sequence. The lowest sheet resistance for the approximately 40 nm thick films was obtained with a Sr cation content of 5 – 6 %. Temperature dependent electrical measurements of the films showed a drastic decrease in sheet resistance at temperatures below 20 K. The resistivity did not, however, reach zero as expected for a superconducting material. The remaining resistivity in the films was assigned to originate grain boundaries present in the samples.

Ternary oxide films can also be made by depositing two discrete binary material layers and annealing the stack to form a homogeneous film. This approach, the so stack deposition-annealing (SDA) method, has been used for creating $CuWO_4$ thin film photoanodes.[149] As a material, $CuWO_4$ exhibits n-type conductivity and has a band gap suitable for visible light absorption, approximately 2.3 eV. The synthesis of $CuWO_4$ thin films was realized by depositing a WO_3 bottom layer from $(^tBuN)_2W(Me_2N)_2 + H_2O$ and by depositing a top CuO layer using the $[Cu^{s-Bu}(amd)]_2 + O_3$ process. A homogeneous, polycrystalline $CuWO_4$ film was obtained after annealing in air at 600 °C for 30 minutes. Stability testing under electrochemical conditions (1.23 V vs. RHE, pH 9, 1 sun illumination) showed that $CuWO_4$ photoanodes made with the SDA approach were stable up to 4 hours, whereas the performance of reference WO_3 thin film photoanodes degraded after 1 hour of operation.

5 Experimental

5.1 Film deposition

All film deposition experiments performed during this dissertation work were done using the commercial F-120 ALD reactor (ASM Microchemistry Ltd.) operated in the cross-flow configuration.[164] Nitrogen (99.999%, $O_2 \leq 3$ ppm, $H_2O \leq 3$ ppm) was used as a carrier and purging gas at a flow rate of 400 sccm. The pressure of the ALD reactor during the film deposition experiments was approximately 10 mbar.

Deposition experiments for process optimization and film characterization were done on 5×5 cm^2 squares of soda lime glass (SLG) and native oxide terminated Si (100) substrates (Okmetic Oy). Thin film samples for photoelectrochemical characterization were deposited on fluorine doped tin(IV) oxide (SnO_2:F, FTO) coated glass substrates (Solems TEC7, 6 – 8 Ω/sq). Prior to film deposition, the SLG and FTO substrates were cleaned with ultrasonication in successive baths of alkaline detergent, absolute ethanol and deionized water, whereas the Si substrates were used as received. Before loading any substrates to the ALD reactor, they were blown clean of particles using pressurized N_2.

All the cobalt and copper precursors used for film deposition are solids. The precursors were evaporated inside the ALD reactor from an open glass vessel. Deionized water or a mixture of O_2/O_3 were used as the oxygen sources. Water vapor was introduced to the ALD reactor through a needle valve using vacuum draw. O_3 was generated from O_2 gas (99.999%) using a Wedeco Ozomatic 4 HC ozone generator. The resulting O_2/O_3 mixture, with an O_3 concentration of approximately 100 g / N m^3 was led to the ALD reactor through needle and solenoid valves. The flow rate of the O_2/O_3 gas mixture was adjusted to approximately 200 sccm using the needle valve.

5.2 In situ reaction mechanism studies

The reaction mechanism studies were done using a modified F-120 ALD reactor (ASM Microchemistry Ltd.) consisting of a Hiden HAL/3F 501 QMS equipped with a Faraday cup detector and a Maxtek TM 400 QCM. A full description of the ALD reactor modified for the reaction mechanism studies has been published elsewhere.[105] In short, the reactor consists of two chambers, the deposition chamber and the QMS chamber. The deposition chamber holds the QCM and a set of large SLG substrates. The SLG substrates increase the surface area of the deposition chamber which helps to obtain a sufficient amount of reaction by-products for the QMS analyzer. The deposition chamber is connected to the QMS chamber via a 100 μm diameter orifice. The pressure of the deposition chamber is approximately 10 mbar while the pressure in the QMS chamber is in the order of 10^{-5} mbar. The pressure difference is achieved by differential pumping through the orifice by using a turbomolecular pump. Nitrogen (99.999% $O_2 \leq 3$ ppm, $H_2O \leq 3$ ppm) was used as a carrier

and purging gas. In the reaction mechanism studies, deuterium oxide, D_2O (99.96% D, Eurisotop) was used instead of H_2O to distinguish the by-products of ligand exchange reations from ligand fragments that form upon ionization in the QMS. The formalism for the analysis of QMS and QCM data is based on the work of Rahtu and Knapas.[98,105]

5.3 Film characterization

Film characterization with respect to crystallinity was conducted using a PANalytical X'Pert Pro MPD X-ray diffractometer or a Rigaku SmartLab X-ray diffractometer. Both instruments were equipped with a Cu Kα X-ray source (λ = 1.54 Å). All of the XRD measurements were performed in the grazing incidence geometry using an incidence angle of 1°. High temperature XRD measurements were done using an Anton-Paar HTK 1200N oven connected to the PANalytical X'Pert Pro MPD instrument.

Thicknesses of the films were measured using either X-ray reflectivity (XRR), UV-Vis spectrophotometry, ellipsometry or energy dispersive X-ray spectroscopy (EDX). The XRR measurements were done with the PANalytical X'Pert Pro MPD X-ray diffractometer. Film thickness was modeled from the XRR data using the X'Pert Reflectivity 1.2a software (PANalytical). UV-Vis measurements were done using a Hitachi U-2000 spectrophotometer at a wavelength range of 190–1100 nm. The UV-Vis spectrophotometer was operated in the reflectance geometry. The data obtained from the UV-Vis measurements was modeled using the ThinFilm software.[165] Ellipsometric measurements were done using the FilmSense FS-1 multi-wavelength instrument. Film thickness was modeled from the measurement data using the Cauchy formalism. The EDX spectra were collected using a system consisting of a Hitachi S-4800 field emission scanning electron microscope (FESEM) and an Oxford INCA 350 microanalysis instrument. Film thickness was calculated from the EDX spectra using the GMRfilm software.[166] In case of metal oxide thin films, the error in film thickness measured with this method is less than 10 %. The analyses were carried out assuming for bulk density for the material in question.

Film morphology was studied using FESEM and atomic force microscopy (AFM). The FESEM analyses were done using the Hitachi S-4800 instrument. AFM images were collected using a Veeco Multimode V atomic force microscope equipped with a Nanoscope V controller. The AFM surface analysis was done in the intermittent contact mode (tapping mode) in air using Si probes with a nominal tip radius of 8 nm (Bruker). In order to remove artifacts caused by sample tilt and scanner bow, the AFM images were either flattened or plane-fitted using the Nanoscope 1.6 software package (Bruker). The surface roughness of the thin film samples was calculated as average root-mean-square (R_q) values from either 0.5×0.5 μm^2 or 2.0×2.0 μm^2 images using the Nanoscope 1.6 software.

X-ray photoelectron spectroscopy (XPS) studies were done in a UHV system consisting of an Omicron DAR 400 X-ray source (1253.6 eV Mg Kα line) and an Omicron ARGUS spectrometer equipped with a multichannel plate detector. The spectrometer was operated

at a pass energy of 20 eV. The binding energies of the photoelectron spectra were calibrated using the C 1s peak of ambient hydrocarbons at 284.8 eV. No sputtering was done for any of the thin film samples. Analysis of the photoelectron spectra was done using the CasaXPS software package (www.casaxps.com). Deconvolution of the photoelectron spectra was done according to peak fitting parameters for Co and Cu refined by Biesinger *et al*.[167–169] Time-of-Flight elastic recoil detection analysis was done using the 5 MV EGP–10–II tandem accelerator at University of Helsinki, Finland. The setup used for the ion beam measurements has been described in full elsewhere.[170]

Optical properties of films deposited on SLG substrates were studied by UV-Vis spectrophotometry. The measurements were done using the Hitachi U-2000 spectrophotometer at a wavelength range of 190–1100 nm and the Shimadzu UV-2600 instrument in a wavelength range of 200–800 nm. The determination of band gaps was done using the Tauc plot formalism.[171]

Photoelectrochemical measurements were done in a standard electrochemical cell consisting of a Pt counter electrode and an Ag/AgCl (3 M KCl) reference electrode. ALD thin films deposited on FTO substrates were used as the working electrode. The electrochemical cell was controlled using a SP-300 BioLogic potentiostat. Wavelength-resolved photocurrent measurements were done using a system consisting of a 150 W xenon lamp and a grating monochromator with a nominal bandwidth of 10 nm. The working electrodes were irradiated from the back side, through the glass substrate. Oxygen evolution experiments were conducted in a two-compartment cell connected to an OxySense 325i oxygen analyzer. 0.1 M borate buffer (pH 9.2) was used as the electrolyte solution. Prior to the oxygen evolution experiments, the electrolyte solution was purged with argon gas for 30 min to remove dissolved oxygen. The working electrode was illuminated with a 150 W xenon lamp equipped with a KG-3 heat-absorbing filter (Schott) and a 1.5 AM filter.

Photoconductivity measurements were carried out using a setup consisting of a Keithley 2450 source meter and laser diodes emitting at 405, 450, 523, 635, 780 and 980 nm (Thorlabs). The incident light power density was controlled using neutral density filters.

6 Results and discussion

This chapter reviews the central results of this dissertation work. Included is a summary of four ALD process development studies, as well as characterization of functional properties of cobalt oxide and copper oxide thin films. A more detailed analysis of the results can be found in references. [I – IV]

6.1 ALD of cobalt oxide thin films

In the course of this work, two new ALD processes were developed for depositing cobalt oxide thin films, the $Co(BTSA)_2(THF) + H_2O$ process [III] and the $Co^{t\text{-}Bu}(DAD)_2 + O_3$ process.[II]

6.1.1. $Co(BTSA)_2(THF) + H_2O$ [III]

$Co(BTSA)_2(THF)_2$ is a metal silylamide compound that can be obtained through a simple synthetic procedure comprising of a metathesis reaction between $CoCl_2$ and Li(BTSA). If the synthesis is done in tetrahydrofuran (THF), $Co(BTSA)_2(THF)$ is obtained, whereas using diethyl ether (Et_2O) as the solvent yields the dimeric $[Co(BTSA)_2]_2$.[172]

According to TGA measurements performed under a dynamic N_2 atmosphere (1 atm), both variants of this cobalt precursor evaporate in a single step and leave a minimal residue of approximately 3 – 4 m-% (Figure 8). In non-vacuum conditions, the dimeric $[Co(BTSA)_2]_2$ appears to have a lower onset temperature for mass loss. However, in ALD conditions, $Co(BTSA)_2(THF)$ can be evaporated already at 55 °C while $[Co(BTSA)_2]_2$ requires a source temperature of 70 °C.

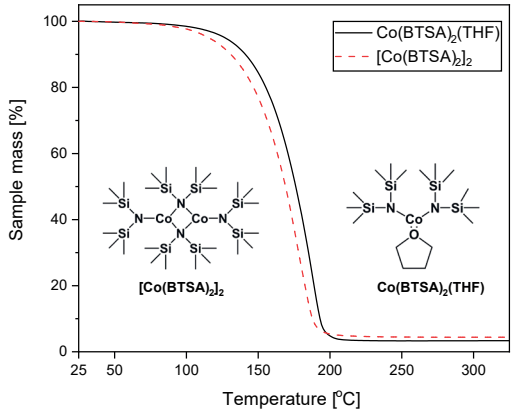

Figure 8. TGA graphs of $[Co(BTSA)_2]_2$ and $Co(BTSA)_2(THF)$. Image reproduced from Journal of Vacuum Science and Technology A, Vol. 37, 010908, T. Iivonen *et al.*: "Atomic layer deposition of cobalt(II) oxide thin films from $Co(BTSA)_2(THF)$", with the permission of the American Vacuum Society.

All film deposition experiments were done using $Co(BTSA)_2(THF)$ due to its lower source temperature requirement. The onset of thermal decomposition of $Co(BTSA)_2(THF)$ was found to be approximately 275 °C as evidenced by the formation of silvery gray metallic deposit on the hot end of the cobalt precursor tube at this temperature. No visual indication of thermal decomposition of $Co(BTSA)_2(THF)$ was observed at deposition temperatures of 250 °C and lower.

Based on post-deposition thickness measurements, the $Co(BTSA)_2(THF) + H_2O$ process showed good ALD characteristics. The GPC of this process had a strong dependence on temperature. At temperatures of 75 – 125 °C, GPC of 1.1 – 1.2 Å was obtained (Figure 9a). Increasing the deposition temperature above 125 °C resulted in decreased GPC. Film growth was found to be saturative at 100 and 200 °C with respect to both the cobalt precursor and H_2O (Figure 9 b). Moreover, a linear relationship between film thickness and the number of applied deposition cycles was confirmed at both 100 and 200 °C (Figure 9c).

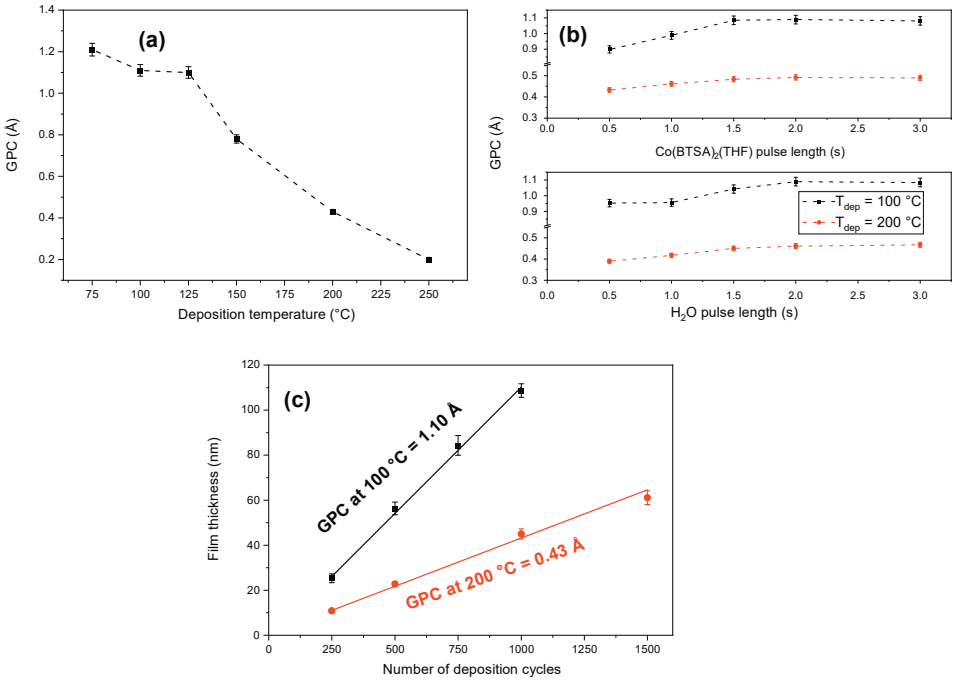

Figure 9. ALD characteristics of the $Co(BTSA)_2(THF) + H_2O$ ALD process. (a) The effect of temperature on GPC, (b) saturation studies at 100 and 200 °C and (c) film thickness as a function of the number of deposition cycles at 100 and 200 °C.

Based on GI-XRD analyses, films deposited at 75 – 200 °C were a mixture of the cubic and hexagonal wurtzite phases of cobalt monoxide. No reflections assignable to Co_3O_4 were observed. The degree of crystallinity of films deposited at all temperatures was low and the films deposited at 250 °C were X-ray amorphous. The low crystallinity is due to the relatively high levels of H, N and Si impurities remaining in the films (Table 7).

Table 7. Elemental composition (at-%) of cobalt oxide films deposited from $Co(BTSA)_2(THF)$ + H_2O at 75–250 °C.

T_{dep} (°C)	Co	O	H	C	Si	Co:O	Si:C
75	37.6 ± 0.4	46.7 ± 0.5	12.1 ± 0.5	1.9 ± 0.1	1.8 ± 0.1	0.81	0.95
100	38.3 ± 0.4	41.9 ± 0.8	15.2 ± 1.5	2.1 ± 0.1	2.2 ± 0.1	0.91	1.1
125	34.5 ± 0.3	44.0 ± 0.5	16.7 ± 0.6	2.3 ± 0.1	2.5 ± 0.1	0.78	1.1
150	34.0 ± 0.3	41.3 ± 0.7	18.7 ± 1.3	2.6 ± 0.1	3.3 ± 0.1	0.82	1.3
200	33.6 ± 0.4	46.0 ± 0.8	13.0 ± 1.4	2.1± 0.1	5.4 ± 0.2	0.73	2.6
250	32.5 ± 0.4	46.7 ± 0.9	12.3 ± 1.4	2.1 ± 0.2	6.4 ± 0.3	0.70	3.1

From Table 7 it can be observed that the amount of Si impurities in the films is increasing with increasing deposition temperature which suggests that $Co(BTSA)_2(THF)$ is (partially) decomposing during the surface reactions. Importantly, the amount of nitrogen in all films was below the detection limit of ToF-ERDA (approximately 0.2 at-%). As no nitrogen impurities were present in the films while silicon impurities were, it is evident that the N–Si bond in the BTSA ligands is labile under the film deposition conditions. As silicon has a strong affinity to form covalent bonds with oxygen,[173] it is likely that Si is incorporated in the films as $–O–Si–Me_x$ moieties (Me = methyl, x = 1–3). The Si:C ratio in the films increases from approximately 1.0 at 75 – 125 °C up to 3.1 at 250 °C, which indicates that also the Si–C bonds in the BTSA ligands are broken during the film deposition. Formation of the $–O–Si–Me_x$ surface terminations has been suggested to explain the decrease in GPC with increasing deposition temperature, as these surface groups hinder the chemisorption of both the metal precursor and H_2O and therefore inhibit the film growth.[174]

Concerning the hydrogen impurities, hydrogen can exist in the films as two different chemical species, cobalt hydroxide and as part of methyl groups originating from the BTSA ligands. Based on XPS studies, films deposited at all temperatures contain $Co(OH)_2$ (Figure 10). In fact, within the probing depth of XPS, the intensity of the hydroxyl peak is greater than that of the lattice oxide for films deposited at all temperatures. Notably, the reaction between CoO and H_2O to form $Co(OH)_2$ is thermodynamically favorable,[18] and therefore the formation of $Co(OH)_2$ can occur either during the film deposition or during post-deposition exposure to ambient moisture. According to ToF-ERDA depth profile measurements, hydrogen is distributed conformally throughout the films, which implies that exposure to ambient moisture is not the sole origin of the hydrogen impurities.

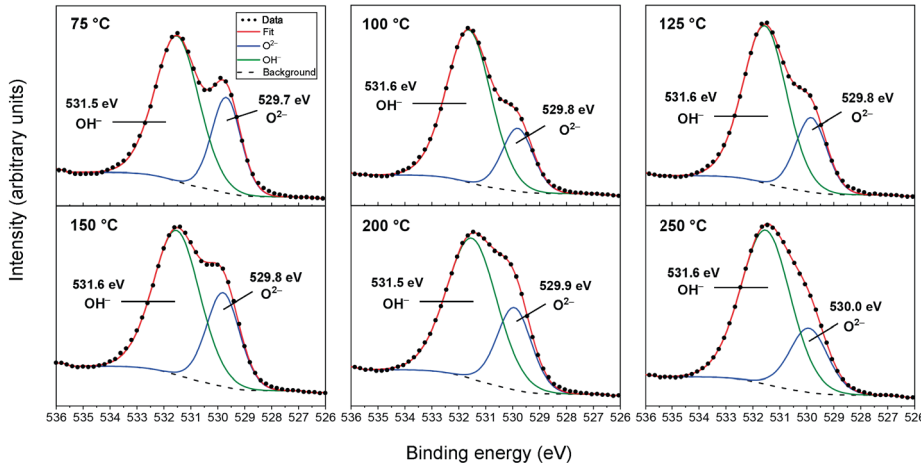

Figure 10. Photoelectron spectra in the O 1s binding energy region for films deposited using $Co(BTSA)_2(THF)$ + H_2O at 75 – 250 °C.

The surface chemistry of the $Co(BTSA)_2(THF)$ + D_2O ALD process at 100 °C was studied *in-situ* using QMS and QCM. At this deposition temperature, the amount of Si impurities was low in comparison to the other deposition temperatures, approximately 2 at-%. This signifies that the majority of the surface reactions at 100 °C are ligand exchange reactions which result in the deposition of CoO, $Co(OH)_2$ or both. The QMS measurements were done by following two signals, m/z = 72, which corresponds to THF, and m/z = 147, which is the most intensive ionization fragment of the deuterated BTSA ligand (D-BTSA) (Figure 11 a).

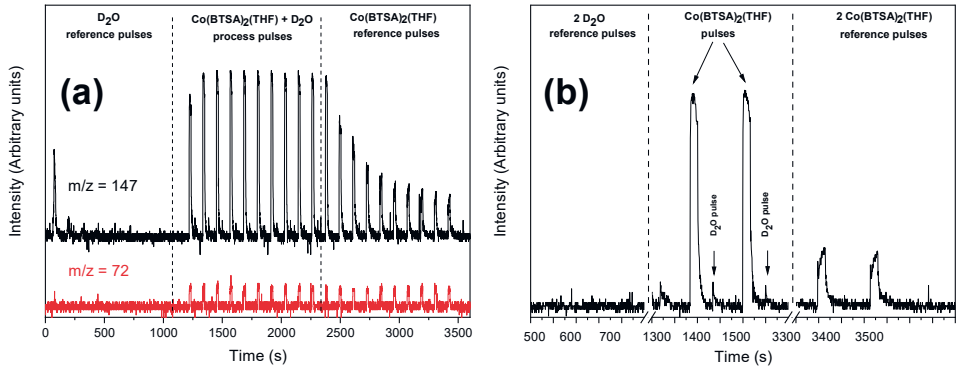

Figure 11. (a) QMS data for m/z = 72 (THF^+) and m/z = 147 at 100 °C. (b) QMS data for m/z = 147 at 100 °C for two cycles of the $Co(BTSA)_2(THF)$ + D_2O process.

The signal for m/z = 72 was observed during the process pulses (cobalt precursor pulse) and also during the consecutive reference pulses of $Co(BTSA)_2(THF)$ (Figure 11a). The intensity of m/z = 72 during the process pulses and the cobalt precursors reference pulses was constant. This indicates that during the process pulses, THF is released from the parent molecule when $Co(BTSA)_2(THF)$ adsorbs on the film surface. During the reference pulses, THF is separated from $Co(BTSA)_2(THF)$ upon ionization in QMS. As THF is a weak Lewis

base and has a high vapor pressure, it can simply desorb from the surface of the deposited film and is therefore unlikely to be incorporated in the deposited material as an impurity.

The analysis of the reaction mechanism was based on measuring the intensities for m/z = 147 during the cobalt precursor pulse and the D_2O pulse. As the QMS analysis is based on measuring the ratio of ligands released during the different precursor pulses, this technique cannot distinguish whether the deposited material is CoO or $Co(OD)_2$. A general scheme for the deposition of an arbitrary mixture of CoO and $Co(OD)_2$ can be presented using Eqns. (1) – (3). In these equations, n determines the stoichiometry of the deposited films, i.e. $n = 0$ corresponds to pure $Co(OD)_2$ and $n = 1$ corresponds to pure CoO. The surface species in Eqns. (1) – (3) are designated with an asterisk *. As THF was found to have a passive role in film deposition, it has been omitted from the reaction equations for clarity.

Net reaction: $(0 < n < 1)$

$$Co(BTSA)_2\,(g) + (2 - n)\,D_2O\,(g) \rightarrow CoO_n(OD)_{(2-2n)}\,(s) + 2\,D\text{–}BTSA\,(g) \quad (1)$$

Cobalt precursor pulse:

$$x\,OD^* + Co(BTSA)_2\,(g) \rightarrow O_x\text{–}Co(BTSA)_{(2-x)}^* + x\,D\text{–}BTSA\,(g) \quad (2)$$

D_2O pulse:

$$O_x\text{–}Co(BTSA)_{(2-x)}^* + (2-n)\,D_2O\,(g) \rightarrow CoO_n(OD)_{(2-2n)}\,(s) + x\,OD^* + (2-x)\,D\text{–}BTSA\,(g) \quad (3)$$

The ratio of D-BTSA ligands released during the cobalt precursor pulse and the D_2O pulse, R, is

$$R = \frac{x}{2 - x} \quad (4)$$

Solving (4) for x gives $x = \frac{2R}{1 + R}$.

As observed from Figure 11b, the intensity of m/z = 147 is far greater during the $Co(BTSA)_2(THF)$ pulse than during the D_2O pulse. This alone suggests that a vast majority of the ligand exchange reactions occurs during the cobalt precursor pulse. Numerical integration of the QMS signals yields $x \approx 1.90$ which states that, on average, 95 % of the BTSA ligands are released from the film surface during the cobalt precursor pulse.

In addition to QMS, the surface chemistry of the $Co(BTSA)_2(THF) + D_2O$ process was also studied with QCM. The QCM trace presented in Figure 12 shows an irreversible mass increase during both the cobalt precursor and the D_2O pulses. These events signify film deposition. During the purging periods following the precursor pulses, mass change is

negative. These events are most likely linked to the reversible adsorption of the cobalt precursor or the reversible physisorption of D-BTSA and D_2O, respectively.

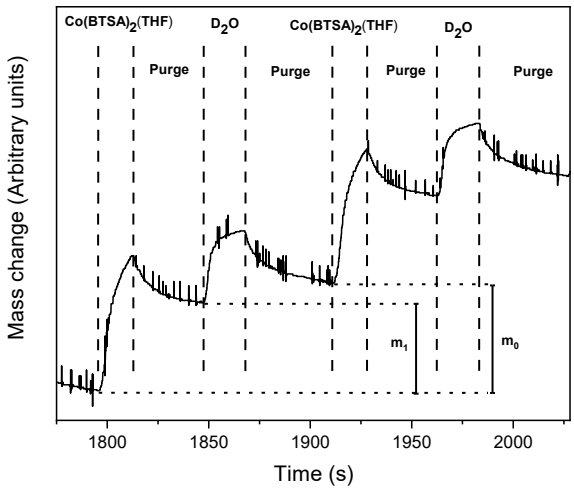

Figure 12. QCM data for the $Co(BTSA)_2(THF) + D_2O$ process at 100 °C. Image reproduced from Journal of Vacuum Science and Technology A, Vol. 37, 010908, T. Iivonen *et al.*: "Atomic layer deposition of cobalt(II) oxide thin films from $Co(BTSA)_2(THF)$", with the permission of the American Vacuum Society.

In the QCM trace shown in Figure 12, m_1 represents the change in mass after the cobalt precursor pulse and the following purge, while m_0 is the mass change after a complete ALD cycle. In terms of Eqns. (1) – (3), m_1 and m_0 have the following relationship:

$$\frac{\Delta\text{m after a Co(BTSA)}_2\text{THF pulse and purge}}{\Delta\text{m after a full process cycle}} \equiv \frac{m_1}{m_0} \equiv \frac{\text{M Co(BTSA)}_2 - x\,\text{M (D–BTSA)}}{\text{M CoO}_n\text{(OD)}_{(2-2n)}} \tag{5}$$

Solving (5) for x yields

$$x = \frac{[\text{M (Co(BTSA)}_2) - \frac{m_1}{m_0}\text{M (CoO}_n\text{(OD)}_{(2-2n)})]}{\text{M (D–BTSA)}} \tag{6}$$

Based on the QCM trace in Figure 12, $m_1 / m_0 \approx 0.80$. Assuming that the deposited material is pure CoO, i.e. $n = 1$, gives $x = 1.96$. On the other hand, using $n = 0$, which corresponds to the deposition of $Co(OD)_2$ gives $x = 1.86$. Both values are in agreement with the value of $x \approx 1.90$ obtained with QMS. Therefore, the *in-situ* measurement data alone cannot give a definitive answer on whether the deposited material is CoO, $Co(OD)_2$ or a mixture thereof.

However, the release of deutered BTSA ligands during the cobalt precursor pulses is a clear indication that film growth proceeds via the ligand exchange mechanism.

Based on the compositional analysis of the films, as well as the *in-situ* studies, it is clear that $Co(BTSA)_2(THF)$ is not an ideal precursor for ALD of cobalt oxide thin films. While the amount of impurities in the films deposited using this chemistry can be minimized by performing film deposition at low temperatures, other ALD cobalt oxide chemistries, such as those based on cobalt amidinate precursors[120,122] are more suitable for depositing impurity-free and stoichiometric CoO.

6.1.2. $Co(^{t\text{-}Bu}DAD)_2 + O_3$ II

$Co^{t\text{-}Bu}(DAD)_2$ (Figure 6) is a diazadienyl compound that was initially used in ALD for depositing metallic cobalt films.[175–177] In this work, $Co^{t\text{-}Bu}(DAD)_2$ was used together with O_3 for depositing cobalt oxide films. In the film deposition experiments, a source temperature of 95 °C was used for $Co^{t\text{-}Bu}(DAD)_2$. The highest deposition temperature was 200 °C, at which grey metallic deposit formed on the hot end of the precursor glass tube used for this cobalt precursor. No visual indication of decomposition was observed at temperatures of 180 °C and lower. However, films deposited at 130 °C and above suffered from severe thickness gradients along the direction of the precursor vapor flow. This thickness non-uniformity was caused by the decomposition of O_3 on the catalytic cobalt oxide surface. Uniform films were obtained at deposition temperatures of 120 °C and below. At these temperatures GPC was 0.95 – 1.20 Å (Figure 13a). At 120 °C, the film growth was saturative with respect to both precursors (Figure 13b,c). In addition, the thickness of films deposited at 120 °C increased linearly with increasing number of deposition cycles (Figure 13d).

Based on GI-XRD measurements, films deposited on Si substrates at 120 °C were polycrystalline Co_3O_4 (Figure 14a). No reflections indicating a presence of CoO were detected. Annealing the films in air resulted in an increase of crystallinity, while changing the annealing atmosphere to N_2 allowed the films to be reduced to CoO at 700 °C (Figure 14b).

The deposition of phase-pure Co_3O_4 thin films was evident also from ToF-ERDA and XPS measurement data. According ToF-ERDA, the Co:O ratio in films deposited at 120 °C was 0.70, which is close to the stoichiometry of pure Co_3O_4, 0.75 (Table 8). The films contained approximately 5 at-% hydrogen and < 2.0 at-% carbon as impurities. Based on the ToF-ERDA depth profiles, the hydrogen impurities were distributed uniformly throughout the films (Figure 15a). This indicates that the hydrogen impurities are incorporated in the films during film deposition. Possible mechanisms for the incorporation of the hydrogen impurities are the incomplete combustion of the $^{t\text{-}Bu}$DAD ligands or the adsorption of by-product H_2O on the surface of the growing film. According to the XPS measurements, the hydrogen present in the films forms cobalt hydroxide (Figure 15b).

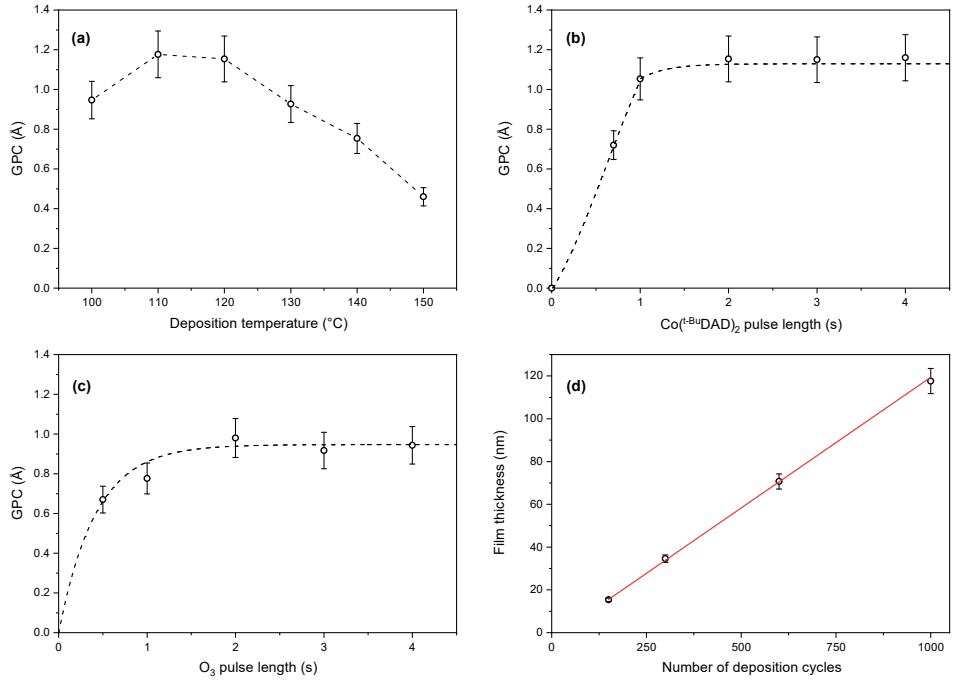

Figure 13. ALD characteristics of the $Co^{t\text{-}Bu}(DAD)_2 + O_3$ ALD process. (a) the effect of temperature on GPC, (b) and (c), saturation studies at 120 °C and (d) film thickness as a function of the number of deposition cycles at 120 °C.

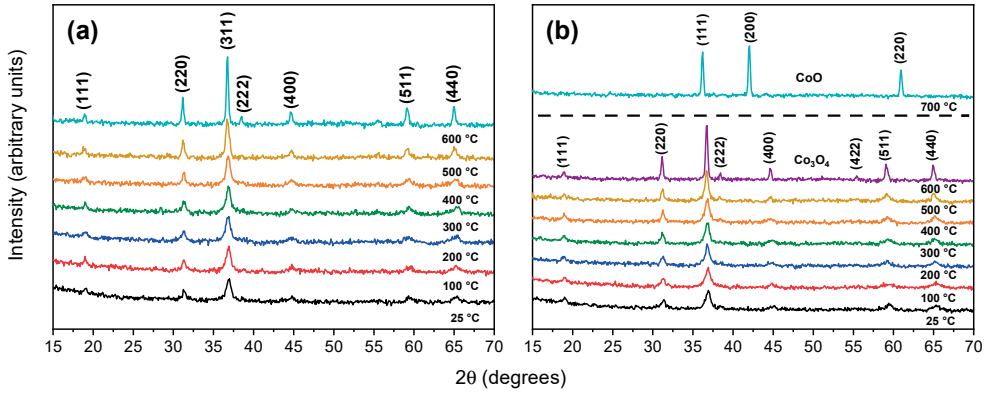

Figure 14. HT-XRD diffractograms of Co_3O_4 films deposited at 120 °C and annealed in (a) air and (b) dynamic N_2 atmosphere. The measurement temperature is shown under each diffractogram.

Table 8. Elemental composition (at-%) of a Co_3O_4 film deposited using $Co^{t\text{-}Bu}(DAD)_2$ and O_3 at 120 °C.

Co	O	H	C	N	Co:O
38.4 ± 0.4	54.6 ± 0.6	4.8 ± 0.5	1.6 ± 0.1	0.7 ± 0.1	0.70

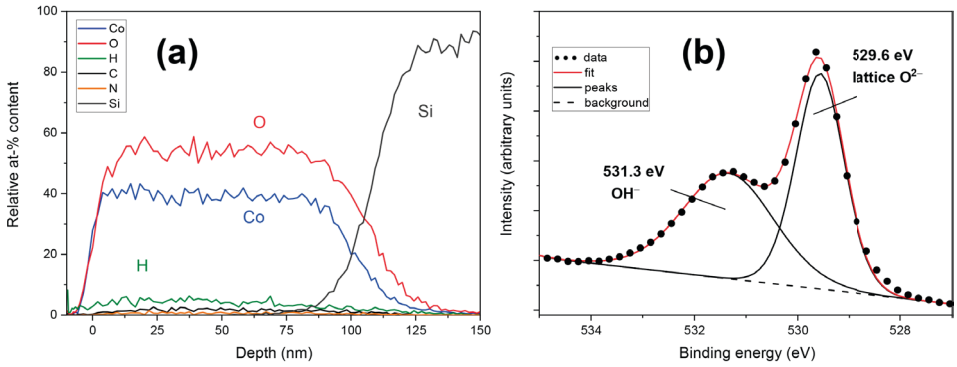

Figure 15. (a) ToF-ERDA depth profile and (b) X-ray photoelectron spectrum in the O 1s binding energy range of a 120 nm thick Co_3O_4 film deposited at 120 °C.

6.2. ALD of copper oxide thin films

The research on copper oxide thin films resulted in the development of two new ALD processes. The $Cu(OAc)_2 + H_2O$ process can be used to deposit Cu_2O thin films,[IV] whereas the $Cu(dmap)_2 + O_3$ precursor combination produces CuO films.[I]

6.2.1. $Cu(OAc)_2 + H_2O$ [IV]

Copper(II) acetate [$Cu(OAc)_2$] (Figure 7) is an interesting ALD precursor in a sense that Cu(I) oxide films are obtained when H_2O is used as the oxygen source. This indicates that copper is reduced from Cu^{2+} to Cu^{+} during the film deposition. According to thermogravimetric and mass spectrometric studies reported in the literature, reduction of $Cu(OAc)_2$ occurs upon heating *in vacuo* and results in the formation of volatile Cu(I) acetate, CuOAc.[178,179] In the following text, the copper precursor in the gas phase is referred to as CuOAc as the evaporating copper species is copper(I) acetate.

Film deposition experiments were done in the temperature range of 180 – 240 ºC using either $Cu(OAc)_2 \cdot H_2O$ or anhydrous $Cu(OAc)_2$ as the starting copper precursor. No difference could be observed between the films deposited from $Cu(OAc)_2 \cdot H_2O$ and those deposited from anhydrous $Cu(OAc)_2$. No film growth occurred with $Cu(OAc)_2 \cdot H_2O$ when the H_2O pulse was omitted from the process sequence. This indicates that the water

of crystallization in $Cu(OAc)_2 \cdot H_2O$ does not contribute to the film growth. Films deposited at 240 ºC had a metallic appearance which indicates that CuOAc is decomposing reductively or undergoing disproportionation at this temperature. Films deposited on glass substrates at 180 – 220 ºC were yellow and partially transparent, which is characteristic for nano-crystalline Cu_2O thin films.

The GPC of this process at 180 – 240 ºC was approximately 0.11 – 0.13 Å (Figure 16a). Based on saturation experiments at 200 ºC, the film growth was self-limiting with respect to both CuOAc and H_2O (Figure 16 b,c). In the early stages of the film growth, i.e. before a continuous copper oxide film was formed on the native oxide terminated Si (100) substrate, the GPC was 0.11 Å. For continuous, thicker films deposited using 3000, 5000 and 7000 cycles, GPC decreased to 0.08 Å. This entails that the adsorption density of CuOAc is higher on a SiO_2 surface than on a Cu_2O surface. A possible explanation for this observation is that hydroxyl groups on Cu_2O surfaces are less stable than Si-OH surface groups. According to Korzhavyi *et al*., Cu(I) hydroxyls are labile and undergo thermal decomposition to Cu_2O.[58] In this case the main film deposition mechanism would be the molecular adsorption of CuOAc on the Cu_2O surface, followed by the ligand exchange reaction during the water pulse.

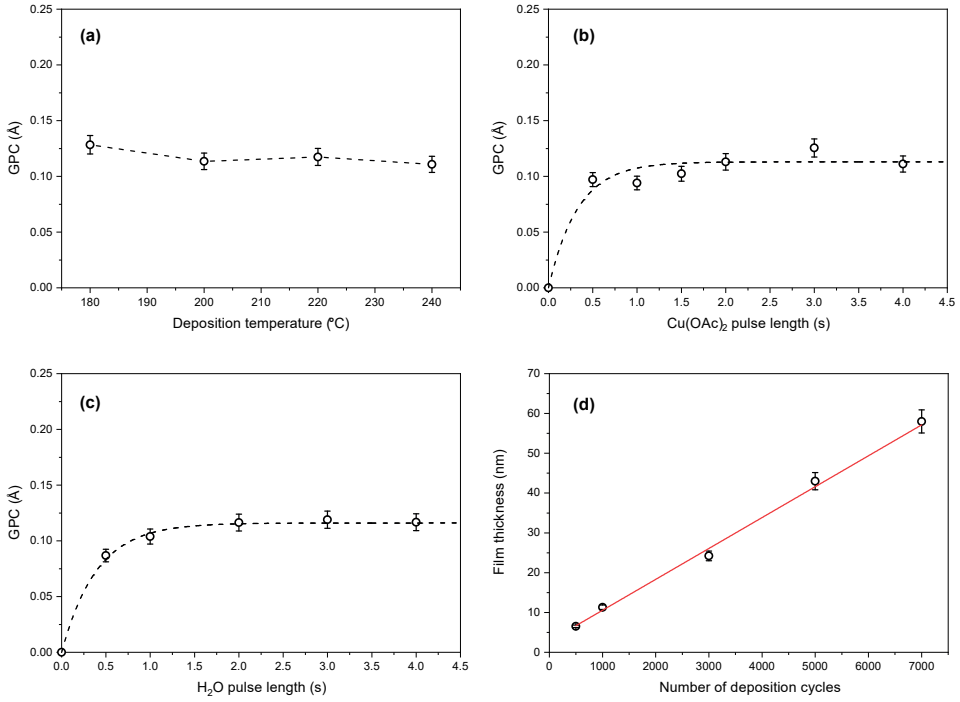

Figure 16. ALD characteristics of the $Cu(OAc)_2$ + H_2O ALD process. (a) the effect of deposition temperature on GPC, (b) and (c) saturation studies at 200 ºC and (d) film thickness as a function of number of deposition cycles.

The film deposition mechanism which involves the molecular adsorption of CuOAc was supported by the results of *in-situ* reaction mechanism studies carried out using QMS and QCM. The QMS analysis was done by following the intensity of the primary electron ionization fragment of deuterated acetic acid (D–OAc, m/z = 43)[180] at 200 ºC. The molecular ion of deutered acetic acid, m/z = 61, was also detected but the signal to noise –ratio of the molecular ion of D-OAc was nearly zero. Thus, m/z = 61 was not used in the reaction mechanism analysis.

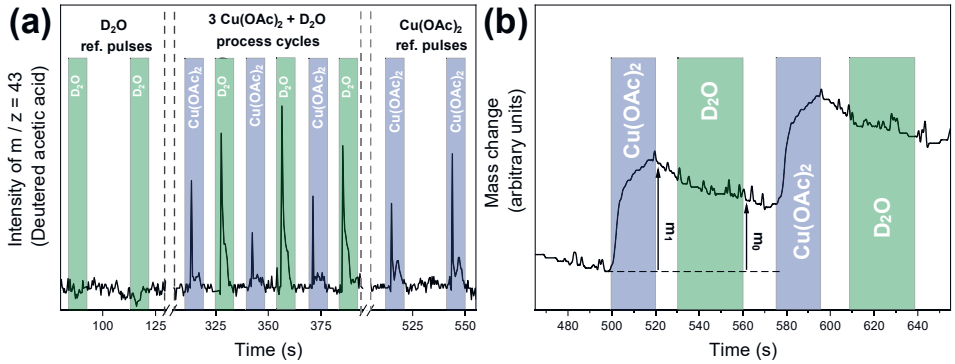

Figure 17. (a) QMS and (b) QCM data for the $Cu(OAc)_2$ + D_2O ALD process at 200 ºC.

During the ALD process, m/z = 43 was observed during both the copper precursor pulses and D_2O pulses (Figure 17a). Furthermore, m/z = 43 was detected also during the consecutive reference pulses of $Cu(OAc)_2$. This indicates that the signal for m/z = 43 arises from both CuOAc and D–OAc. The intensities of the QMS signals for m/z = 43 during the $Cu(OAc)_2$ process pulses and the reference pulses were virtually identical. In other words, the background-corrected intensity of m/z = 43 during the process pulses of $Cu(OAc)_2$ is close to zero. The chemical interpretation of this result is that CuOAc is adsorbing molecularly on the Cu_2O surface. In terms of half-reactions (8) – (9), x is zero.

Net reaction:

$$2\ CuOAc\ (g) + D_2O \rightarrow Cu_2O\ (s) + 2\ D\text{–}OAc\ (g) \quad (7)$$

Copper precursor pulse:

$$x\ OD^* + 2\ CuOAc\ (g) \rightarrow O_x\text{–}Cu_2(OAc)_{(2-x)}^* + x\ D\text{–}OAc\ (g) \quad (8)$$

D_2O pulse:

$$O_x\text{–}Cu_2(OAc)_{(2-x)}^* + D_2O\ (g) \rightarrow Cu_2O\ (g) + x\ OD^* + (2-x)\ D_2O\ (g) \quad (9)$$

The reaction mechanism involving the molecular adsorption of CuOAc was partially supported by the QCM data (Figure 17b). From the QCM trace, it can be seen that the QCM mass is increasing during the copper precursor pulse due to the adsorption of CuOAc.

During the following purge, a decrease in the QCM mass is observed, which can signify that CuOAc is desorbing from the surface. During the D_2O pulse, the rate of mass loss is lower than during the preceding purge. The decrease in mass during the D_2O pulse is due to the fact that the mass of the released deutered acetic acid ligands is greater than the mass of oxygen deposited in the film. During the purge following the D_2O pulse, the QCM mass continues to decrease, which can be related to the decomposition of Cu(I) surface hydroxyls to Cu_2O:

$$2\ \mathrm{CuOH\ (s)} \rightarrow \mathrm{Cu_2O\ (s)} + \mathrm{H_2O\ (g)} \tag{10}$$

Based on the QCM trace shown in Figure 17b, the m_1/m_0 ratio is approximately 1.44. The relationship between the QCM mass change and the amount of ligands x released during the copper precursor pulse is

$$\frac{\Delta\mathrm{m\ after\ a\ Cu(OAc)_2\ pulse\ and\ purge}}{\Delta\mathrm{m\ after\ a\ full\ process\ cycle}} \equiv \frac{m_1}{m_0} \equiv \frac{2\ \mathrm{M(CuOAc)} - x\ \mathrm{M\ (DOAc)}}{\mathrm{M\ (Cu_2O)}} \tag{11}$$

$$x = \frac{2\ \mathrm{M\ (CuOAc)} - \frac{m_1}{m_0}\mathrm{M\ (Cu_2O)}}{\mathrm{M\ (DOAc)}} \tag{12}$$

Solving Eqn. (12) for x using $m_1 / m_0 = 1.44$ yields $x \approx 0.64$. Based on this ratio, approximately 2/3 of the ligands of CuOAc would be released during the D_2O pulse and 1/3 during the copper precursor pulse. This apparent difference between the QMS and QCM results is likely caused by the low intensity of the QMS signals and the resulting uncertainty in the QMS data.

Based on GI-XRD measurements, the copper oxide films deposited from $Cu(OAc)_2 + H_2O$ at 180 – 220 ºC are polycrystalline Cu_2O (Figure 18a). No reflections assignable to CuO were detected. The films deposited at 240 ºC contained reflections assignable to metallic copper, which indicates that CuOAc is either decomposing reductively or disproportionation. The adhesion of the metallic copper deposited on Si and SLG at 240 ºC was poor and the films did not pass the Scotch tape adhesion test.

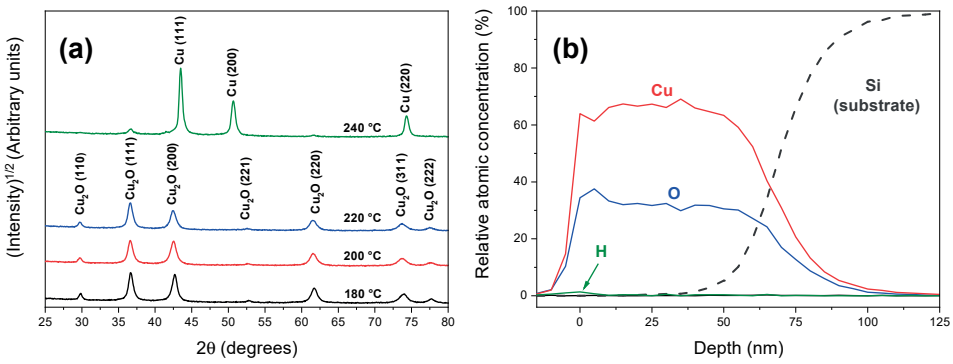

Figure 18. (a) GI-XRD patterns for films deposited using 5000 cycles at temperatures of 180 – 240 ºC. (b) ToF-ERDA depth profile for a Cu_2O film deposited using 7000 cycles.

According to ToF-ERDA measurements, the Cu_2O films deposited at 200 ºC are nearly stoichiometric (Table 9). The amount of both hydrogen and carbon impurities in the films is exceptionally low, 0.4 at-% H and ≤ 0.2 at-% C. Based on the ToF-ERDA depth profile shown in Figure 18b, hydrogen is concentrated on the film surface, while the bulk of the film is free of impurities. The scarcity of hydrogen impurities is explained by the lability of Cu(I) hydroxides.[58] The low amount of carbon impurities is explained by the fact that acetic acid, which is formed as a by-product in the ligand exchange reactions, is a stable compound that has a high vapor pressure,[181] and therefore desorbs cleanly from the film surface.

Table 9. Elemental composition (at-%) of a 50 thick Cu_2O film deposited using $Cu(OAc)_2$ + H_2O at 200 °C.

Cu	O	H	C	Cu:O
65.8	33.6	0.4	≤ 0.2	1.96

6.2.2. $Cu(dmap)_2$ + O_3 [I]

Similarly to $Co^{t-Bu}(DAD)_2$, $Cu(dmap)_2$ was initially used for the deposition of metallic thin films with both CVD and ALD.[147,182] This copper precursor is also reactive towards O_3, and as $Cu(dmap)_2$ exhibits good volatility, this precursor combination is well-suited for low-temperature ALD of copper oxide thin films.

The $Cu(dmap)_2$ precursor was evaporated at 65 ºC in all deposition experiments. Film deposition was carried out at 80 – 140 ºC. The onset for the decomposition of $Cu(dmap)_2$ was 150 ºC, as evidenced by the coloration of the hot end of the precursor glass tube at this temperature. No indication of thermal decomposition of $Cu(dmap)_2$ was observed at deposition temperatures of 140 ºC and lower.

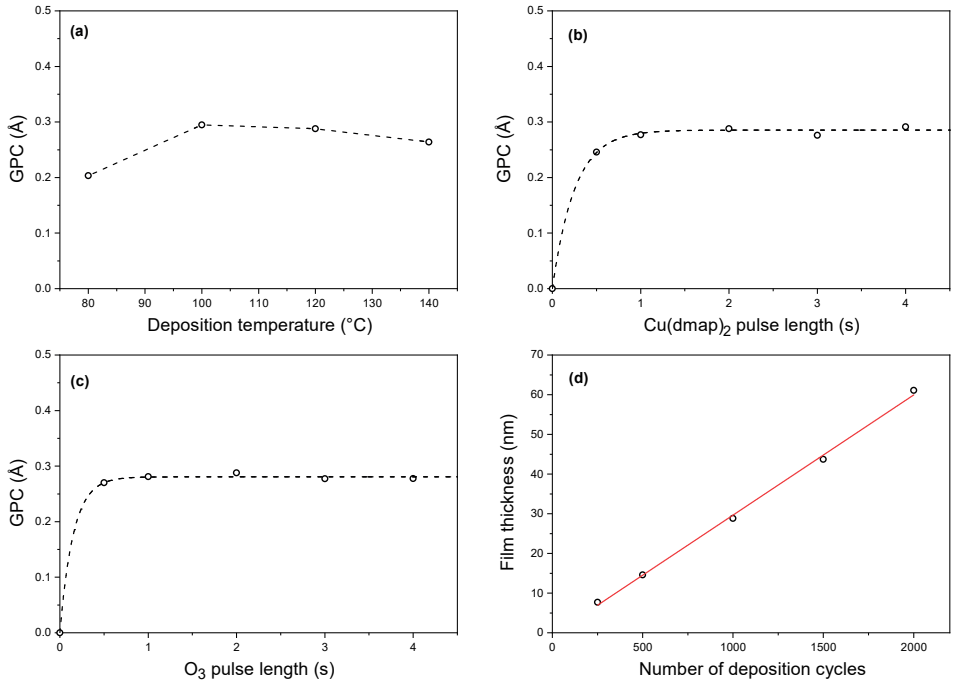

Figure 19. ALD characteristics of the $Cu(dmap)_2 + O_3$ process. (a) The effect of temperature on GPC, (b) and (c) saturation studies at 120 °C and (d) film thickness as a function of the number of cycles at 120 °C.

Contrarily to the report by Avila *et al.*,[143] using H_2O as the oxygen source did not result in film growth. GPC of the $Cu(dmap)_2 + O_3$ process was 0.20 Å at 80 ºC and 0.26 – 0.30 Å at 100 – 140 ºC (Figure 19a). Based on saturation experiments at 120 ºC, the film growth proceeded in a self-limiting manner with respect to both $Cu(dmap)_2$ and O_3 (Figure 19b,c). In further deposition experiments at 120 ºC, the relationship between film thickness and the number of deposition cycles was found to be linear at a GPC of 0.30 Å up to 2000 cycles, the highest cycle number studied (Figure 19d).

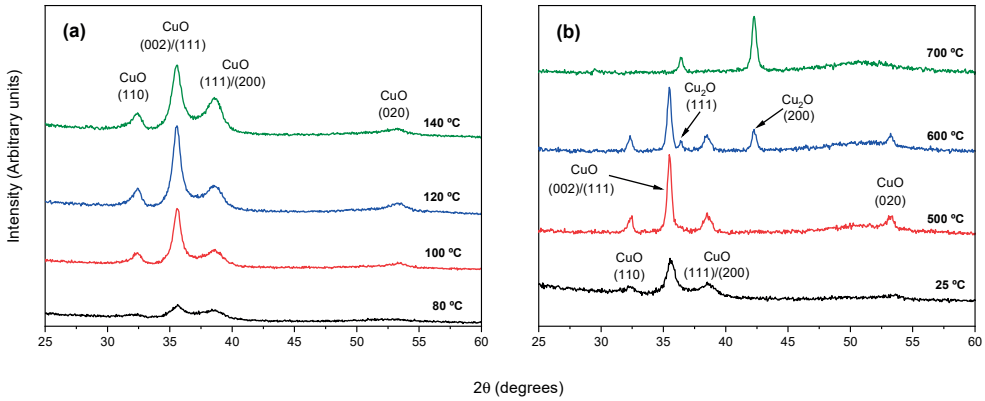

Figure 20. (a) GI-XRD diffractograms of CuO films deposited at 80–140 ºC using 1000 cycles. (b) HT-XRD diffractograms for a 30 nm CuO film deposited at 120 ºC and annealed at different temperatures under an N_2 atmosphere.

Based on GI-XRD measurements, films deposited from $Cu(dmap)_2 + O_3$ on Si and SLG at 80 – 140 ºC were polycrystalline CuO (Figure 20a). For the as-deposited films, no reflections assignable to metallic Cu or Cu_2O were detected. Notably, the films deposited at 80 ºC were only weakly crystalline, while increasing the deposition temperature to 100 ºC and above resulted in increased degree of crystallinity. Further improvement in film crystallinity was achieved by high temperature annealing in a dynamic N_2 atmosphere at 500 ºC (Figure 20b). Increasing the annealing temperature resulted in a partial reduction to Cu_2O at 600 ºC and complete reduction at 700 ºC.

Surface morphology studies of as-deposited films with AFM (Figure 21) yielded results that were in agreement with the GI-XRD measurements. The approximately 20 nm thick CuO film deposited at 80 °C showed morphology typical for a weakly crystalline or amorphous material as well as a low root-mean-square roughness value of 0.45 nm. The films deposited at 100 – 140 °C, on the other hand, consisted of grains that were 30 nm or smaller in diameter. The RMS roughnesses of the films deposited at 100 – 140 ºC were 1.3 – 1.8 nm, which correspond to 4 – 6 % of the film thicknesses.

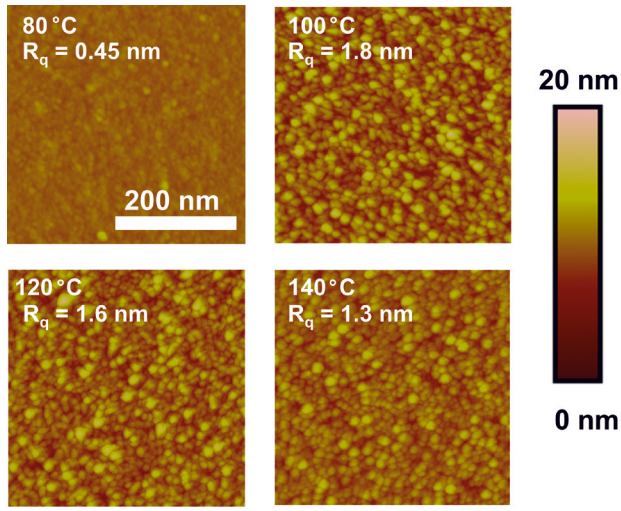

Figure 21. Top-view AFM images of CuO films deposited at 80 – 140 C using 1000 cycles. The 200 nm scale bar and the 0 – 20 nm height scale apply to all images.

XPS measurements showed that films obtained at all deposition temperatures contained copper solely as Cu^{2+}. The photoelectron spectra in the Cu 2p binding energy range contained Cu $2p_{3/2}$ and Cu $2p_{1/2}$ peaks at 933.7 ± 0.1 and 953.6 ± 0.1 eV, respectively, which is characteristic for CuO (Figure 22a).[167] The photoelectron spectra in the O 1s binding energy range contained peaks for both the lattice oxide of CuO (529.4 ± 0.1 eV) and hydroxide or carbonate (531.1 ± 0.1 eV) (Figure 22b). For the films deposited at 80 °C, the intensity of the peak assignable to $Cu(OH)_2$ / $CuCO_3$ was greater than for the films deposited at 100 – 140 ºC. This indicates that the films deposited at the lowest temperature contain high amount of hydrogen or carbon impurities. The incorporation of light element impurities in the films was also observed in the ToF-ERDA measurements (Figure 22c, Table 10). The CuO films deposited at 80 ºC contained approximately 7 at-% hydrogen and 2 at-% of carbon. Increasing the deposition temperature resulted in films with less impurities and the CuO films deposited at 140 ºC contained only 2 at-% H and < 0.5 at-% C.

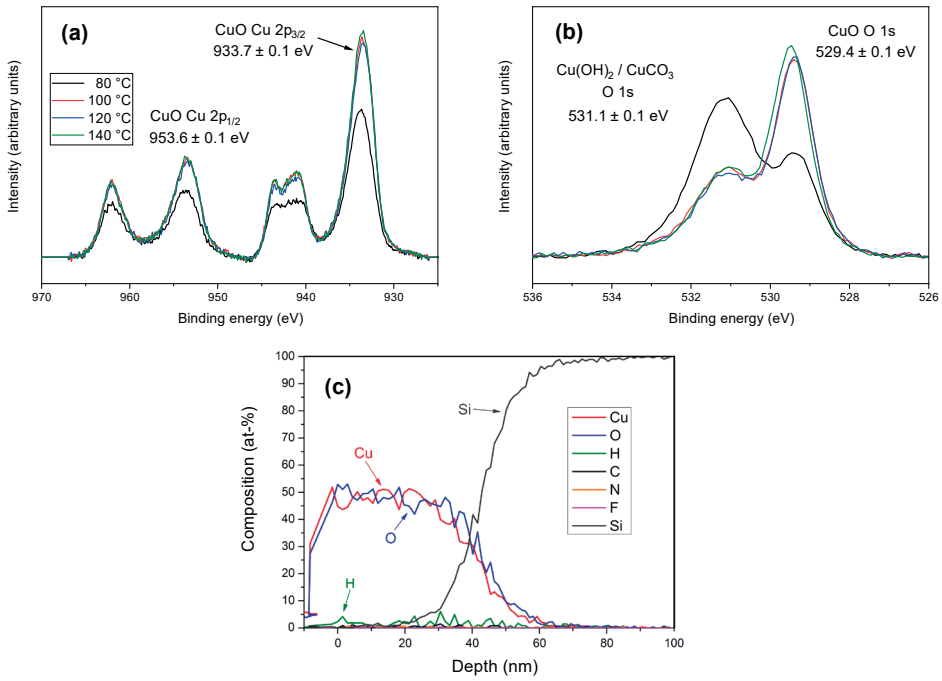

Figure 22. X-ray photoelectron spectra for binding energy regions of (a) Cu 2p and (b) O 1s measured for CuO films deposited at 80 – 140 °C. Panel (c) shows a ToF-ERDA depth profile of a CuO film deposited using 2000 cycles at 120 °C.

Table 10. Elemental composition (at-%) of copper oxide films deposited from $Cu(dmap)_2$ + O_3 at 80–140 °C as measured with ToF-ERDA.

T_{dep} (°C)	Cu	O	H	C	N	Cu:O
80	44.4 ± 0.7	45.0 ± 0.8	7.4 ± 0.6	2.0 ± 0.4	0.9 ± 0.3	0.99
100	47.0 ± 0.7	48.9 ± 0.8	3.1 ± 0.5	0.6 ± 0.3	0.3 ± 0.2	0.96
120	47.0 ± 0.8	49.3 ± 0.9	2.8 ± 0.5	0.5 ± 0.3	0.2 ± 0.2	0.95
140	49.7 ± 0.8	47.6 ± 0.8	1.9 ± 0.5	0.4 ± 0.3	0.2 ± 0.2	1.04

6.3 Functional properties of CoO, Co_3O_4, Cu_2O and CuO films

As discussed throughout this thesis, cobalt oxide and copper oxide thin films exhibit p-type semiconductivity and absorb light at visible wavelengths. Therefore, these materials have potential to be utilized in various optical, electronic and catalytic applications. Optical properties of cobalt oxide and copper oxide thin films deposited in this work were evaluated using UV-Vis transmittance measurements. Catalytic properties of Co_3O_4 nanoparticles and films deposited using the $Co^{t-Bu}(DAD)_2 + O_3$ ALD process were tested in the photoelectrochemical water splitting reaction. Optoelectronic properties of Cu_2O films deposited from $Cu(OAc)_2 + H_2O$ were studied by making photoconductor test structures.

6.3.1 Optical properties and band gap analysis

Optical properties of Co_3O_4, Cu_2O and CuO films deposited during this work were evaluated with UV-Vis transmittance measurements and using the Tauc plot method (Figure 23).[I–IV]

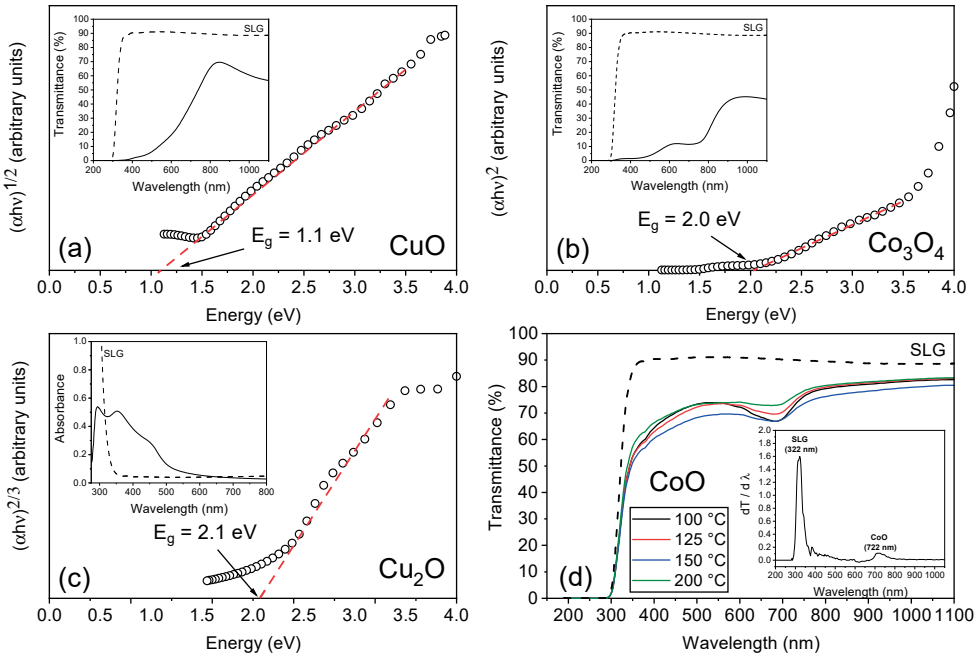

Figure 23. Band gap analyses for (a) a 100 nm thick CuO film deposited using $Cu(dmap)_2 + O_3$, (b) a 100 nm thick Co_3O_4 film deposited using $Co^{t-Bu}(DAD)_2 + O_3$ and (c) a 30 nm thick Cu_2O film deposited using $Cu(OAc)_2 + H_2O$. Panel (d) shows transmittance data of CoO films deposited from $Co(BTSA)_2(THF) + H_2O$ at 100 – 200 °C. The insets of panels (a) – (c) show the transmittance / absorbance data used for calculating the band gap values. The inset of panel (d) shows a derivative of the transmittance with respect to wavelength for a CoO film deposited at 200 °C.

The indirect allowed band gap obtained for a 100 nm CuO film deposited from $Cu(dmap)_2$ + O_3 at 120 °C was 1.1 eV.[I] This value is lower than what is normally reported for bulk CuO, 1.4 eV.[57,183] However, the experimentally obtained value is in agreement with the band gap values of 1.1 – 1.2 eV reported for sub-100 nm thick CuO deposited using the $Cu(thd)_2$ + O_3 ALD chemistry.[54] For copper oxide films deposited from (hfac)Cu(DMB) + O_3 chemistry and crystallized as CuO with RTA at 300 – 500 °C, band gaps of 1.4 – 1.5 eV were reported.[68] The authors of the (hfac)Cu(DMB) + O_3 process did not, however, specify whether the band gap analysis was done accounting for direct or indirect transitions. As a note, in several reports on the optical properties of CuO thin films found in the literature, the band gap analysis has been done with respect to direct allowed transitions. Owing to this misconception, band gaps values of larger than 1.5 eV are commonly reported.[56,184,185]

For a 120 nm thick Co_3O_4 film deposited using $Co^{t-Bu}(DAD)_2$ + O_3 at 120 °C, a direct allowed band gap of 2.0 eV was obtained (Figure 23b). The transmittance data shown in the inset of Figure 23b shows two distinct optical events at approximately 810 and 550 nm, respectively. The absorption event occurring at 810 nm corresponds to a charge transfer between Co^{2+} and Co^{3+}, while the optical event at approximately 550 nm corresponds to the excitation of electrons across the fundamental band gap.[12,15] The direct band gap value of 2.0 eV obtained for the Co_3O_4 films deposited in this work is in agreement with the values of 2.0 – 2.2 eV reported for ALD Co_3O_4 films deposited using the $CoCp_2$ + O_3 and $Co^{i-Pr}(DAD)_2$ + O_3 precursor combinations.[14,125] The band gap values of the single phase Co_3O_4 films deposited using ALD are also in agreement with the values of Co_3O_4 films obtained with other techniques, such as CVD (1.9 – 2.0 eV),[12] spray pyrolysis (2.1 eV)[186] and reactive magnetron sputtering (2.0 – 2.2 eV).[187]

For Cu_2O films deposited from $Cu(OAc)_2$ + H_2O at 200 °C, the Tauc plot analysis was carried out assuming for direct forbidden transitions, as prompted by Malerba *et al*.[52] For a 24 nm thick Cu_2O film deposited on glass, this approach yielded a band gap of 2.1 eV (Figure 23c), which is agreement with literature values reported form both bulk and thin film samples of Cu_2O.[52] The direct forbidden band gap value of 2.1 eV obtained in this work is not comparable to the band gap values reported for Cu_2O films deposited using other ALD chemistries, such as (hfac)Cu(TMVS) + H_2O and $Cu(dmamb)_2$ + H_2O because the band gap analyses in these studies were done with respect to direct allowed transitions.[49,142] The direct allowed band gap of Cu_2O films reported in these studies was 2.5 eV. As a comparison, when the Tauc plot analysis of Cu_2O films deposited in this work was done with respect to a direct allowed transition, a band gap of 2.4 eV was obtained.

The optical properties of CoO films deposited using the $Co(BTSA)_2(THF)$ + H_2O process at 100 – 200 °C were studied with transmittance measurements in the UV-Vis wavelength range (Figure 23d). Tauc plot analysis of the transmittance data did not yield valid results, as the band gap of CoO is approximately 6 eV [9,188] and therefore not accessible by transmittance measurements on films deposited on SLG. The transmittance data presented in Figure 23d includes a low intensity absorption event at 720 nm. This wavelength translates to photon energy of 1.7 eV, which does not correspond to any optical feature of CoO and is likely related to the $Co(OH)_2$ or silicon impurities present in the films.

6.3.2 Photoelectrochemical water splitting

For studying the electrocatalytic properties of cobalt oxide nanoparticles and thin films deposited with ALD, 10, 50, 100, 300, 500 and 1000 cycles of the $Co^{t-Bu}(DAD)_2 + O_3$ process were applied on 100 nm thick, polycrystalline anatase/rutile TiO_2 photoanodes at a deposition temperature of 120 °C.[II] In comparison to the reference TiO_2 photoanodes, the highest increase in photocurrent, incident photon-to-current efficiency (IPCE) and OER rate, approximately 30 %, were obtained with TiO_2 thin films modified with 10 cobalt oxide deposition cycles (Figure 24).

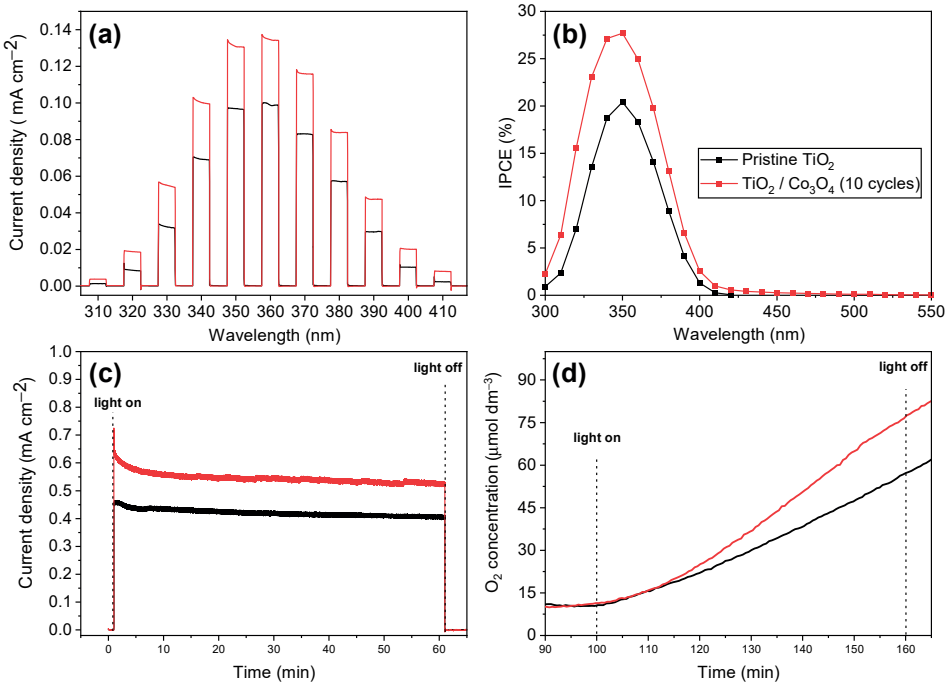

Figure 24. Photoelectrochemical properties of 100 nm TiO_2 photoanodes with (red) and without (black) modification with 10 cobalt oxide deposition cycles. (a) photocurrent transients at different illumination wavelengths, (b) IPCE–plot, (c) photocurrent over 60 minutes, (d) a snapshot of the rate of the oxygen evolution reaction during 60 minutes of irradiation.

Despite the relatively high GPC of the $Co^{t-Bu}(DAD)_2 + O_3$ process, 10 deposition cycles does not result in a continuous film, but cobalt oxide islands, or nanoparticles, are formed instead.[II] Increase in photoelectrochemical performance was observed also for photoanodes modified with 50, 100 and 300 cobalt oxide deposition cycles. However, photocurrent measurements with chopped illumination revealed that the photoanodes modified with thicker cobalt oxide overlayers suffered from a fast recombination of the photogenerated charges, which can be caused by the accumulation of holes in the electrocatalyst layer.[189] Based on the IPCE plot shown in Figure 24b, the surface modification of TiO_2 thin film photoanodes does not result in visible light activity. Instead, the improvement in the device performance stems from the capability of cobalt oxide nanoparticles and overlayers to extract photogenerated holes from TiO_2 and to catalyze the OER (Figure 24c,d).[27,28]

6.3.3 Photoconductivity

Photoconductivity is a known effect for both n-type and p-type semiconductors.[190] The fundamental mechanism of photoconduction in semiconductors is the light-induced excitation of electrons from the valence band to the conduction band. As a consequence, the concentration of free electrons or holes available to carry electric current is increased. In order to induce photoconductivity, the wavelength of irradiation must match the band gap of the semiconductor.

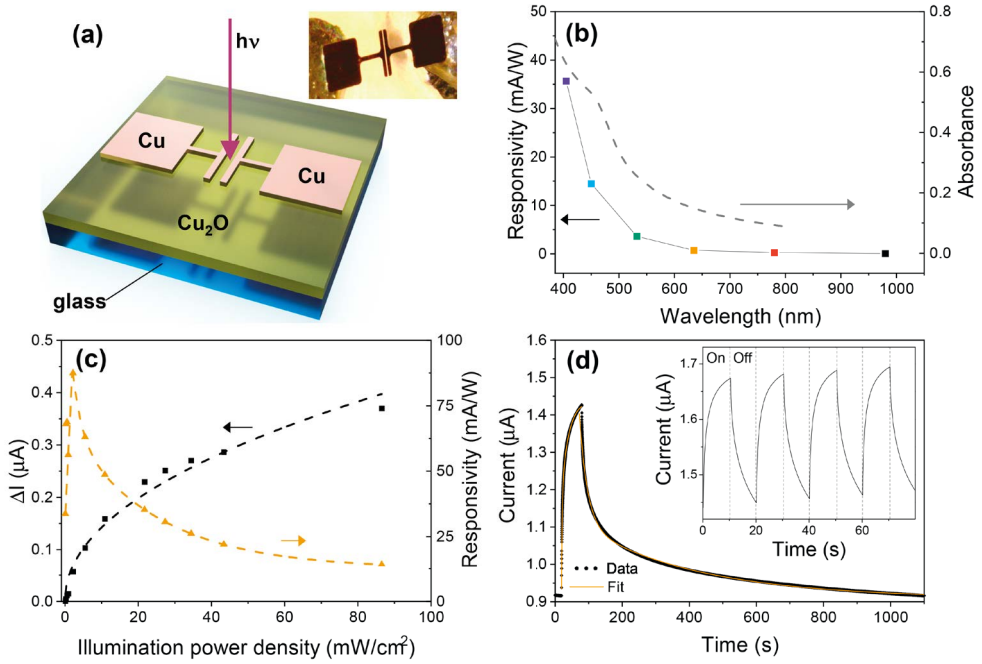

Figure 25. Optoelectronic properties of Cu_2O photoconductor devices. (a) Schematic presentation of the Cu_2O photoconductor test structure. Inset of panel (a) : Image of the photoconductor devices from glass side (back side). (b) Responsivity and absorbance as a function of illumination wavelength. (c) Relationship between photocurrent and responsivity on illumination light density. (d) Time-dependent photocurrent response of a device illumination for 1 minute. Inset of panel (d) : time-dependent photoresponse with chopped illumination (10 s on, 10 s off). In (c) and (d), a 405 nm laser was used for illumination. Image reproduced from **IV**, Copyright ® 2019 Authors, distributed under a Creative Commons CC BY License.

Cu_2O holds potential to be used in photodetection in the visible wavelength range due to its band gap of approximately 2.1 eV and a high absorption coefficient for visible wavelength photons.[52] The evaluation of the optoelectronic properties of approximately 24 nm thick Cu_2O films deposited at 200 °C consisted of photocurrent measurements and analysis of parameters related to photodetection, such as responsivity and time constants.[IV]

The responsivity of a photodetector is defined as

$$\mathrm{R} = \frac{I_{\mathrm{photo}}}{P_{\mathrm{light}}} = \frac{I_{\mathrm{light}} - I_{\mathrm{dark}}}{P_{\mathrm{d}} \cdot A} \quad , \tag{13}$$

where I_{photo} (ΔI) is the photocurrent, i.e. the difference between current under illumination (I_{light}) and dark current (I_{dark}). P_{light} is the power of the incident light at the sample surface. P_{light} can be also defined as the product of intensity P_{d} of the light source and the area of the device, A.

As seen from Figure 25b, the responsivity of the thin film photoconductor follows the absorbance of Cu_2O. When the illumination power density was kept constant, the highest responsivity and therefore, the highest photocurrent was observed when the device was activated using illumination at 405 nm. Upon illumination at this wavelength, a maximum in responsivity was reached at an incident power density of 1 mW cm^{-2} (Figure 25c). Therefore, the 24 nm thick device is saturated at very low illumination power densities. The increase in photocurrent under illumination at 405 nm was found to depend on the illumination power density according to $I_{\mathrm{photo}} \propto P_d{}^{(0.5)}$.

Temporal photocurrent measurements revealed that the photocurrent of the Cu_2O thin film device did not saturate even after 60 s of illumination (Figure 25d). The relaxation time of the device was correspondingly long, in the order of 300 s. The slow switching characteristics of Cu_2O are caused by the persistent photocurrent (PPC) effect, which has been suggested to originate from the trapping of electrons to intra-band gap states.[191] The PPC effect causes the conductivity of Cu_2O to slowly increase upon illumination and the increase in conductivity to persist under dark conditions. In comparison to bulk crystals of Cu_2O in which the PPC effect persist for several days,[51] the nanometer level thickness of the Cu_2O thin films contributes to a faster discharge of the PPC effect.

7 Conclusions

The goal of this PhD project was to explore and develop new chemistries for depositing cobalt oxide and copper oxide thin films using ALD. Notably, studies on deposition and characterization of thin films of cobalt oxides and copper oxides are of great importance, as these materials have the potential to enable various technologies, such as solar fuel production, thin film batteries and transparent electronics. Moreover, as the direct deposition of transition metals with ALD has proved to be challenging, the deposition of oxide films and subsequent post-deposition reduction to metals can offer an alternative route to enable both cobalt and copper metallization.

During the course of this work, two new cobalt oxide and two new copper oxide ALD chemistries were systematically evaluated and properties of the films obtained from each respective process thoroughly characterized. All four ALD processes developed in this work exhibited saturative growth behaviour. From the point of view of depositing uniform and conformal thin films, the saturative film growth mode is essential.

The $Co(BTSA)_2(THF) + H_2O$ precursor combination was found to produce cobalt oxide films that contained significant amounts of hydrogen, carbon and silicon as impurities. The amount of impurities in the films could be minimized by using a low deposition temperature, but the deposition of stoichiometric and pure CoO could not be achieved. The H impurities in the films originate either from hydroxides or the BTSA ligands. The BTSA ligands are also the origin of the C and Si impurities. No nitrogen was detected in the films, which suggests that the N–Si bond in the BTSA ligands is labile and likely to break under conditions that are typical for ALD of oxide thin films. Other possible mechanisms for H, C and Si impurity incorporation are the condensation of BTSA ligands or the reaction of BTSA ligands with OH groups.

$Co^{t\text{–}Bu}(DAD)_2$ proved to be a well-suited precursor for low-temperature (100 – 120 °C) ALD of cobalt oxide thin films. This precursor was unreactive toward H_2O, but using the more reactive O_3 as the oxygen source enabled the deposition of polycrystalline Co_3O_4 thin films. The GPC for this process was relatively high, approximately 1.0 – 1.2 Å depending on the deposition temperature. Based on ToF-ERDA measurements, the films deposited from $Co^{t\text{–}Bu}(DAD)_2 + O_3$ contained approximately 5 at-% of hydrogen, while the contents of carbon and nitrogen impurities were < 2.0 at-%. According to XPS analyses, hydrogen in the films is forming cobalt hydroxide. Furthermore, this low-temperature ALD chemistry was also shown to be suitable for depositing electrocatalytic cobalt oxide nanoparticles on TiO_2 thin film photoanodes and thereby increasing the performance of TiO_2 in the oxygen evolution reaction.

$Cu(dmap)_2$ was found to be an exemplary precursor for low-temperature copper oxide ALD. The films deposited with O_3 at 80 – 140 °C were polycrystalline CuO and contained low amounts of light impurities, < 7.4 at-% H, < 2.0 at-% C and < 0.9 at-% N. The optimal deposition temperature with respect to film crystallinity and purity was 120 °C. Despite the

high degree of crystallinity, surface roughnesses of the films were low, approximately 5 % of film thicknesses for 20 – 30 nm samples thick films on Si substrates.

The $Cu(OAc)_2 + H_2O$ ALD chemistry proved to be interesting in a sense that it produced Cu_2O thin films even though the oxidation state of copper in $Cu(OAc)_2$ is +2 and no separate reducing agent was used. This redox chemistry is explained by the thermally induced reduction of $Cu(OAc)_2$ to the volatile CuOAc. The Cu_2O films deposited at 200 °C using $Cu(OAc)_2 + H_2O$ were polycrystalline, phase-pure and virtually free of impurities. Even though ALD is well-known for its ability to produce high-quality thin films with low impurity content, the deposition of oxide films with only 0.4 at-% H and ≤ 0.2 at-% C can be considered to be exceptional. Based on *in-situ* reaction mechanism studies, the film growth in this process proceeds through ligand exchange and results in the formation of acetic acid.

Concerning future studies on the topic of this thesis, emphasis should be placed on developing new precursors suitable for depositing cobalt oxide and copper oxide thin films. A significant part of the metal precursors described in this work have been originally designed for the deposition of metallic cobalt and copper films with either CVD or ALD. While these precursors can be also used to deposit oxide thin films, the design and synthesis of volatile and reactive molecules specifically optimized for oxide deposition would undoubtedly be beneficial.

With respect to applications, the deposition of ternary and quaternary cobalt- and copper-containing oxides using ALD should be explored further. As an example, an ALD deposition process for the prototypical p-type TCO, $CuAlO_2$, remains to be published even though robust ALD processes for both Cu_2O and Al_2O_3 exist. In view of obtaining thin films with optimized electronic and optical properties, epitaxial deposition of these materials should also be considered.

8 References

(1) Sasaki, S.; Fujino, K.; Takeuchi, Y. X-Ray Determination of Electron Density Distributions in Oxides, MgO, MnO, CoO, and NiO, and Atomic Scattering Factors of Their Constituent Atoms. *Proc. Japan Acad. Ser. B* **1979**, *55* (2), 43–48.

(2) Redman, M. J.; Steward, E. G. Cobaltous Oxide with the Zinc Blende/Wurtzite-Type Crystal Structure. *Nature* **1962**, *193* (4818), 867.

(3) Meyer, W.; Hock, D.; Biedermann, K.; Gubo, M.; Müller, S.; Hammer, L.; Heinz, K. Coexistence of Rocksalt and Wurtzite Structure in Nanosized CoO Films. *Phys. Rev. Lett.* **2008**, *101* (1), 16103.

(4) Biedermann, K.; Gubo, M.; Hammer, L.; Heinz, K. Phases and Phase Transitions of Hexagonal Cobalt Oxide Films on Ir(100)-(1×1). *J. Phys. Condens. Matter* **2009**, *21* (18), 185003.

(5) Väyrynen, K.; Hatanpää, T.; Mattinen, M.; Heikkilä, M.; Mizohata, K.; Meinander, K.; Räisänen, J.; Ritala, M.; Leskelä, M. Diamine Adduct of Cobalt(II) Chloride as a Precursor for Atomic Layer Deposition of Stoichiometric Cobalt(II) Oxide and Reduction Thereof to Cobalt Metal Thin Films. *Chem. Mater.* **2018**, *30* (10), 3499–3507.

(6) Picard, J. P.; Baud, G.; Besse, J. P.; Chevalier, R. Croissance Cristalline et Étude Structurale de Co_3O_4. *J. Less Common Met.* **1980**, *75* (1), 99–104.

(7) Rao, K. V; Smakula, A. Dielectric Properties of Cobalt Oxide, Nickel Oxide, and Their Mixed Crystals. *J. Appl. Phys.* **1965**, *36* (6), 2031–2038.

(8) Joshi, G. M.; Pai, M.; Harrison, H. R.; Sandberg, C. J.; Aragón, R.; Honig, J. M. Electrical Properties of Undoped Single CoO Crystals. *Mater. Res. Bull.* **1980**, *15* (11), 1575–1579.

(9) Shen, Z. X.; Allen, J. W.; Lindberg, P. A. P.; Dessau, D. S.; Wells, B. O.; Borg, A.; Ellis, W.; Kang, J. S.; Oh, S. J.; Lindau, I.; et al. Photoemission Study of CoO. *Phys. Rev. B* **1990**, *42* (3), 1817–1828.

(10) van Elp, J.; Wieland, J. L.; Eskes, H.; Kuiper, P.; Sawatzky, G. A.; de Groot, F. M. F.; Turner, T. S. Electronic Structure of CoO, Li-Doped CoO, and $LiCoO_2$. *Phys. Rev. B* **1991**, *44* (12), 6090–6103.

(11) Wdowik, U. D.; Parlinski, K. Lattice Dynamics of CoO from First Principles. *Phys. Rev. B* **2007**, *75* (10), 104306.

(12) Cheng, C.-S.; Serizawa, M.; Sakata, H.; Hirayama, T. Electrical Conductivity of Co_3O_4 Films Prepared by Chemical Vapour Deposition. *Mater. Chem. Phys.* **1998**, *53* (3), 225–230.

(13) Cho, S. B.; Sim, E. S.; Chung, Y.-C. Elucidating the Unintentional p-type Nature of Spinel Co_3O_4: A Defect Study Using ab initio Calculation. *J. Eur. Ceram. Soc.* **2018**, *38* (2), 629–635.

(14) Holden, K. E. K.; Conley, J. F. Characterization of Atomic Layer Deposited Semiconducting Co_3O_4. *J. Vac. Sci. Technol. A* **2019**, *37* (2), 20903.

(15) Qiao, L.; Xiao, H. Y.; Meyer, H. M.; Sun, J. N.; Rouleau, C. M.; Puretzky, A. A.; Geohegan, D. B.; Ivanov, I. N.; Yoon, M.; Weber, W. J.; et al. Nature of the Band Gap and Origin of the Electro-/Photoactivity of Co_3O_4. *J. Mater. Chem. C* **2013**, *1* (31), 4628–4633.

(16) Wang, S.; Zhang, B.; Zhao, C.; Li, S.; Zhang, M.; Yan, L. Valence Control of Cobalt Oxide Thin Films by Annealing Atmosphere. *Appl. Surf. Sci.* **2011**, *257* (8), 3358–3362.

(17) Yang, J.; Liu, H.; Martens, W. N.; Frost, R. L. Synthesis and Characterization of Cobalt Hydroxide, Cobalt Oxyhydroxide, and Cobalt Oxide Nanodiscs. *J. Phys. Chem. C* **2010**, *114* (1), 111–119.
(18) Petitto, S. C.; Marsh, E. M.; Carson, G. A.; Langell, M. A. Cobalt Oxide Surface Chemistry: The Interaction of CoO (100), Co_3O_4 (110) and Co_3O_4 (111) with Oxygen and Water. *J. Mol. Catal. A Chem.* **2008**, *281* (1), 49–58.
(19) Schwarz, M.; Faisal, F.; Mohr, S.; Hohner, C.; Werner, K.; Xu, T.; Skála, T.; Tsud, N.; Prince, K. C.; Matolín, V.; et al. Structure-Dependent Dissociation of Water on Cobalt Oxide. *J. Phys. Chem. Lett.* **2018**, *9* (11), 2763–2769.
(20) Gao, X.; Guo, H.; Xia, Y.; Yin, J.; Liu, Z. Unipolar Resistive Switching Characteristics in Co_3O_4 Films. *Thin Solid Films* **2010**, *519* (1), 450–452.
(21) Kalam, K.; Seemen, H.; Mikkor, M.; Jõgiaas, T.; Ritslaid, P.; Tamm, A.; Kukli, K.; Kasikov, A.; Link, J.; Stern, R.; et al. Electrical and Magnetic Properties of Atomic Layer Deposited Cobalt Oxide and Zirconium Oxide Nanolaminates. *Thin Solid Films* **2019**, *669*, 294–300.
(22) Xu, J. M.; Cheng, J. P. The Advances of Co_3O_4 as Gas Sensing Materials: A Review. *J. Alloys Compd.* **2016**, *686*, 753–768.
(23) Wang, B.; Bates, J. B.; Hart, F. X.; Sales, B. C.; Zuhr, R. A.; Robertson, J. D. Characterization of Thin-Film Rechargeable Lithium Batteries with Lithium Cobalt Oxide Cathodes. *J. Electrochem. Soc.* **1996**, *143* (10), 3203–3213.
(24) Li, W. Y.; Xu, L. N.; Chen, J. Co_3O_4 Nanomaterials in Lithium-Ion Batteries and Gas Sensors. *Adv. Funct. Mater.* **2005**, *15* (5), 851–857.
(25) Lokhande, C. D.; Dubal, D. P.; Joo, O.-S. Metal Oxide Thin Film Based Supercapacitors. *Curr. Appl. Phys.* **2011**, *11* (3), 255–270.
(26) Li, Y.; Huang, K.; Yao, Z.; Liu, S.; Qing, X. Co_3O_4 Thin Film Prepared by a Chemical Bath Deposition for Electrochemical Capacitors. *Electrochim. Acta* **2011**, *56* (5), 2140–2144.
(27) Harriman, A.; Pickering, I. J.; Thomas, J. M.; Christensen, P. A. Metal Oxides as Heterogeneous Catalysts for Oxygen Evolution under Photochemical Conditions. *J. Chem. Soc. Faraday Trans. 1 Phys. Chem. Condens. Phases* **1988**, *84* (8), 2795–2806.
(28) Mattioli, G.; Giannozzi, P.; Amore Bonapasta, A.; Guidoni, L. Reaction Pathways for Oxygen Evolution Promoted by Cobalt Catalyst. *J. Am. Chem. Soc.* **2013**, *135* (41), 15353–15363.
(29) Zhang, M.; de Respinis, M.; Frei, H. Time-Resolved Observations of Water Oxidation Intermediates on a Cobalt Oxide Nanoparticle Catalyst. *Nat. Chem.* **2014**, *6*, 362.
(30) Liardet, L.; Katz, J. E.; Luo, J.; Grätzel, M.; Hu, X. An Ultrathin Cobalt–Iron Oxide Catalyst for Water Oxidation on Nanostructured Hematite Photoanodes. *J. Mater. Chem. A* **2019**, *7* (11), 6012–6020.
(31) Wang, L.; Mitoraj, D.; Turner, S.; Khavryuchenko, O. V; Jacob, T.; Hocking, R. K.; Beranek, R. Ultrasmall $CoO(OH)_x$ Nanoparticles As a Highly Efficient "True" Cocatalyst in Porous Photoanodes for Water Splitting. *ACS Catal.* **2017**, *7* (7), 4759–4767.
(32) Mackenzie, A. P. The Properties of Ultrapure Delafossite Metals. *Reports Prog. Phys.* **2017**, *80* (3), 32501.
(33) Windisch, C. F.; Exarhos, G. J.; Ferris, K. F.; Engelhard, M. H.; Stewart, D. C. Infrared Transparent Spinel Films with p-type Conductivity. *Thin Solid Films* **2001**, *398–399*, 45–52.

(34) Silwal, P.; Miao, L.; Stern, I.; Zhou, X.; Hu, J.; Ho Kim, D. Metal Insulator Transition with Ferrimagnetic Order in Epitaxial Thin Films of Spinel $NiCo_2O_4$. *Appl. Phys. Lett.* **2012**, *100* (3), 32102.
(35) Hagen, D. J.; Tripathi, T. S.; Karppinen, M. Atomic Layer Deposition of Nickel-Cobalt Spinel Thin Films. *Dalt. Trans.* **2017**, *46* (14), 4796–4805.
(36) Takahashi, M.; Fine, M. E. Magnetic Behavior of Quenched and Aged $CoFe_2O_4$ – Co_3O_4 Alloys. *J. Appl. Phys.* **1972**, *43* (10), 4205–4216.
(37) Bazuev, G. V; Korolyov, A. V. Magnetic Behavior of $MnCo_2O_{4+\delta}$ Spinel Obtained by Thermal Decomposition of Binary Oxalates. *J. Magn. Magn. Mater.* **2008**, *320* (18), 2262–2268.
(38) Androulakis, J.; Katsarakis, N.; Giapintzakis, J. Ferromagnetic and Antiferromagnetic Interactions in Lanthanum Cobalt Oxide at Low Temperatures. *Phys. Rev. B* **2001**, *64* (17), 174401.
(39) Miyazaki, Y. Crystal Structure and Thermoelectric Properties of the Misfit-Layered Cobalt Oxides. *Solid State Ionics* **2004**, *172* (1), 463–467.
(40) Lybeck, J.; Valkeapää, M.; Shibasaki, S.; Terasaki, I.; Yamauchi, H.; Karppinen, M. Thermoelectric Properties of Oxygen-Tuned ALD-Grown $[Ca_2CoO_3]_{0.62}[CoO_2]$ Thin Films. *Chem. Mater.* **2010**, *22* (21), 5900–5904.
(41) Wang, L.-S.; Wu, H.; Desai, S. R.; Lou, L. Electronic Structure of Small Copper Oxide Clusters. *Phys. Rev. B* **1996**, *53* (12), 8028–8031.
(42) Morgan, P. E. D.; Partin, D. E.; Chamberland, B. L.; O'Keeffe, M. Synthesis of Paramelaconite: Cu_4O_3. *J. Solid State Chem.* **1996**, *121* (1), 33–37.
(43) Meyer, B. K.; Polity, A.; Reppin, D.; Becker, M.; Hering, P.; Klar, P. J.; Sander, T.; Reindl, C.; Benz, J.; Eickhoff, M.; et al. Binary Copper Oxide Semiconductors: From Materials towards Devices. *Phys. Status Solidi Basic Res.* **2012**, *249* (8), 1487–1509.
(44) Li, J.; Vizkelethy, G.; Revesz, P.; Mayer, J. W.; Tu, K. N. Oxidation and Reduction of Copper Oxide Thin Films. *J. Appl. Phys.* **1991**, *69* (2), 1020–1029.
(45) Ghijsen, J.; Tjeng, L.; van Elp, J.; Eskes, H.; Westerink, J.; Sawatzky, G.; Czyzyk, M. Electronic Structure of Cu_2O and CuO. *Phys. Rev. B* **1988**, *38* (16), 11322–11330.
(46) Raebiger, H.; Lany, S.; Zunger, A. Origins of the p-type Nature and Cation Deficiency in Cu_2O and Related Materials. *Phys. Rev. B* **2007**, *76* (4), 45209.
(47) Paul, G. K.; Nawa, Y.; Sato, H.; Sakurai, T.; Akimoto, K. Defects in Cu_2O Studied by Deep Level Transient Spectroscopy. *Appl. Phys. Lett.* **2006**, *88* (14), 141901.
(48) Ishizuka, S.; Maruyama, T.; Akimoto, K. Thin-Film Deposition of Cu2O by Reactive Radio-Frequency Magnetron Sputtering. *Jpn. J. Appl. Phys.* **2000**, *39* (8 A), L786–L788.
(49) Muñoz-Rojas, D.; Jordan, M.; Yeoh, C.; Marin, A. T.; Kursumovic, A.; Dunlop, L. A.; Iza, D. C.; Chen, A.; Wang, H.; MacManus Driscoll, J. L. Growth of ~5 $cm^2 V^{-1} s^{-1}$ Mobility, p-type Copper(I) Oxide (Cu_2O) Films by Fast Atmospheric Atomic Layer Deposition (AALD) at 225°C and Below. *AIP Adv.* **2012**, *2* (4), 42179.
(50) Matsuzaki, K.; Nomura, K.; Yanagi, H.; Kamiya, T.; Hirano, M.; Hosono, H. Epitaxial Growth of High Mobility Cu_2O Thin Films and Application to p-Channel Thin Film Transistor. *Appl. Phys. Lett.* **2008**, *93* (20), 202107.
(51) Biccari, F. *Defects and Doping in Cu $_2$O, Ph.D. Thesis*; Sapienza University of Rome, Italy, 2009.
(52) Malerba, C.; Biccari, F.; Leonor Azanza Ricardo, C.; D'Incau, M.; Scardi, P.; Mittiga, A. Absorption Coefficient of Bulk and Thin Film Cu_2O. *Sol. Energy Mater. Sol. Cells* **2011**, *95* (10), 2848–2854.
(53) Alnes, M. E.; Monakhov, E.; Fjellvåg, H.; Nilsen, O. Atomic Layer Deposition of

Copper Oxide Using Copper(II) Acetylacetonate and Ozone. *Chem. Vap. Depos.* **2012**, *18* (4-6), 173–178.
(54) Tripathi, T. S.; Terasaki, I.; Karppinen, M. Anomalous Thickness-Dependent Optical Energy Gap of ALD-Grown Ultra-Thin CuO Films. *J. Phys. Condens. Matter* **2016**, *28* (47), 475801.
(55) Cho, S. Optical and Electrical Properties of CuO Thin Films Deposited at Several Growth Temperatures by Reactive RF Magnetron Sputtering. *Met. Mater. Int.* **2013**, *19* (6), 1327–1331.
(56) Reppin, D.; Polity, A.; Meyer, B. K.; Shokhovets, S. Optical and Electrical Properties of Cu_2O, Cu_4O_3 and CuO. *MRS Proc.* **2012**, *1494*, 165–169.
(57) Ghijsen, J.; Tjeng, L. H.; van Elp, J.; Eskes, H.; Westerink, J.; Sawatzky, G. A.; Czyzyk, M. T. Electronic Structure of Cu_2O and CuO. *Phys. Rev. B* **1988**, *38* (16), 11322–11330.
(58) Korzhavyi, P. A.; Soroka, I. L.; Isaev, E. I.; Lilja, C.; Johansson, B. Exploring Monovalent Copper Compounds with Oxygen and Hydrogen. *Proc. Natl. Acad. Sci.* **2012**, *109* (3), 686 LP – 689.
(59) Fukuda, M.; Koga, N. Kinetics and Mechanisms of the Thermal Decomposition of Copper(II) Hydroxide: A Consecutive Process Comprising Induction Period, Surface Reaction, and Phase Boundary-Controlled Reaction. *J. Phys. Chem. C* **2018**, *122* (24), 12869–12879.
(60) Rai, B. P. Cu_2O Solar Cells: A Review. *Sol. Cells* **1988**, *25* (3), 265–272.
(61) Akimoto, K.; Ishizuka, S.; Yanagita, M.; Nawa, Y.; Paul, G. K.; Sakurai, T. Thin Film Deposition of Cu_2O and Application for Solar Cells. *Sol. Energy* **2006**, *80* (6), 715–722.
(62) Bagal, I. V; Chodankar, N. R.; Hassan, M. A.; Waseem, A.; Johar, M. A.; Kim, D.-H.; Ryu, S.-W. Cu_2O as an Emerging Photocathode for Solar Water Splitting - A Status Review. *Int. J. Hydrogen Energy* **2019**, *44* (39), 21351–21378.
(63) Toe, C. Y.; Zheng, Z.; Wu, H.; Scott, J.; Amal, R.; Ng, Y. H. Photocorrosion of Cuprous Oxide in Hydrogen Production: Rationalising Self-Oxidation or Self-Reduction. *Angew. Chemie* **2018**, *130* (41), 13801–13805.
(64) Paracchino, A.; Laporte, V.; Sivula, K.; Grätzel, M.; Thimsen, E. Highly Active Oxide Photocathode for Photoelectrochemical Water Reduction. *Nat Mater* **2011**, *10* (6), 456–461.
(65) Paracchino, A.; Brauer, J. C.; Moser, J.-E.; Thimsen, E.; Graetzel, M. Synthesis and Characterization of High-Photoactivity Electrodeposited Cu_2O Solar Absorber by Photoelectrochemistry and Ultrafast Spectroscopy. *J. Phys. Chem. C* **2012**, *116* (13), 7341–7350.
(66) Fortunato, E.; Figueiredo, V.; Barquinha, P.; Elamurugu, E.; Barros, R.; Gonçalves, G.; Park, S.-H. K.; Hwang, C.-S.; Martins, R. Thin-Film Transistors Based on p-Type Cu_2O Thin Films Produced at Room Temperature. *Appl. Phys. Lett.* **2010**, *96* (19), 192102.
(67) Al-Jawhari, H. A. A Review of Recent Advances in Transparent p-type Cu_2O-Based Thin Film Transistors. *Mater. Sci. Semicond. Process.* **2015**, *40*, 241–252.
(68) Maeng, W.; Lee, S.-H.; Kwon, J.-D.; Park, J.; Park, J.-S. Atomic Layer Deposited p-Type Copper Oxide Thin Films and the Associated Thin Film Transistor Properties. *Ceram. Int.* **2016**, *42* (4), 5517–5522.
(69) Yao, Z. Q.; Liu, S. L.; Zhang, L.; He, B.; Kumar, A.; Jiang, X.; Zhang, W. J.; Shao, G. Room Temperature Fabrication of p-channel Cu_2O Thin-Film Transistors on Flexible Polyethylene Terephthalate Substrates. *Appl. Phys. Lett.* **2012**, *101* (4),

42114.
(70) Kawazoe, H.; Yasukawa, M.; Hyodo, H.; Kurita, M.; Yanagi, H.; Hosono, H. p-type Electrical Conduction in Transparent Thin Films of $CuAlO_2$. *Nature* **1997**, *389*, 939.
(71) Kudo, A.; Yanagi, H.; Hosono, H.; Kawazoe, H. $SrCu_2O_2$: A p-type Conductive Oxide with Wide Band Gap. *Appl. Phys. Lett.* **1998**, *73* (2), 220–222.
(72) Tripathi, T. S.; Niemela, J.-P.; Karppinen, M. Atomic Layer Deposition of Transparent Semiconducting Oxide $CuCrO_2$ Thin Films. *J. Mater. Chem. C* **2015**, *3* (32), 8364–8371.
(73) Tripathi, T. S.; Karppinen, M. Enhanced p-type Transparent Semiconducting Characteristics for ALD-Grown Mg-Substituted $CuCrO_2$ Thin Films. *Adv. Electron. Mater.* **2017**, *3* (6), 1600341.
(74) Ginley, D.; Coutts, T.; Perkins, J.; Young, D.; Li, X.; Parilla, P. Next-Generation Transparent Conducting Oxides for Photovoltaic Cells: An Overview. *MRS Proc.* **2001**, *668*, H2.7.
(75) Zhang, K. H. L.; Xi, K.; Blamire, M. G.; Egdell, R. G. p-type Transparent Conducting Oxides. *J. Phys. Condens. Matter* **2016**, *28* (38), 383002.
(76) Morales-Masis, M.; De Wolf, S.; Woods-Robinson, R.; Ager, J. W.; Ballif, C. Transparent Electrodes for Efficient Optoelectronics. *Adv. Electron. Mater.* **2017**, *3* (5), 1600529.
(77) Sønsteby, H. H.; Aarholt, T.; Prytz, Ø.; Fjellvåg, H.; Nilsen, O. First Complex Oxide Superconductor by Atomic Layer Deposition. *Chem. Commun.* **2018**, *54* (59), 8253–8256.
(78) Inam, A.; Hegde, M. S.; Wu, X. D.; Venkatesan, T.; England, P.; Miceli, P. F.; Chase, E. W.; Chang, C. C.; Tarascon, J. M.; Wachtman, J. B. As-deposited High T_c and J_c Superconducting Thin Films Made at Low Temperatures. *Appl. Phys. Lett.* **1988**, *53* (10), 908–910.
(79) Lee, S.-I.; Lee, S.; Mun, M.-O.; Bae, M.-K. Synthesis and Superconductivity of the $HgBa_2Ca_2Cu_3O_x$ Superconductors. *Phys. C Supercond.* **1994**, *235–240*, 895–896.
(80) Maeda, H.; Yanagisawa, Y. Recent Developments in High-Temperature Superconducting Magnet Technology (Review). *IEEE Trans. Appl. Supercond.* **2014**, *24* (3), 1–12.
(81) George, S. M. Atomic Layer Deposition: An Overview. *Chem. Rev.* **2010**, *110* (1), 111–131.
(82) Miikkulainen, V.; Leskelä, M.; Ritala, M.; Puurunen, R. L. Crystallinity of Inorganic Films Grown by Atomic Layer Deposition: Overview and General Trends. *J. Appl. Phys.* **2013**, *113* (2).
(83) Leskelä, M.; Ritala, M. Atomic Layer Deposition (ALD): From Precursors to Thin Film Structures. *Thin Solid Films* **2002**, *409* (1), 138–146.
(84) Ritala, M.; Niinisto, J. Industrial Applications of Atomic Layer Deposition. *ECS Trans.* **2009**, *25* (8, EuroCVD 17/CVD 17), 641–652.
(85) Lee, H.-B.-R. The Era of Atomic Crafting. *Chem. Mater.* **2019**, *31* (5), 1471–1472.
(86) Li, W.-M. Recent Developments of Atomic Layer Deposition Processes for Metallization. *Chem. Vap. Depos.* **2013**, *19* (4-6), 82–103.
(87) Niinistö, J.; Kukli, K.; Heikkilä, M.; Ritala, M.; Leskelä, M. Atomic Layer Deposition of High-k Oxides of the Group 4 Metals for Memory Applications. *Adv. Eng. Mater.* **2009**, *11* (4), 223–234.
(88) Mackus, A. J. M.; Bol, A. A.; Kessels, W. M. M. The Use of Atomic Layer Deposition in Advanced Nanopatterning. *Nanoscale* **2014**, *6* (19), 10941–10960.
(89) van Delft, J. A.; Garcia-Alonso, D.; Kessels, W. M. M. Atomic Layer Deposition for

Photovoltaics: Applications and Prospects for Solar Cell Manufacturing. *Semicond. Sci. Technol.* **2012**, *27* (7), 74002.
(90) Mayer, T. M.; Elam, J. W.; George, S. M.; Kotula, P. G.; Goeke, R. S. Atomic-Layer Deposition of Wear-Resistant Coatings for Microelectromechanical Devices. *Appl. Phys. Lett.* **2003**, *82* (17), 2883–2885.
(91) Kim, H. G.; Lee, H.-B.-R. Atomic Layer Deposition on 2D Materials. *Chem. Mater.* **2017**, *29* (9), 3809–3826.
(92) Hao, W.; Marichy, C.; Journet, C. Atomic Layer Deposition of Stable 2D Materials. *2D Mater.* **2018**, *6* (1), 12001.
(93) Knoops, H. C. M.; Donders, M. E.; van de Sanden, M. C. M.; Notten, P. H. L.; Kessels, W. M. M. Atomic Layer Deposition for Nanostructured Li-Ion Batteries. *J. Vac. Sci. Technol. A* **2011**, *30* (1), 10801.
(94) Meng, X.; Yang, X.-Q.; Sun, X. Emerging Applications of Atomic Layer Deposition for Lithium-Ion Battery Studies. *Adv. Mater.* **2012**, *24* (27), 3589–3615.
(95) O'Neill, B. J.; Jackson, D. H. K.; Lee, J.; Canlas, C.; Stair, P. C.; Marshall, C. L.; Elam, J. W.; Kuech, T. F.; Dumesic, J. A.; Huber, G. W. Catalyst Design with Atomic Layer Deposition. *ACS Catal.* **2015**, *5* (3), 1804–1825.
(96) Skoog, S. A.; Elam, J. W.; Narayan, R. J. Atomic Layer Deposition: Medical and Biological Applications. *Int. Mater. Rev.* **2013**, *58* (2), 113–129.
(97) Hatanpää, T. *Precursor Chemistry for Atomic Layer Deposition, Ph.D. Thesis*; University of Helsinki, Finland, 2019.
(98) Knapas, K.; Ritala, M. In Situ Studies on Reaction Mechanisms in Atomic Layer Deposition. *Crit. Rev. Solid State Mater. Sci.* **2013**, *38* (3), 167–202.
(99) Hämäläinen, J.; Ritala, M.; Leskelä, M. Atomic Layer Deposition of Noble Metals and Their Oxides. *Chem. Mater.* **2014**, *26* (1), 786–801.
(100) Kalutarage, L. C.; Clendenning, S. B.; Winter, C. H. Low-Temperature Atomic Layer Deposition of Copper Films Using Borane Dimethylamine as the Reducing Co-Reagent. *Chem. Mater.* **2014**, *26* (12), 3731–3738.
(101) Potts, S. E.; Kessels, W. M. M. Energy-Enhanced Atomic Layer Deposition for More Process and Precursor Versatility. *Coord. Chem. Rev.* **2013**, *257* (23), 3254–3270.
(102) Knoops, H. C. M.; Faraz, T.; Arts, K.; Kessels, W. M. M. (Erwin). Status and Prospects of Plasma-Assisted Atomic Layer Deposition. *J. Vac. Sci. Technol. A* **2019**, *37* (3), 30902.
(103) Miikkulainen, V.; Väyrynen, K.; Kilpi, V.; Han, Z.; Vehkamäki, M.; Mizohata, K.; Räisänen, J.; Ritala, M. Photo-Assisted ALD: Process Development and Application Perspectives. *Meet. Abstr.* **2017**, *MA2017-02* (25), 1093.
(104) Sprenger, J. K.; Sun, H.; Cavanagh, A. S.; George, S. M. Electron-Enhanced Atomic Layer Deposition of Silicon Thin Films at Room Temperature. *J. Vac. Sci. Technol. A* **2017**, *36* (1), 01A118.
(105) Rahtu, A. *Atomic Layer Deposition of High Permittivity Oxides : Film Growth and In Situ Studies, Ph.D. Thesis*; University of Helsinki, Finland, 2002.
(106) Knoops, H. C. M.; Elam, J. W.; Libera, J. A.; Kessels, W. M. M. Surface Loss in Ozone-Based Atomic Layer Deposition Processes. *Chem. Mater.* **2011**, *23* (9), 2381–2387.
(107) Uwai, K. Sequential Self-Limiting Growth of CuO on MgO(100) by Chemical Vapor Deposition. *J. Cryst. Growth* **1991**, *112* (1), 298–301.
(108) Waechtler, T.; Oswald, S.; Roth, N.; Jakob, A.; Lang, H.; Ecke, R.; Schulz, S. E.; Gessner, T.; Moskvinova, A.; Schulze, S.; et al. Copper Oxide Films Grown by Atomic Layer Deposition from Bis(Tri-n-Butylphosphane)Copper(I)Acetylacetonate

on Ta, TaN, Ru, and SiO_2. *J. Electrochem. Soc.* **2009**, *156* (6), H453–H459.
(109) Spiegelman, J.; Alvarez, D.; Holmes, R. J.; Heinlein, E.; Shamsi, Z. Advantages of Hydrogen Peroxide as an Oxidant for Atomic Layer Deposition and Related Novel Delivery System. *MRS Proc.* **2013**, *1494*, 209–214.
(110) Goldstein, D. N.; McCormick, J. A.; George, S. M. Al_2O_3 Atomic Layer Deposition with Trimethylaluminum and Ozone Studied by in Situ Transmission FTIR Spectroscopy and Quadrupole Mass Spectrometry. *J. Phys. Chem. C* **2008**, *112* (49), 19530–19539.
(111) Tomczak, Y.; Knapas, K.; Sundberg, M.; Leskelä, M.; Ritala, M. In Situ Reaction Mechanism Studies on the New t-BuN=M$(NEt_2)_3$ - Water and t-BuN=M$(NEt_2)_3$ - Ozone (M = Nb,Ta) Atomic Layer Deposition Processes. *Chem. Mater.* **2012**, *24* (9), 1555–1561.
(112) McCafferty, E.; Wightman, J. P. Determination of the Concentration of Surface Hydroxyl Groups on Metal Oxide Films by a Quantitative XPS Method. *Surf. Interface Anal.* **1998**, *26* (8), 549–564.
(113) Guerra-Nuñez, C.; Döbeli, M.; Michler, J.; Utke, I. Reaction and Growth Mechanisms in Al_2O_3 Deposited via Atomic Layer Deposition: Elucidating the Hydrogen Source. *Chem. Mater.* **2017**, *29* (20), 8690–8703.
(114) Aarik, L.; Arroval, T.; Rammula, R.; Mändar, H.; Sammelselg, V.; Aarik, J. Atomic Layer Deposition of TiO_2 from $TiCl_4$ and O_3. *Thin Solid Films* **2013**, *542*, 100–107.
(115) Kukli, K.; Kemell, M.; Mizohata, K.; Vehkamäki, M.; Kalam, K.; Castán, H.; Dueñas, S.; Link, J.; Stern, R.; Ritala, M.; et al. Atomic Layer Deposition of Zirconium Dioxide from Zirconium Tetraiodide and Ozone. *ECS J. Solid State Sci. Technol.* **2018**, *7* (2), P1–P8.
(116) Fink, C. K.; Nakamura, K.; Ichimura, S.; Jenkins, S. J. Silicon Oxidation by Ozone. *J. Phys. Condens. Matter* **2009**, *21* (18), 183001.
(117) Dhandapani, B.; Oyama, S. T. Gas Phase Ozone Decomposition Catalysts. *Appl. Catal. B Environ.* **1997**, *11* (2), 129–166.
(118) Li, W.; Gibbs, G. V.; Oyama, S. T. Mechanism of Ozone Decomposition on a Manganese Oxide Catalyst. 1. In Situ Raman Spectroscopy and Ab Initio Molecular Orbital Calculations. *J. Am. Chem. Soc.* **1998**, *120* (35), 9041–9046.
(119) Li, W.; Oyama, S. T. Mechanism of Ozone Decomposition on a Manganese Oxide Catalyst. 2. Steady-State and Transient Kinetic Studies. *J. Am. Chem. Soc.* **1998**, *120* (35), 9047–9052.
(120) Lim, B. S.; Rahtu, A.; Gordon, R. G. Atomic Layer Deposition of Transition Metals. *Nat. Mater.* **2003**, *2* (11), 749–754.
(121) Ngo, T. Q.; Posadas, A.; Seo, H.; Hoang, S.; McDaniel, M. D.; Utess, D.; Triyoso, D. H.; Buddie Mullins, C.; Demkov, A. A.; Ekerdt, J. G. Atomic Layer Deposition of Photoactive CoO/$SrTiO_3$ and CoO/TiO_2 on Si(001) for Visible Light Driven Photoelectrochemical Water Oxidation. *J. Appl. Phys.* **2013**, *114* (8), 84901.
(122) Zhang, Z.; Nallan, H. C.; Coffey, B. M.; Ngo, T. Q.; Pramanik, T.; Banerjee, S. K.; Ekerdt, J. G. Atomic Layer Deposition of Cobalt Oxide on Oxide Substrates and Low Temperature Reduction to Form Ultrathin Cobalt Metal Films. *J. Vac. Sci. Technol. A* **2018**, *37* (1), 10903.
(123) Zhang, Z.; Dwyer, T.; Sirard, S. M.; Ekerdt, J. G. Area-Selective Atomic Layer Deposition of Cobalt Oxide to Generate Patterned Cobalt Films. *J. Vac. Sci. Technol. A* **2019**, *37* (2), 20905.
(124) Gandrud, K. B. *Thin Films of Multiferroic $BiCoO_3$ by ALD*, M.Sc. Thesis; University of Oslo, Norway, 2009.

(125) Jung, S.; Nandi, D. K.; Yeo, S.; Kim, H.; Jang, Y.; Bae, J.-S.; Hong, T. E.; Kim, S.-H. Phase-Controlled Growth of Cobalt Oxide Thin Films by Atomic Layer Deposition. *Surf. Coatings Technol.* **2018**, *337*, 404–410.
(126) Han, B.; Park, J.-M.; Choi, K. H.; Lim, W.-K.; Mayangsari, T. R.; Koh, W.; Lee, W.-J. Atomic Layer Deposition of Stoichiometric Co_3O_4 Films Using Bis(1,4-Di-Iso-Propyl-1,4-Diazabutadiene) Cobalt. *Thin Solid Films* **2015**, *589*, 718–722.
(127) Seim, H.; Nieminen, M.; Niinistö, L.; Fjellvåg, H.; Johansson, L.-S. Growth of $LaCoO_3$ Thin Films from β-Diketonate Precursors. *Appl. Surf. Sci.* **1997**, *112* (0), 243–250.
(128) Klepper, K. B.; Nilsen, O.; Fjellvag, H. Growth of Thin Films of Co_3O_4 by Atomic Layer Deposition. *Thin Solid Films* **2007**, *515* (20–21), 7772–7781.
(129) Klepper, K. B.; Nilsen, O.; Fjellvåg, H. Epitaxial Growth of Cobalt Oxide by Atomic Layer Deposition. *J. Cryst. Growth* **2007**, *307* (2), 457–465.
(130) Diskus, M.; Nilsen, O.; Fjellvag, H. Thin Films of Cobalt Oxide Deposited on High Aspect Ratio Supports by Atomic Layer Deposition. *Chem. Vap. Depos.* **2011**, *17* (4–6), 135–140.
(131) Huang, B.; Cao, K.; Liu, X.; Qian, L.; Shan, B.; Chen, R. Tuning the Morphology and Composition of Ultrathin Cobalt Oxide Films via Atomic Layer Deposition. *RSC Adv.* **2015**, *5* (88), 71816–71823.
(132) Holden, K. E. K.; Jenkins, M. A.; Conley, J. F. Characterization of Atomic Layer Deposited Cobalt Oxide. *ECS Trans.* **2018**, *85* (13), 735–741.
(133) Han, B.; Choi, K. H.; Park, J. M.; Park, J. W.; Jung, J.; Lee, W.-J. Atomic Layer Deposition of Cobalt Oxide Thin Films Using Cyclopentadienylcobalt Dicarbonyl and Ozone at Low Temperatures. *J. Vac. Sci. Technol. a* **2013**, *31* (1), 01A145-01A145.
(134) Han, B.; Choi, K. H.; Park, K.; Han, W. S.; Lee, W.-J. Low-Temperature Atomic Layer Deposition of Cobalt Oxide Thin Films Using Dicobalt Hexacarbonyl Tert-Butylacetylene and Ozone. *Electrochem. Solid-State Lett.* **2011**, *15* (2), D14–D17.
(135) Nandi, D. K.; Manna, J.; Dhara, A.; Sharma, P.; Sarkar, S. K. Atomic Layer Deposited Cobalt Oxide: An Efficient Catalyst for $NaBH_4$ Hydrolysis. *J. Vac. Sci. Technol. A* **2015**, *34* (1), 01A115.
(136) Büyükyazi, M.; Fischer, T.; Yu, P.; Coll, M.; Mathur, S. A Cobalt(II)Heteroarylalkenolate Precursor for Homogeneous Co_3O_4 Coatings by Atomic Layer Deposition. *Dalt. Trans.* **2017**, *46* (38), 12996–13001.
(137) Rooth, M.; Lindahl, E.; Hårsta, A. Atomic Layer Deposition of Co_3O_4 Thin Films Using a CoI_2/O_2 Precursor Combination. *Chem. Vap. Depos.* **2006**, *12* (4), 209–213.
(138) Bard, A. J.; Fox, M. A. Artificial Photosynthesis: Solar Splitting of Water to Hydrogen and Oxygen. *Acc. Chem. Res.* **1995**, *28* (3), 141–145.
(139) Oh, S.; Jung, S.; Lee, Y. H.; Song, J. T.; Kim, T. H.; Nandi, D. K.; Kim, S.-H.; Oh, J. Hole-Selective $CoO_x/SiO_x/Si$ Heterojunctions for Photoelectrochemical Water Splitting. *ACS Catal.* **2018**, *8* (10), 9755–9764.
(140) Törndahl, T. *Atomic Layer Deposition of Copper, Copper(I) Oxide and Copper(I) Nitride on Oxide Substrates, Ph.D. Thesis*; University of Uppsala, Sweden, 2004.
(141) Törndahl, T.; Ottosson, M.; Carlsson, J.-O. Growth of Copper(I) Nitride by ALD Using Copper(II) Hexafluoroacetylacetonate, Water, and Ammonia as Precursors. *J. Electrochem. Soc.* **2006**, *153* (3), C146–C151.
(142) Kim, H.; Lee, M. Y.; Kim, S.-H.; Bae, S. I.; Ko, K. Y.; Kim, H.; Kwon, K.-W.; Hwang, J.-H.; Lee, D.-J. Highly-Conformal p-Type Copper(I) Oxide (Cu_2O) Thin Films by Atomic Layer Deposition Using a Fluorine-Free Amino-Alkoxide

Precursor. *Appl. Surf. Sci.* **2015**, *349*, 673–682.
(143) Avila, J. R.; Peters, A. W.; Li, Z.; Ortuño, M. A.; Martinson, A. B. F.; Cramer, C. J.; Hupp, J. T.; Farha, O. K. Atomic Layer Deposition of Cu(I) Oxide Films Using Cu(II) Bis(Dimethylamino-2-Propoxide) and Water. *Dalt. Trans.* **2017**, *46* (18), 5790–5795.
(144) George, M. A.; Hess, D. W.; Beck, S. E.; Ivankovits, J. C.; Bohling, D. A.; Lane, A. P. Reaction of 1,1,1,5,5,5-Hexafluoro-2,4-pentanedione (H+hfac) with CuO, Cu_2O, and Cu Films. *J. Electrochem. Soc.* **1995**, *142* (3), 961–965.
(145) Kim, H.; Kim, S.-H.; Ko, K. Y.; Kim, H.; Kim, J.; Oh, J.; Lee, H.-B.-R. High Efficiency n-Si/p-Cu_2O Core-Shell Nanowires Photodiode Prepared by Atomic Layer Deposition of Cu_2O on Well-Ordered Si Nanowires Array. *Electron. Mater. Lett.* **2016**, *12* (3), 404–410.
(146) Young, V. L.; Cox, D. F.; Davis, M. E. Metalorganic Chemical Vapor Deposition of Copper from Copper(II) Dimethylaminoethoxide. *Chem. Mater.* **1993**, *5* (12), 1701–1709.
(147) Becker, R.; Devi, A.; Weiß, J.; Weckenmann, U.; Winter, M.; Kiener, C.; Becker, H.-W.; Fischer, R. A. A Study on the Metal Organic CVD of Pure Copper Films from Low Cost Copper(II) Dialkylamino-2-Propoxides: Tuning the Thermal Properties of the Precursor by Small Variations of the Ligand. *Chem. Vap. Depos.* **2003**, *9* (3), 149–156.
(148) Gordon, P. G.; Kurek, A.; Barry, S. T. Trends in Copper Precursor Development for CVD and ALD Applications. *ECS J. Solid State Sci. Technol.* **2015**, *4* (1), N3188–N3197.
(149) Gao, Y.; Zandi, O.; Hamann, T. W. Atomic Layer Stack Deposition-Annealing Synthesis of $CuWO_4$. *J. Mater. Chem. A* **2016**, *4* (8), 2826–2830.
(150) Cheng, B.; Yi, H.; He, C.; Liu, C.; Lei, A. Revealing the Ligand Effect on Copper(I) Disproportionation via Operando IR Spectra. *Organometallics* **2015**, *34* (1), 206–211.
(151) Mackus, A. J. M.; Schneider, J. R.; MacIsaac, C.; Baker, J. G.; Bent, S. F. Synthesis of Doped, Ternary, and Quaternary Materials by Atomic Layer Deposition: A Review. *Chem. Mater.* **2019**, *31* (4), 1142–1183.
(152) Uusi-Esko, K.; Rautama, E.-L.; Laitinen, M.; Sajavaara, T.; Karppinen, M. Control of Oxygen Nonstoichiometry and Magnetic Property of $MnCo_2O_4$ Thin Films Grown by Atomic Layer Deposition. *Chem. Mater.* **2010**, *22* (23), 6297–6300.
(153) Scheffe, J. R.; Li, J.; Weimer, A. W. A Spinel Ferrite/Hercynite Water-Splitting Redox Cycle. *Int. J. Hydrogen Energy* **2010**, *35* (8), 3333–3340.
(154) Chong, Y. T.; Yau, E. M. Y.; Nielsch, K.; Bachmann, J. Direct Atomic Layer Deposition of Ternary Ferrites with Various Magnetic Properties. *Chem. Mater.* **2010**, *22* (24), 6506–6508.
(155) Lie, M.; Barnholt Klepper, K.; Nilsen, O.; Fjellvag, H.; Kjekshus, A. Growth of Iron Cobalt Oxides by Atomic Layer Deposition. *Dalt. Trans.* **2008**, No. 2, 253–259.
(156) Ahvenniemi, E.; Matvejeff, M.; Karppinen, M. $SrCoO_{3-\delta}$ Thin Films by Atomic Layer Deposition. *Appl. Surf. Sci.* **2014**, *320*, 838–842.
(157) Ahvenniemi, E.; Matvejeff, M.; Karppinen, M. Atomic Layer Deposition of Quaternary Oxide (La,Sr)$CoO_{3-\delta}$ Thin Films. *Dalt. Trans.* **2015**, *44* (17), 8001–8006.
(158) Łukasiewicz, M.; Wójcik-Głodowska, A.; Guziewicz, E.; Jakieła, R.; Krajewski, T.; Łusakowska, E.; Paszkowicz, W.; Minikayev, R.; Kiecana, M.; Sawicki, M.; et al. ZnCoO Films Obtained at Low Temperature by Atomic Layer Deposition Using Organic Zinc and Cobalt Precursors. *Acta Phys. Pol. A* **2016**, *114* (5), 1235–1240.

(159) Pore, V.; Dimri, M.; Khanduri, H.; Stern, R.; Lu, J.; Hultman, L.; Kukli, K.; Ritala, M.; Leskelä, M. Atomic Layer Deposition of Ferromagnetic Cobalt Doped Titanium Oxide Thin Films. *Thin Solid Films* **2011**, *519* (10), 3318–3324.
(160) Seemen, H.; Rähn, M.; Kalam, K.; Sajavaara, T.; Dueñas, S.; Castán, H.; Link, J.; Stern, R.; Kukli, K.; Tamm, A. Properties of Atomic Layer Deposited Nanolaminates of Zirconium and Cobalt Oxides. *ECS J. Solid State Sci. Technol.* **2018**, *7* (8), P402–P409.
(161) Tripathi, T. S.; Yadav, C. S.; Karppinen, M. Transparent Ferrimagnetic Semiconducting $CuCr_2O_4$ Thin Films by Atomic Layer Deposition. *APL Mater.* **2016**, *4* (4), 46106.
(162) Sønsteby, H. H.; Bratvold, J. E.; Weibye, K.; Fjellvåg, H.; Nilsen, O. Phase Control in Thin Films of Layered Cuprates. *Chem. Mater.* **2018**, *30* (3), 1095–1101.
(163) Xu, S.-S.; Lu, H.-L.; Zhang, Y.; Wang, T.; Geng, Y.; Huang, W.; Ding, S.-J.; Zhang, D. W. Bandgap Narrowing and Conductivity Evolution of Atomic-Layer-Deposited ZnO:Cu Thin Films under Rapid Thermal Annealing. *J. Alloys Compd.* **2015**, *638*, 133–135.
(164) Suntola, T. Atomic Layer Epitaxy. *Thin Solid Films* **1992**, *216* (1), 84–89.
(165) Ylilammi, M.; Ranta-aho, T. Optical Determination of the Film Thicknesses in Multilayer Thin Film Structures. *Thin Solid Films* **1993**, *232* (1), 56–62.
(166) Waldo, R. A.; Militello, M. C.; Gaarenstroom, S. W. Quantitative Thin-Film Analysis with an Energy-Dispersive X-Ray Detector. *Surf. Interface Anal.* **1993**, *20* (2), 111–114.
(167) Biesinger, M. C.; Lau, L. W. M.; Gerson, A. R.; Smart, R. S. C. Resolving Surface Chemical States in XPS Analysis of First Row Transition Metals, Oxides and Hydroxides: Sc, Ti, V, Cu and Zn. *Appl. Surf. Sci.* **2010**, *257* (3), 887–898.
(168) Biesinger, M. C.; Payne, B. P.; Grosvenor, A. P.; Lau, L. W. M.; Gerson, A. R.; Smart, R. S. C. Resolving Surface Chemical States in XPS Analysis of First Row Transition Metals, Oxides and Hydroxides: Cr, Mn, Fe, Co and Ni. *Appl. Surf. Sci.* **2011**, *257* (7), 2717–2730.
(169) Biesinger, M. C. Advanced Analysis of Copper X-Ray Photoelectron Spectra. *Surf. Interface Anal.* **2017**, *49* (13), 1325–1334.
(170) Jokinen, J.; Keinonen, J.; Tikkanen, P.; Kuronen, A.; Ahlgren, T.; Nordlund, K. Comparison of TOF-ERDA and Nuclear Resonance Reaction Techniques for Range Profile Measurements of KeV Energy Implants. *Nucl. Instruments Methods Phys. Res. Sect. B* **1996**, *119* (4), 533–542.
(171) Tauc, J. Optical Properties and Electronic Structure of Amorphous Ge and Si. *Mater. Res. Bull.* **1968**, *3* (1), 37–46.
(172) Bryan, A. M.; Long, G. J.; Grandjean, F.; Power, P. P. Synthesis, Spectroscopic Characterization, and Determination of the Solution Association Energy of the Dimer $[Co\{N(SiMe_3)_2\}_2]_2$. *Inorg. Chem.* **2013**, *52* (20), 12152–12160.
(173) Weinhold, F.; West, R. The Nature of the Silicon–Oxygen Bond. *Organometallics* **2011**, *30* (21), 5815–5824.
(174) Haukka, S.; Root, A. The Reaction of Hexamethyldisilazane and Subsequent Oxidation of Trimethylsilyl Groups on Silica Studied by Solid-State NMR and FTIR. *J. Phys. Chem.* **1994**, *98* (6), 1695–1703.
(175) Knisley, T. J.; Saly, M. J.; Heeg, M. J.; Roberts, J. L.; Winter, C. H. Volatility and High Thermal Stability in Mid- to Late-First-Row Transition-Metal Diazadienyl Complexes. *Organometallics* **2011**, *30* (18), 5010–5017.
(176) Klesko, J. P.; Kerrigan, M. M.; Winter, C. H. Low Temperature Thermal Atomic

Layer Deposition of Cobalt Metal Films. *Chem. Mater.* **2016**.
(177) Kerrigan, M. M.; Klesko, J. P.; Rupich, S. M.; Dezelah, C. L.; Kanjolia, R. K.; Chabal, Y. J.; Winter, C. H. Substrate Selectivity in the Low Temperature Atomic Layer Deposition of Cobalt Metal Films from Bis(1,4-Di-Tert-Butyl-1,3-Diazadienyl) Cobalt and Formic Acid. *J. Chem. Phys.* **2017**, *146* (5), 52813.
(178) Edwards, D. A.; Hayward, R. N. Transition Metal Acetates. *Can. J. Chem.* **1968**, *46* (22), 3443–3446.
(179) Didonato, G. C.; Busch, K. L. A Mass Spectrometric Study of Copper(II) Acetate. *Int. J. Mass Spectrom. Ion Process.* **1986**, *69* (1), 67–83.
(180) NIST Chemistry WebBook - Acetic Acid, https://webbook.nist.gov/cgi/cbook.cgi?ID=C64197.
(181) Potter, A. E.; Ritter, H. L. The Vapor Pressure of Acetic Acid and Acetic-d_3 Acid-d. The Liquid Density of Acetic-d_3 Acid-D. *J. Phys. Chem.* **1954**, *58* (11), 1040–1042.
(182) Lee, B. H.; Hwang, J. K.; Nam, J. W.; Lee, S. U.; Kim, J. T.; Koo, S.-M.; Baunemann, A.; Fischer, R. A.; Sung, M. M. Low-Temperature Atomic Layer Deposition of Copper Metal Thin Films: Self-Limiting Surface Reaction of Copper Dimethylamino-2-Propoxide with Diethylzinc. *Angew. Chemie Int. Ed.* **2009**, *48* (25), 4536–4539.
(183) Marabelli, F.; Parravicini, G. B.; Salghetti-Drioli, F. Optical Gap of CuO. *Phys. Rev. B* **1995**, *52* (3), 1433–1436.
(184) Oral, A. Y.; Menşur, E.; Aslan, M. H.; Başaran, E. The Preparation of Copper(II) Oxide Thin Films and the Study of Their Microstructures and Optical Properties. *Mater. Chem. Phys.* **2004**, *83* (1), 140–144.
(185) Sanal, K. C.; Vikas, L. S.; Jayaraj, M. K. Room Temperature Deposited Transparent p-channel CuO Thin Film Transistors. *Appl. Surf. Sci.* **2014**, *297*, 153–157.
(186) Patil, P. S.; Kadam, L. D.; Lokhande, C. D. Preparation and Characterization of Spray Pyrolysed Cobalt Oxide Thin Films. *Thin Solid Films* **1996**, *272* (1), 29–32.
(187) El Aakib, H.; Pierson, J. F.; Chaik, M.; Samba Vall, C.; Ait Dads, H.; Narjis, A.; Outzourhit, A. Evolution of the Structural, Morphological, Optical and Electrical Properties of Reactively RF-Sputtered Cobalt Oxide Thin Films with Oxygen Pressure. *Vacuum* **2019**, *159*, 346–352.
(188) Powell, R. J.; Spicer, W. E. Optical Properties of NiO and CoO. *Phys. Rev. B* **1970**, *2* (6), 2182–2193.
(189) Peter, L. M. Dynamic Aspects of Semiconductor Photoelectrochemistry. *Chem. Rev.* **1990**, *90* (5), 753–769.
(190) Bube, R. H. *Photoelectronic Properties of Semiconductors*, 1st ed.; Cambridge University Press, 1992.
(191) Tapiero, M.; Zielinger, J. P.; Noguet, C. Photomemory Effect in Cu_2O Single Crystals. Phenomenology and Interpretation. *Phys. status solidi* **1976**, *33* (1), 155–166.